Design and Synthesis of Meso- and Macrocyclic Tripodal Triamine Ligands and Investigations into their Coordination Chemistry

A thesis presented to the University of Dublin for the degree of Doctor of Philosophy

by Andrew Ure

Under the Supervision of Dr. Aidan R. McDonald

School of Chemistry
Trinity College
Febuary 2017

Author's Declaration

I declare that this thesis has not been submitted as an exercise for a degree at this or any other university and it is entirely my own work. I agree to deposit this thesis in the Universitys open access institutional repository or allow the library to do so on my behalf, subject to Irish Copyright Legislation and Trinity College Library conditions of use and acknowledgement.

Andrew Ure

17/02/2017

Contents

Abstract

The ability to directly and selectively functionalise hydrocarbons is one of the greatest remaining challenges facing chemists. The development of catalytic systems capable of affecting these transformations under ambient conditions would be of great environmental and economic importance. In nature, enzymes have been shown to utilise metal-based oxidants, such as high-valent terminal metal-oxos (M=O) to carry out these reactions. A multitude of biomimetic Mn=O and Fe=O complexes have been reported which are capable of activating C-H bonds. In this thesis, we postulate that late transition metal-oxos (Co, Ni, Cu, Zn) will form more potent oxidants than their early transition metal counterparts. However, there are currently no examples of stable late transition metal-oxo species in the literature, owing to the concept of the oxo-wall. It has been postulated that the oxo-wall may be circumvented through the synthesis of *pseudo*-tetrahedral metal-oxos. Herein, we describe the design and synthesis of several meso- and macrocyclic ligands. These oxidatively robust ligands have been designed to bind metals in a *pseudo*-tetrahedral fashion, which we believe will provide access to unprecedented late transition metal-oxos. We describe the synthesis of two mesocyclic ligands **2** and **4** as well as a library of useful synthons containing the 1,5-diazamacrocycle moiety. We show that **2** tends to form square pyramidal metal complexes [Fe(**2**)Cl_2)] (**24**), [Cu(**2**)$(MeCN)_2$] (**30**) and [Zn(**2**)Cl_2] (**31**) in the absensce of bridging ligands. In the case of $FeCl_2$, a diiron species [Fe_2(**2**)$_2Cl_2$)] (**25**) was also observed by X-ray crystallography. We also report the synthesis of a trigonal planar complex of **4**, [Cu(**4**)(MeCN)](PF_6) (**33**). Finally, we report the synthesis of a unique tricyclic macrocycle, **5**, and describe tentative evidence that supports the formation of Cu^I and lithium complexes of this ligand.

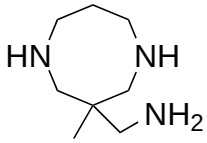

2

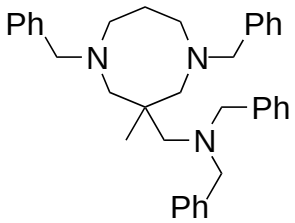

4

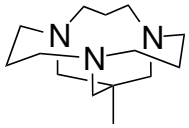

5

Acknowledgments

First and foremost I would like to thank Dr. Aidan McDonald for his continued support and guidance over the past four years. In particular, I would like to thank him for his patience and perseverance. There have been times when I suppose I haven't exactly been the model student but we got here in the end!

I'd also like to thank all of the members of the McDonald group, past and present. You have made the lab (or labs?!) an incredibly fun place to work. You've all put up with my constant whinging, some of you (Adrianna) more than others although I guess Paolo, Xin, Ciara, Bertrand, Peppe and Ankita have had their fair share too, it kept me sane over the past four years, so thanks! Even if the majority of you may disagree with that last statement! The memories made and lessons learned during this time will stay with me forever. The main one being that it's a terrible idea to move an entire lab across campus on one comically small trolley…Paolo deserves a shout out of his own. As well as becoming a good friend, and always being around to answer my questions no matter how ridiculous. Our discussions have helped me to push myself as a chemist. Its been a pleasure to work with someone so talented.

All of the Staff in the School of Chemistry have been incredibly supportive. I'd like to thank Dr John O'Brien and Dr Brendan Twamley for their infectious enthusiasm and always taking the time to teach and explain to me what they are doing and why, no matter how many annoying questions I ask! I'd also like to thank Dr Gary Hessman and Dr Martin Feeney for going out of their way to help with the mass-spec of my extra sensitive compounds. A lot of this work would not have been possible without your help. The staff in the Cocker lab, Peter and Peggy, have also been life savers at times. You have always been willing to help out with equipment and chemicals which was particularly useful

back in the day when we were poor…

I'd also like to thank the great friends that I've made within the department. Helen, Barry and Paddy (#mathsandcats) in particular have always been there to pick me up when things haven't been going so great and for that I'll always be thankful.

I'd like to thank my non-chemistry related friends. Mick, you have always been there for a pint whenever I've had a bad day in the lab and Amanda, you have been a source of constant encouragement, I honestly couldn't have done this without your support.

Finally, I'd like to thank my family. Mam and Dad, I'm still not convinced that you have a clue what I'm doing over here in Ireland but you've always supported me in doing what makes me happy, without question and for that I will always be grateful. And yes…I can get a real job now…

List of Figures

List of Schemes

List of Tables

List of Abbreviations

α-KG	α-ketoglutarate
***m*CPBA**	*meta*-chloroperbenzoic acid
^{iPr_3}TACN	1,4,7-triisopropyl-1,4,7-triazcyclononane
BDE	bond dissociation energy
bme-DACO	(2-mercaptoethyl)-1,5-diazacyclooactane
Bn-TPEN	*N*-benzyl-*N,N′,N′*-tris(2-pyridylmethyl)ethane-1,2-diamine)
MeCN	acetonitrile
$CHCl_3$	chloroform
CHD	cyclohexadiene
COSY	correlation spectroscopy
cyclam	1,4,8,11-tetraazacyclotetradecane
DACO	1,5-diazacyclooctane
DACODA	1,5-diazacyclooctane-*N,N*-diacetic acid
$DACOpy_2$	*N,N*-bis(2-pyridyl)-1,5-diazacycloactane
DCM	dichloromethane
DFT	density functional theory

DHA	9,10-dihydroanthracene
DMF	*N*,*N*-dimethylformamide
DTBP	2,6-di-*tert*butylphenol
EPR	electron paramagnetic resonance
ESI-MS	electrospray ionisation mass spectrometry
Et_2O	diethyl ether
EtOAc	ethyl acetate
EXAFS	extended x-ray absorption fine structure
FT-IR	fourier transform infrared
guanTAME	1,1,1-tris(2*N*- 1,1,3,3-tetramethylguanidino) methylethane
H_2bpc	4,5-di-chloro-1,2-bis(2-pyridine-2-carboxamido)benzene
H_4PHAB	1,2-*bis*(2,2-diphenyl-2-hydroxyethanamido)benzene
H_6buea	1,1′,1″-(nitrilotris(ethane-2,1-diyl))tris(3-(*tert*-butyl)urea)
HAA	hydrogen atom abstraction
HMBC	heteronuclear multiple-bond correlation
HSQC	heteronuclear single quantum coherence
KIE	kinetic isotope effect
L8	1-isopropyl-5-(2-(pyridin-2-yl)ethyl)-1,5-diazocane
Me_2opba	*o*-phenylenebis(*N*-methyloxamidate)

Me_3NTB	tris((1-methyl-1H-benzoimidazol-2-yl)methyl)amine
Me_3TAME	*N,N′,N″*-Trimethyl-1,1,1-tris(aminomethyl)ethane
Me_6TAME	1,1,1-tris(*N,N*-dimethylamino)methylethane
MMO	methane monooxygenase
N_4py	1,1-di(pyridin-2-yl)-*N,N*-bis(pyridin-2-ylmethyl)methanamine
NMR	nuclear magnetic resonance
NOE	nuclear Overhauser effect
OAT	oxygen atom transfer
OTf	1,1,1-trifluoromethane sulphonate
PCET	proton coupled electron transfer
PDP	(S,S)-1,1′-bis(pyridin-2-ylmethyl)-2,2′-bipyrrolidine
pMMO	particulate methane monooxygenase
$PyNMe_3$	3,6,9-trimethyl-3,6,9-triaza-1(2,6)-pyridinacyclodecaphane
pyTACN	1,4-dimethyl-7-(pyridin-2-ylmethyl)-1,4,7-triazonane
ROESY	rotating-frame Overhauser effect spectroscopy
salen	2,2-ethylene-*bis*-(nitrilomethylidene)diphenol
sMMO	soluble methane monooxygenase
TACDD	1,5,9-triazacyclododecane
TACN	1,4,7-triazacyclononane
TACUD	1,4,8-triazacycloundecane

TAME	1,1,1-tris(aminomethyl)ethane
TAML	tetra amido macrocyclic ligand
TEMPO-H	2,6-diisopropylpiperidin-1-ol
THF	tetrahydrofuran
TMC	1,4,8,11-tetramethyl-1,4,8,11-tetraazacyclotetradecane
TMG_2dien	2′,2′-((methylazanediyl)*bis*(ethane-2,1-diyl))*bis*(1,1,3,3-tetramethylguanidine)
TMG_3tren	2,2′-(((2-((*bis* (dimethylamino)methylene) amino)ethyl)azanediyl) *bis*(ethane-2,1-diyl))*bis* (1,1,3,3-tetramethylguanidine)
TPA	tris(pyridin-2-ylmethyl)amine
tren	tris(2-aminoethyl)amine
XANES	X-ray absorption near edge spectroscopy

Chapter 1

Introduction

1.1 Hydrocarbon Oxidation

The selective oxidation of aliphatic hydrocarbons remains one of the greatest challenges facing chemists.[1] Olefin and BXT (benzene, xylene, toluene) feedstocks are routinely converted to an array of more valuable products such as polymers owing to the relatively high reactivity of these substances. However, owing to their relative inertness, aliphatic hydrocarbons are generally valorised *via* cracking, dehydrogenation or reforming processes. These processes require large amounts of energy and produce significant amounts of carbon dioxide and therefore have a detrimental impact on the environment.[2]

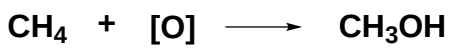

Figure 1.1: Direct oxidation of methane to methanol.

A prime example of the underutilisation of these aliphatic hydrocarbon feedstocks is methane.[2] As the main component of natural gas, methane is highly abundant and cheap; making it an ideal feedstock for C1 and C2 chemicals such as methanol or acetic acid. However, methane is currently either burned as a domestic fuel or industrially, converted into syngas . This can be attributed to the fact that the ability to directly and selectively oxidise methane (and other C2-C4 hydrocarbons) to olefins or oxygenates, as depicted in Figure 1.1, are transformations which still elude chemists.[2] This would be of great benefit not only because it would allow for the more efficient utilisation of methane but also because the facile conversion of gaseous methane to liquid methanol would allow for its convenient transport and storage; further encouraging its use. There are three main reasons for the absence of such a process.[3] The first is that the C-H bonds in these molecules are amongst the strongest known. Methane for example possesses a bond dissociation energy of 104 kcal mol^{-1}. Secondly, the C-H bonds in these molecules are apolar

owing to the similar electronegativity values of carbon and hydrogen, making them extremely difficult to activate. Finally, the C-H bonds in the oxidised products are often more reactive towards activation than the starting materials, meaning that over oxidation is a significant issue. Therefore if we wish to oxidise hydrocarbons under ambient conditions, we must endeavour to develop catalytic systems which are capable of doing so.[3]

1.2 Metalloenzymes

While the facile activation of strong C-H bonds remains a challenge synthetically, it is a feat which is routinely achieved by metalloenzymes. Transition metals within the active sites of these enzymes have been shown to be capable of activating O_2 and catalysing the oxidation of a plethora of substrates; displaying remarkable selectivity and substrate specificity. Therefore, it is useful to study these systems in order to understand the structure function relationships that purvey this highly desirable reactivity.

1.2.1 Cytochrome p450

Cytochrome p450s are a superfamily of haem based oxygenases that utilise O_2 to activate aliphatic C-H bonds.[4] The p450s represent one of the most well studied classes of oxygenases therefore provide an excellent example of the mechanisms employed by oxygenases in general to activate O_2 and subsequently C-H bonds.

In the resting state, the active site in p450 is comprised of a haem Fe^{III} centre, with a proximal thiolate and distal aqua ligand (**A**, Figure 1.2). Coordination of the substrate (RH) displaces the distal aqua ligand to give **B**, which is then reduced by one electron to give the Fe^{II} compound **C**. Compound **C** then reacts with O_2 to give the Fe^{III}-superoxo complex **D**. A second electron transfer step generates an Fe^{III}-peroxy anion which is subsequently protonated to give the Fe^{III}-hydroperoxo complex **E**, known as compound 0. Protonation of this unstable intermediate **E**, and concomitant heterolytic O-O bond scission gives the Fe^{IV}-oxo complex, **F**, known as compound I. Compound I then abstracts a hydrogen atom from the substrate to generate an Fe^{IV}-hydroxo complex **G**, known as compound II and a substrate radical. The Fe^{IV}-hydroxo then rebounds with the substrate radical to give the hydroxylated product and an Fe^{III} species.

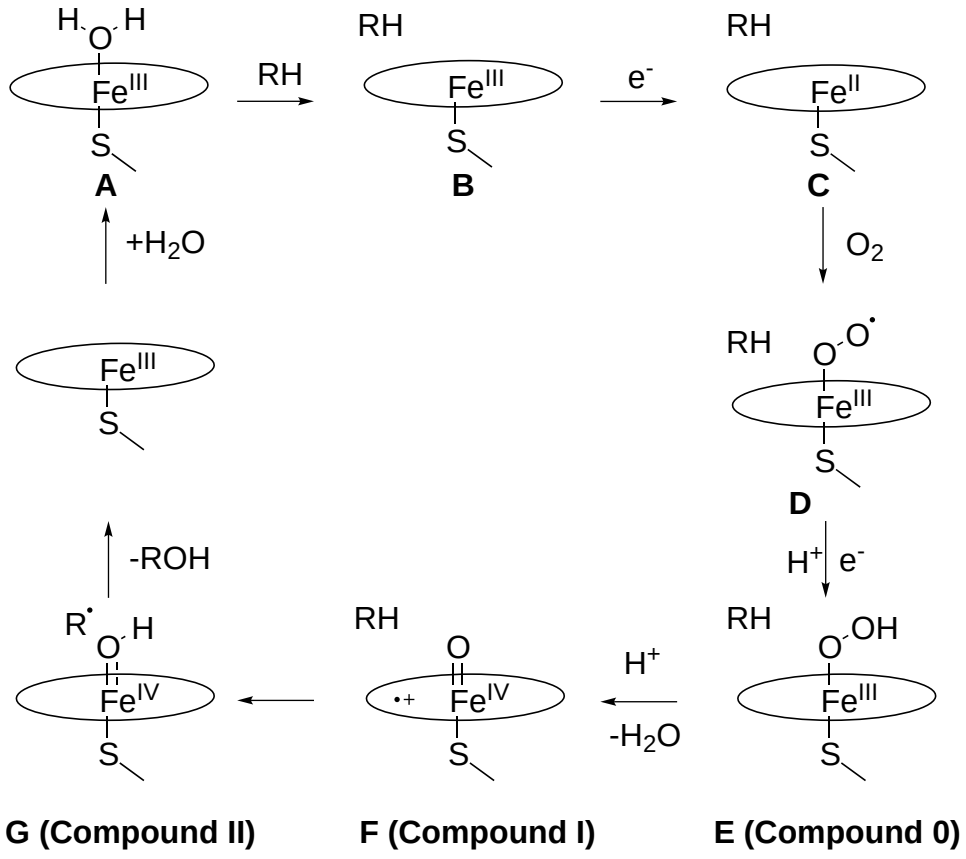

Figure 1.2: Postulated Catalytic Cycle of Cytochrome p450. The two electron reduction of O_2 followed by heterolytic O-O bond scission forms the active oxidant, Compound I. Circles represent the porphyrin framework.

This is known as the haem paradigm. This mechanism can be summarised as a two electron reduction of O_2 followed by heterolytic O-O bond scission to form a high-valent metal-oxo species; which is capable of activating strong C-H bonds.[4]

The extensive characterisation of compound I demonstrated the vital role that metal-oxos play in biological C-H activation and emphasised their importance as key synthetic targets for bioinorganic chemists.[5] More recently, Green and co-workers have fully characterised compound II and in doing so, elucidated the intriguing role of the thiolate ligand in p450s.[6] It is suggested that the strong electron donating ability of the thiolate pushes electron density onto the metal centre; lowering the one electron reduction potential. This results in a more

basic Fe^{IV}-oxo and a higher p*K*a in the Fe^{IV}-hydroxo *i.e.* a stronger O-H bond. This illustrates a fascinating strategy employed by these enzymes to activate C-H bonds, namely, the formation of a strong O-H bond in the process. The implications of this are discussed in greater detail below.

1.2.2 Non-Haem Enzymes

As well as the haem enzymes discussed above, high-valent metal oxos have also been observed as intermediates in a variety of non-haem enzymes. The α-ketoglutarate (α-KG) dependent oxygenases, are a family of non-haem iron oxygenases. These enzymes couple the oxidative decarboxylation of α-ketoglutarate with C-H activation. Bollinger and co-workers were the first to show that in the α-KG dependent enzyme taurine dioxygenase, a high spin (S = 2) Fe^{IV}-oxo (intermediate J) is responsible for hydrogen atom abstraction; in a manner akin to p450s compound I (Figure 1.2).[7] Since this discovery, an array of other Fe^{IV}-oxo intermediates have been reported as reactive intermediates in the catalytic cycle of α-KG dependent dioxygenases.[8–10] This adds further support

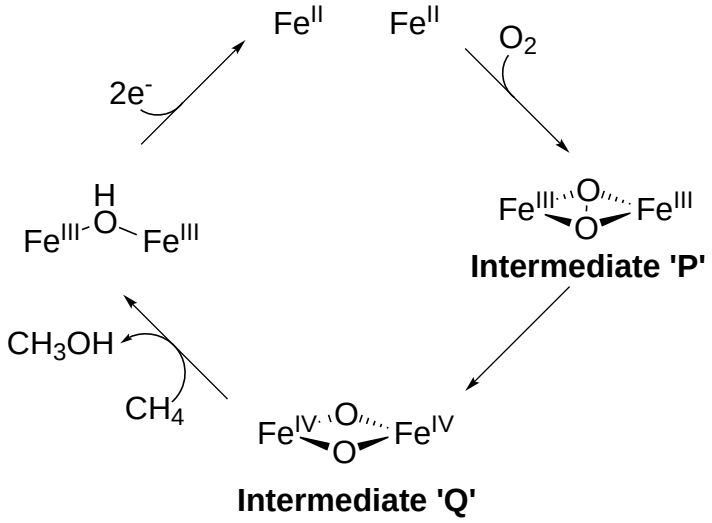

Figure 1.3: Catalytic Cycle of Soluble Methane Monooxygenase. The di-iron(IV)-oxo speices, Q, is responsible for C-H activation.

to the fact that metal-oxos are powerful oxidants.

In addition to the mononuclear non-haem iron enzymes capable of activating C-H bonds, there are also dinuclear iron enzymes that carry out similar transformations. Most notably, soluble methane monooxygenase (sMMO) is a di-iron enzyme capable of oxidising methane to methanol (Figure 1.3).[11,12] Similar to p450, dioxygen activation occurs through a two electron reduction of O_2. In the first step a di-iron(III)-peroxo, intermediate P, is formed from the reaction of the di-iron(II) resting state with O_2. Subsequent heterolytic O-O bond scission affords the di-iron(IV)-oxo species, intermediate Q; which is then responsible for functionalising the C-H bond in methane to produce methanol.[11,13]

Iron is extensively employed by enzymes as a cofactor due to its high natural abundance. However, in environments where other metals are rich they have been incorporated into the active sites of enzymes.[14] For example, particulate methane monooxygenase (pMMO) utilises a copper containing active site. Owing to the lack of a high resolution X-ray structure of pMMO, there has been significant debate over the exact nature of the active site.[14] Rosenzweig and co-workers have shown that it most likely contains a dicopper centre; as opposed to a mononuclear copper, mononuclear zinc or di-iron centre, as had been previously suggested.[11,15]

The exact structure of the reactive intermediate in pMMO is still unclear. Density functional theory (DFT) has been used to model potential active sites,

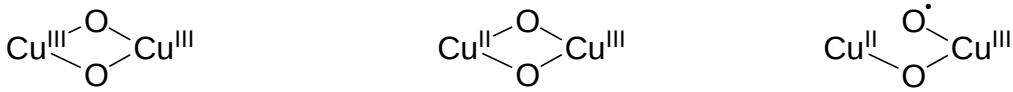

bis-μ-oxo-$Cu^{III}Cu^{III}$ **bis-μ-oxo-$Cu^{II}Cu^{III}$** **oxyl-Cu^{III}**

Figure 1.4: Proposed reactive intermediates for pMMO.

based on the moderate resolution X-ray structures reported in the literature.[11,14] Two reaction mechanisms namely, hydrogen atom abstraction (HAA) and concerted oxene insertion have been considered and the most energetically plausible di-copper intermediates arising from these calculations are shown in Figure 1.4.[14] These intermediates all contain either bridging or terminal metal-oxo moieties, providing a further example of the oxidising ability of these species. However, it is difficult to reasonably conclude more from these computational studies as there is insufficient data to compare all of the possible intermediates reacting by either of the mechanisms listed above.[14]

1.3 Bioinspired Hydrocarbon Oxidation Catalysis

The emergence of a myriad of studies on non-haem oxygenases over the past 20 years has shown how enzymes have evolved to make use of some of the most unreactive bonds known. Furthermore, they are able to do this in a selective manner.[16] This illustrates that although subtle, the chemical differences between (for example) secondary and tertiary C-H bonds are significant enough to allow preferential reactivity. These findings have directed significant attention to the area of bioinspired oxidation catalysis.[17] Bioinspired catalysts aim to utilise the extremely powerful yet selective metal based oxidants to oxidise C-H and C-C bonds. Similarly, metal-based oxidants have been employed in of water oxidation catalysts, inspired by the postulated reaction mechanism of photosystem II.[18] While this is beyond the scope of this thesis, Spiccia and Singh have recently published a comprehensive review on the subject.[19]

1.3.1 Iron Based Cataysts

Non-haem iron based catalytic systems are particularly well developed therefore, serve as an excellent illustrative example of the potential of bioinspired systems.[17] Non-haem systems have two main advantages over their

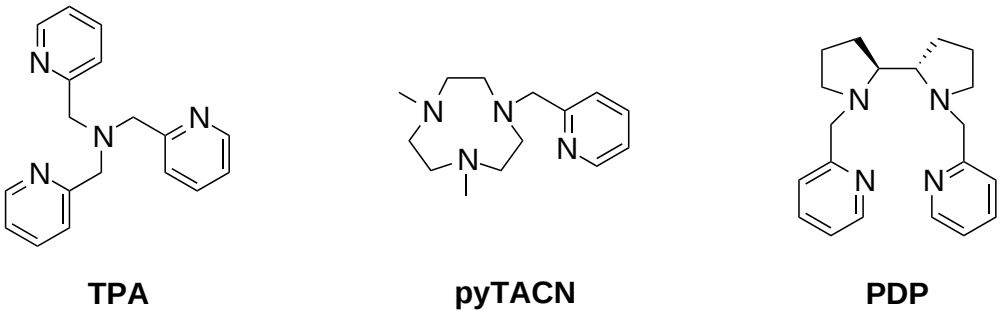

Figure 1.5: Ligands used in the synthesis of highly selective biomimetic iron catalysts.

haem counterparts. The first is that the supporting ligands in non-haem systems are less susceptible to oxidation than those in haem systems. The second advantage is that unlike haem systems, non-haem metal centres contain two vacant *cis*-coordination sites, potentially allowing for simultaneous binding of the substrate and oxidant in close proximity. This allows for intramolecular oxidations.

The first example of a non-haem iron catalyst was based on the tetradentate polypyridyl tris(pyridin-2-ylmethyl)amine (TPA) ligand shown in Figure 1.5 was reported by Que and co-workers.[20] The corresponding complex, $[Fe(TPA)(NCCH_3)_2](ClO_4)_2$ was reacted with 10 equivalents of H_2O_2 and 1000 equivalents of cyclohexane. Cyclohexanol (3.0 equivalents) was observed as the major product along with a small amount of cyclohexanone (0.7 equivalents). Furthermore, it was shown that the Fe(II) TPA complex could oxidise both *cis*- and *trans*- 1,2-dimethylcyclohexane to the corresponding tertiary alcohol products with 99% retention of stereochemistry. This provided the first evidence that a bioinspired catalyst was a viable candidate for C-H activation in the laboratory. Que and co-workers later demonstrated that an HO-Fe(V)=O was most likely the active oxidant.[21] However, this system showed a low yield (approximately 30% with respect to the oxidant in the case of cyclohexane) and low turnover numbers, this catalyst showed limited prospect for practical application.

These values were significantly improved on by Costas and co-workers who utilised the 1,4-dimethyl-7-(pyridin-2-ylmethyl)-1,4,7-triazonane (pyTACN) framework shown in Figure 1.5 and derivatives to generate highly active catalysts.[22,23] The Fe(II) comlex of pyTACN, $[Fe(pyTACN)(CF_3SO_3)_2]$ was synthesised and reacted with cyclohexane in the presence of 10 equivalents of H_2O_2 and 1000 equivalents of H_2O. Cyclohexanol and cyclohexanone products were obtained in a ratio of 12:1 at a 65% yield with respect to the iron

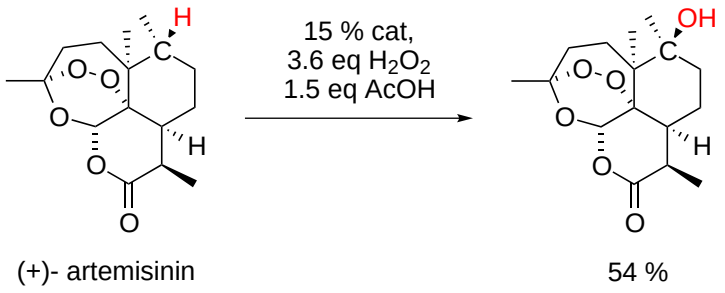

Scheme 1.1: Selective oxidation of (+)-artemisim.

complex. The high selectivity for the alcohol product over the ketone product, coupled with the high yield of oxidised products demonstrated for the first time potential practical applications of biomimetic catalysts. Mechanistic studies again implicated the involvement of an HO-Fe(V)=O active species,[22] demonstrating that high-valent metal-oxo species are capable of selectively activating strong C-H bonds.

The rapid development in this field since Que's initial report in 1997 is best exemplified by considering the (S,S)-1,1'-bis(pyridin-2-ylmethyl)-2,2'-bipyrrolidine (PDP) (Figure 1.5) based system reported by White and co-workers.[24] $[Fe(S,S\text{-}PDP)(NCCH_3)_2](SbF_6)_2$ was reacted with a host of substrates in the presence of 3.6 equivalents of H_2O_2 and 1.5 equivalents of acetic acid. Addition of acetic acid has been previously shown to improve oxidation yields.[25,26] In the oxidation of cyclohexane, cyclohexanone was obtained in a 92% yield, demonstrating a significantly greater selectivity than the systems developed by Que and Costas (*vide supra*).[24] The PDP system was also shown to selectively and predictably oxidise sp^3 C-H bonds. The electrophilic catalyst preferentially attacks the most electron rich C-H bond, thus can be directed by electron withdrawing groups, with complete retention of stereochemistry.[24] It was also demonstrated that the PDP catalyst preferentially attacks the least sterically crowded C-H bond,[27,28] owing to the bulky catalyst.[24] The predictable selectivity of this catalyst is best exemplified in the oxidation of (+)-artemisim

(Scheme 1.1). The most electron rich, sterically accessible sp^3 carbon atom, C10, is preferentially hydroxylated, while other functional groups such as the endoperoxo remain untouched.[24] The substrate scope of the PDP based catalyst has subsequently been expanded to the selective oxidation of sp^2 carbons to the corresponding ketones,[29] desaturation of aliphatic C-H bonds[30] and most recently nitrogen containing heterocycles.[31] This seminal work by White and co-workers highlights the potential utility of high-valent metal-oxos in catalytic systems.

1.3.2 Manganese Based Catalysts

Bioinspired manganese oxidation catalysts are significantly less well developed than their iron counterparts. This may be in part down to the fact that there are no examples of manganese containing oxygenases or dioxygenases found in nature. Nevertheless, manganese based catalytic systems have been developed and have shown promise in a variety of oxidation reactions. Perhaps the most well known class of manganese catalysts are those derived from 2,2-ethylene-*bis*-(nitrilomethylidene)diphenol (salen), originally reported independently by the groups of Jacobsen and Katsuki.[32,33] These were shown to be capable catalysts in the asymmetric epoxidation of alkenes. These reactions were proposed to proceed *via* a postulated $Mn^{V}{\equiv}O$ oxidant, generated through the reaction of a Mn^{III} precursor with iodosylbenzene. While there is experimental support for the presence of the $Mn^{V}{\equiv}O$ in the reaction mixture,[34,35] mechanistic studies confirming the role of this species are still absent from the literature. Furthermore, the nature of the active oxidant has been shown to be highly dependent on the oxidant employed in the reaction protocol. For example, when *meta*-chloroperbenzoic acid (*m*CPBA) was used as the oxidant, no evidence for a $Mn^{V}{\equiv}O$ was observed and the active oxidant

was proposed as a Mn^{III}–OOCOAr (acyl peroxo) species.[34] The reactivity of a variety of salen systems towards alkenes has been extensively investigated and comprehensively reviewed.[36] Importantly, Jacobsen catalysts are widely employed industrially in the epoxidation of olefins owing to their superior enantioselectivities. This is a direct result of the reaction proceeding *via* a metal-bound oxidant.[37] This highlights the potential utility of bioinspired catalysts.

In addition to the salen type systems, a selection of polyamine based catalysts have more recently been developed, and are proposed to react *via* high-valent manganese-oxo intermediates in analogy with their iron counterparts.[34] In general, these catalysts are tetradentate nitrogen donor ligands derived from enantiopure backbones similar to PDP (Figure 1.5). They have been shown to be capable of catalysing the asymmetric epoxidation of a variety of simple alkenes such as chalcones or styrenes with high enantioselectivity, utilising H_2O_2 as the oxidant.[38–55] Furthermore, as with the iron systems the addition of carboxylic acids has been shown to significantly enhance the reactivity of the catalyst. However, mechanistic studies are significantly lacking when compared to the analogous iron systems. The active oxidants are proposed to resemble those postulated for iron *i.e.* HO-Mn^{V}≡O.[34] While these studies into manganese based systems are in their infancy, it is undeniable that they will constitute an important family of catalysts in the future, owing to the significance of epoxidation reactions and their ability to make use of a green oxidant such as H_2O_2. This once again highlights the crucial role metal based oxidants, in particular metal-oxos can play in oxidation catalysis and in doing so, identifies the need to better understand the factors that effect the reactivity of these systems.

1.3.3 Cobalt Based Catalysts

Examples of cobalt based hydrocarbon oxidation catalysts in the literature are rare. However, there are reports worth note. Journaux and co-workers have described a catalyst derived from *o*-phenylenebis(*N*-methyloxamidate) (Me_2opba) (Scheme 1.2). This dianionic oxamide ligand was used to synthesise the corresponding square planar $[Co^{III}(Me_2opba)]^+$ complex.[56] This complex was then shown to activate dioxygen in the presence of pivaldehyde and was capable of oxidising secondary alcohols to the corresponding ketones. The authors speculate that the active oxidant is most likely a Co^{IV}=O. Similarly, the dianionic 4,5-di-chloro-1,2-bis(2-pyridine-2-carboxamido)benzene (H_2bpc) (Scheme 1.2) has been used to synthesise $[Co^{III}(bpc)Cl_2]^+$.[57] This complex was shown to catalyse the epoxidation of a variety of alkenes, using *m*CPBA as the oxidant. In the presence of protic solvents, the authors invoke the formation of a Co^{V}=O as the active oxidant. In both of these examples, it is proposed that the formation of the putative high-valent cobalt species is promoted by the highly basic nature of the ligand.

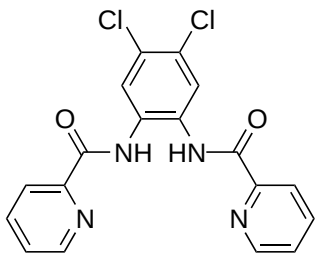

H_2bpc

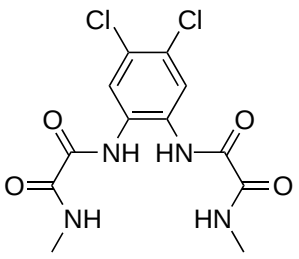

Me_2opba

Scheme 1.2: Ligands used in the synthesis of cobalt oxidation catalysts.

1.3.4 Nickel Based Catalysts

Numerous examples exist in the literature of nickel catalysts which are proposed to perform oxidation reactions *via* high-valent Ni-oxo species. The first of these was reported by Kochi and Koola, who showed that a Ni^{II} 1,4,8,11-tetraazacyclotetradecane (cyclam) species could epoxidise and/or hydroxylate olefins in the presence of iodosyl benzene. In these reactions, a Ni^{IV}=O was proposed as the most likely active oxidant. Burrows and co-workers have shown that a salen complex of Ni^{II} would epoxidise a variety of olefins in the presence of NaOCl. In this instance it was speculated that the active oxidant could be either a Ni^{III}–$O^{\bullet}$ or Ni^{III}–OCl species.[58] The Journaux and Bhatt groups have separately reported the synthesis of Ni^{II} complexes, of oxamide[59] or chiral Schiff base ligands[60] respectively. These complexes were capable of activating dioxygen to affect the epoxidation of a variety of alkenes. In both of these examples, a Ni^{IV}=O is proposed as the active oxidant. More recently, studies in this area have moved to parallel those ongoing with iron catalysis in both the choice of substrate and oxidant. The Itoh group have reported numerous examples of Ni^{II} catalysts, containing TPA as well as several derivatives.[61–63] Employing *m*CPBA as the oxidant, they have shown that these complexes can hydroxylate cyclohexane with high selectivity for the alcohol product over the over oxidised ketone product. Furthermore, these complexes have shown selectivity for the formation of primary over secondary alcohols in the oxidation of adamantane.[61–63] Similar high selectivity has been observed by other Ni^{II} catalysts in alkane oxidations utilising *m*CPBA.[64,65] In all of the aforementioned catalytic cycles, metal based oxidants are used to account for the high selectivty. These oxidants have been proposed to include Ni^{II}–$O^{\bullet}$, Ni^{III}=O and Ni^{IV}=O however, little to no direct experimental evidence of the existence of such oxidants has been put forward to substantiate these claims.

1.3.5 Copper Based Catalysts

Copper salts and simple copper complexes are widely employed as oxidation catalysts.[66] These reactions have been proposed to proceed by a range of mechanisms and consequently, the majority of these systems are beyond the scope of this thesis.[66] Nevertheless, in some cases, such as the oxidation of cyclohexane with $CuCl_2$ in the presence of a peracid, an aldehyde and crown-ether, these catalysts have been proposed to operate *via* a Cu^{III}–$O^{\bullet}$ or a Cu^{IV}=O reactive intermediate.[67] Similarly, a [Cu(1,10-phenanthroline)Cl] catalyst has been shown to oxidise alcohols *via* a proposed Cu^{III}–$O^{\bullet}$.[68]

1.3.6 Summary of Biomimetic Catalysis

The development of these highly active biomimetic catalysts which utilise high-valent metal based oxidants allow C-H bonds to be considered as functional groups, in the same manner as aldehydes or carboxylic acids; opening the door to the selective oxidation of hydrocarbon feedstocks to more valuable chemicals. In order to make progress towards more selective and/or stronger oxidants we must endeavour to rationalise the fundamental behaviour of the metal-based oxidants that are responsible for this reactivity. In the case of the iron and manganese systems, advances in model complex systems are providing revealing insights into the behaviour of these metal-oxo species; paving the way for the development of more advanced catalytic systems. However, for the late transition metals (Co, Ni, Cu and Zn) model complexes are absent from the literature (*vide infra*), leaving a gap in our understanding of these systems. It is therefore imperative that we strive to identify conditions that will allow us to isolate and study such species.

1.4 Model Complexes

It is apparent from the above discussion that high-valent metal-oxos are potent and synthetically useful oxidants. It is important therefore that we attempt to understand the origin of this reactivity. A significant body of work has already exists on haem-iron systems,[69] akin to cytochrome P450 and to a lesser extent on non-haem, di-iron systems, based on MMO.[70] This thesis will focus on mononuclear, non-haem, metal-oxo species; which display a more diverse range of reactivity. Recently, significant attention has been focused on the use of model complexes to isolate reactive intermediates and probe the associated structure reactivity relationships. Before discussing the model complexes, which have been isolated, in detail, it is important to consider what we hope to learn by carrying out these studies and importantly, how to achieve these goals.

The high-valent metal-oxo intermediates discussed above have all been postulated to react as electrophilic oxidants in HAA reactions. This is the reactivity we wish to probe using model complexes. Consequently, we require

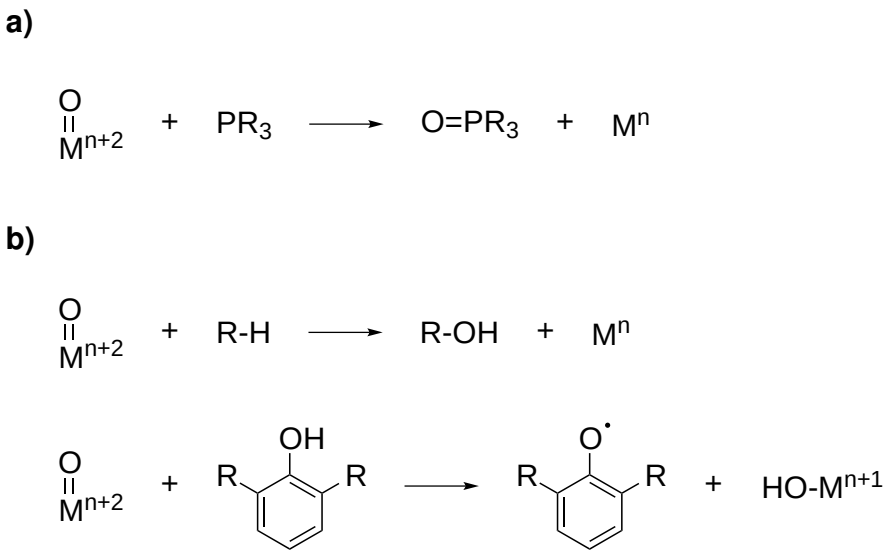

Figure 1.6: Chemdraw representation of a) oxygen atom transfer and b) hydrogen atom abstraction by a high valent metal-oxo species, $O=M^{n+2}$.

substrates which are prone to react in this manner. By analysing the products and kinetic data resulting from the reaction of these substrates with the metal-oxo species, we can gain insights into the underlying mechanisms.

The electrophilic character of metal-oxo based oxidants is generally assesed using nucleophiles that are susceptible to oxygen atom transfer (OAT). These include phosphines such as triphenylphosphine and thioethers such as thioanisole, which are oxidised to triphenylphosphine oxide and methyl phenyl sulphoxide respectively. This is summarised in Figure 1.6a. Similarly, HAA reactivity is probed using substrates that contain weak X-H bonds and is summarised in Figure 1.6b. Substrates typically include hydrocarbons such as 9,10-dihydroanthracene (DHA) or cyclohexadiene (CHD) and various substituted phenols such as 2,6-di-*tert*butylphenol (DTBP). These compounds have bond X-H bond dissociation energies of 78, 77 and 82 kcal mol^{-1} respectively;[71,72] significantly lower than that of methane (104 kcal mol^{-1}) for example.[73] This means that hydrogen atom abstraction reactions involving these reagents are relatively facile. These molecular probes have been used in conjunction with a variety of spectroscopic techniques in unravelling the chemistry of model high-valent metal-oxo complexes.

1.4.1 Reactive S = 1 Iron (IV) Model Complexes

Non-haem iron complexes are by far the most populated class of model complexes. The major breakthrough in this field came in 2003 when Que and co-workers isolated and crystalographically characterised an Fe^{IV}-oxo complex of 1,4,8,11-tetramethyl-1,4,8,11-tetraazacyclotetradecane (TMC); $[Fe^{IV}(TMC)(NCCH_3)(O)](OTf)_2$.[74] The $[Fe^{II}(TMC)(OTf)_2]$ starting material was reacted with the OAT reagent, iodosyl benzene to give the corresponding Fe^{IV}=O species. This provided the first unequivocal evidence for the existence

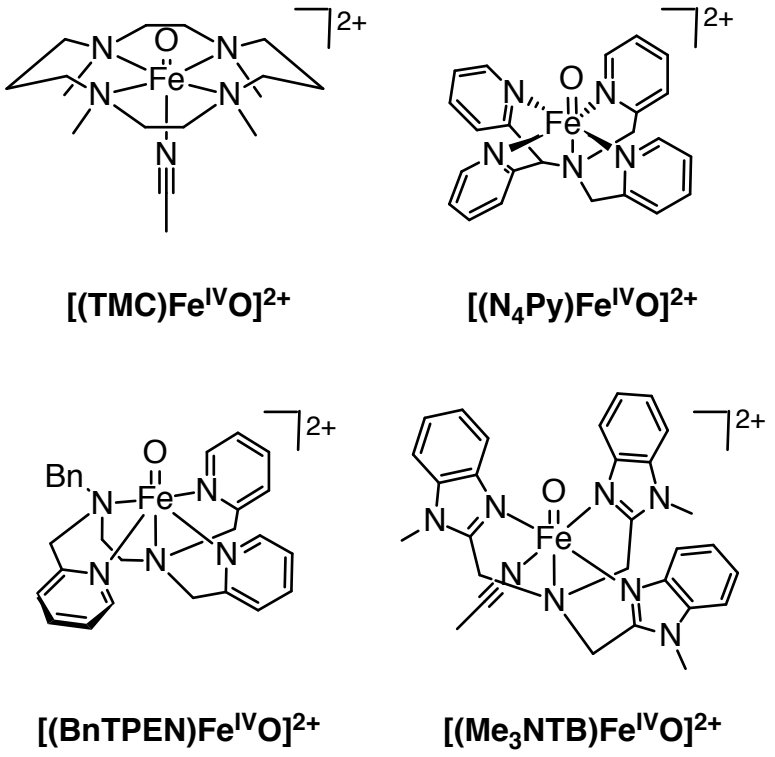

Figure 1.7: A selection of S = 1 reactive Fe^{IV}=O complexes.

of a terminal non-haem Fe^{IV}=O, validating its inclusion as an intermediate in previously postulated reaction mechanisms of non-haem enzymes (*vide supra*). The high stability of this complex is attributed to steric protection provided by the unusual coordination mode of TMC where the four methyl groups are orientated *anti-* to the oxo group; creating a protective pocket from the methylene CH_2 groups on the ligand skeleton. This allowed for the reactivity of the metal-oxo moiety to be investigated. Notably, of the nine crystal structures of terminal Fe^{IV}=O registered in the Cambridge structural database, four of those contain a TMC derived moiety;[74–77] exemplifying the strong stabilising effect this macrocycle has on these species. Interestingly, Que and co-workers have recently isolated an analogous complex in which the methyl groups are *syn-* to the oxo group.[77] It will be fascinating to observe the effect this has on the stability and reactivity of the complex.

The reactivity of $[Fe^{IV}(TMC)(NCCH_3)(O)](OTf)_2$

was probed using the substrates discussed above.[74,78] Upon reaction of $[Fe^{IV}(TMC)(NCCH_3)(O)](OTf)_2$ with triphenyl phosphine, triphenylphosphine oxide was observed in the post reaction mixture. Furthermore, when the ^{16}O atom was replaced with ^{18}O to give $[Fe^{IV}(TMC)(NCCH_3)(^{18}O)](OTf)_2$, the triphenylphosphine oxide product was found to contain ^{18}O.[74] These observations showed that $[Fe^{IV}(TMC)(NCCH_3)(O)](OTf)_2$ was an electrophilic oxidant and confirmed the oxygen atom in the product was derived from the metal-oxo moiety.[78] $[(TMC)Fe^{IV}O(NCCH_3)]$ was also shown to react with 2,4-di-*tert*-butylphenol to give 2,2′-dihydroxy-3,3′,5,5′-tetra-*tert*-butylphenol. The observed product was formed after abstraction of a hydrogen atom from the phenol and subsequent coupling of two phenoxyl radicals. This result indicated that $[Fe^{IV}(TMC)(NCCH_3)(O)](OTf)_2$ was capable of performing HAA. This conclusion was supported by the fact that two equivalents of $[Fe^{IV}(TMC)(NCCH_3)(O)](OTf)_2$ were shown to react with one equivalent DHA, CHD or xanthene, as a one electron oxidant.[78] This reaction resulted in an Fe^{III}-OH byproduct which is not a sufficiently powerful enough oxidant to further oxidise the substrates. Significantly, these results provided the first direct evidence for the electrophilic oxidising capebilities of an Fe^{IV}=O. The rates observed in the reaction of $[Fe^{IV}(TMC)(NCCH_3)(O)](OTf)_2$ with hydrocarbons were found to be low when compared with other Fe^{IV}=O complexes (*vide infra*). This has been attributed to the steric inaccessibility of the Fe^{IV}=O unit in $[Fe^{IV}(TMC)(NCCH_3)(O)](OTf)_2$.

As well as conducting reactivity studies, spectroscopic characterisation was also carried out on the complex. Importantly, $[Fe^{IV}(TMC)(NCCH_3)(O)](OTf)_2$ contained no chromophoric ancilliary ligands, unlike haem systems, which lead to an absense of any intense transitions in the visible spectrum. This allowed the identification of a near-infrared feature at 824 nm in the UV-Vis, determined to be a characteristic feature of an S = 1 Fe^{IV}=O in C_{4v}

symmetry.[79] This subsequently led to the characterisation of a plethora of Fe^{IV}=O intermediates, the number of which now exceeds 50.[80] In general, these species are stabilised by ligands containing strong σ-donor atoms such as tertiary amines or polypyridines. A few noteworthy examples are considered below.

The pentacoordinate polypyridyl ligand 1,1-di(pyridin-2-yl)-*N*,*N*-bis(pyridin-2-ylmethyl)methanamine (N_4py) was utilised by Que and co-workers to isolate the corresponding Fe^{IV}=O (Figure 1.7).[81] The thermal stability of $[Fe^{IV}(N_4py)(O)]^{2+}$ allowed for characterisation by X-ray crystallography; this also meant that the reactivity of $[Fe^{IV}(N_4py)(O)]^{2+}$ towards cyclohexane at room temperature could be investigated. Cyclohexanol was observed in the post reaction mixture. This, coupled with a non-classical kinetic isotope effect (KIE), showed that $[(N_4py)Fe^{IV}O]$ is capable of hydroxylating the relatively strong C-H bond in cyclohexane (BDE=99 kcal mol^{-1}) *via* HAA.[81] Similar results were obtained for the complex based on *N*-benzyl-*N*,*N*′,*N*′-tris(2-pyridylmethyl)ethane-1,2-diamine) (Bn-TPEN) $[Fe^{IV}(BnTPEN)(O)]^{2+}$.[81] Closely related to $[Fe^{IV}(BnTPEN)(O)]^{2+}$ is the tris((1-methyl-1H-benzoimidazol-2-yl)methyl)amine (Me_3NTB) based system, $[Fe^{IV}((Me_3NTB))(O)]^{2+}$.[82] This system represents the most reactive S = 1 Fe^{IV}=O isolated to date. For example, in the oxidation of cyclohexane at -40 °C, $[Fe^{IV}((Me_3NTB))(O)]^{2+}$ showed a significantly higher second order rate constant (k_2= 0.25 M^{-1} s^{-1}) than observed for either $[Fe^{IV}(N_4py)(O)]^{2+}$ (k_2= 0.000055 M^{-1} s^{-1}) or $[Fe^{IV}(BnTPEN)(O)]^{2+}$ (k_2= 0.00039 M^{-1} s^{-1}) at 25 °C.[81] The fact that $[Fe^{IV}((Me_3NTB))(O)]^{2+}$ displayed significantly higher reactivity at lower temperature than any of the other systems described above indicates that it is an extremely potent oxidant.

1.4.2 Reactive S = 2 Iron (IV) Model Complexes

The unprecedented reactivity of $[Fe^{IV}(Me_3NTB)(O)]^{2+}$ has been attributed to the existence of a low-lying, highly reactive, S = 2 excited state.[82] The reasons for this postulated increased reactivity of high-spin species are discussed in more detail below. On closer inspection of the well characterised enzymatic metal-oxo intermediates, it is apparent that the species observed in nature exclusively have S = 2 ground states. This has long led to the assumption that S = 2 states are inherently more reactive, as they have been favoured by natural selection. Consequently, significant effort has been devoted to developing S = 2 model complexes.

Most of the S = 2 non-heme iron systems isolated to date have featured the tris(2-aminoethyl)amine (tren) framework. These systems are of trigonal rather than tetragonal symmetry; like those complexes discussed above. This causes the d_{xy} and $d_{x^2-y^2}$ to become degenerate and favours electrons singly occupying these orbitals, to give S = 2 systems, rather than pairing in the d_{xy} orbital to give S = 1

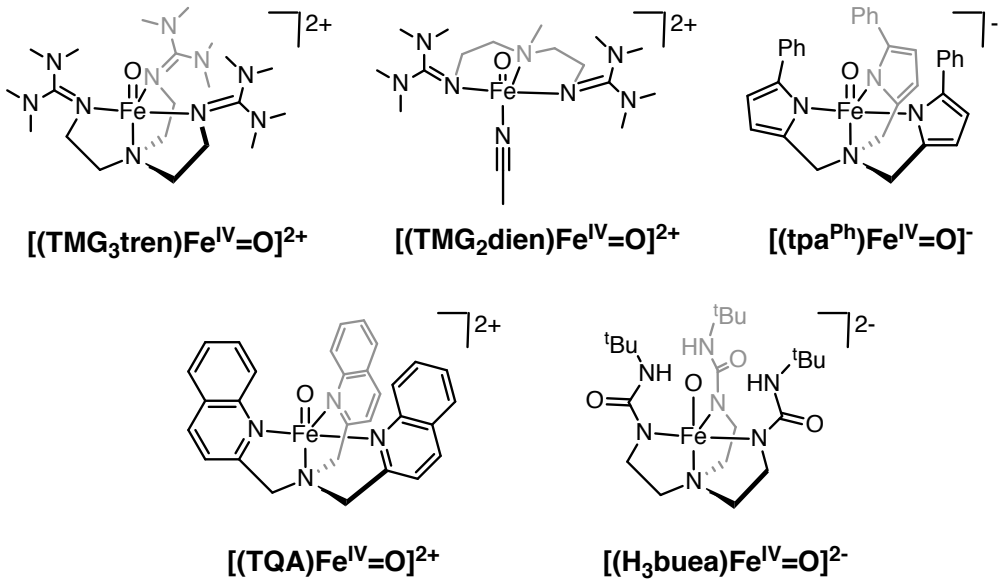

Figure 1.8: High Spin, S = 2, Fe=O complexes.

systems (*vide supra*).

Que and co-workers were the first to isolate and crystalographically characterise such a system, utilising 2,2′-(((2-((*bis* (dimethylamino)methylene) amino)ethyl)azanediyl) *bis*(ethane-2,1-diyl))*bis* (1,1,3,3-tetramethylguanidine) (TMG_3tren). $[Fe^{II}(TMG_3tren)(OTf)][OTf]$ was reacted with iodosyl benzene to give $[Fe^{IV}(TMG_3tren)(O)]^{2+}$.[83] This S = 2 complex was shown to react with DHA and CHD *via* HAA although at a rate not appreciably different to $[Fe^{IV}(TMC)(NCCH_3)(O)](OTf)_2$. This lower than expected reactivity was attributed to the high degree of steric shielding afforded to the Fe=O moiety by the bulky tetramethylguanidine groups. In order to test this hypothesis, one of the arms of TMG_3tren was removed to give 2′,2′-((methylazanediyl)*bis*(ethane-2,1-diyl))*bis*(1,1,3,3-tetramethylguanidine) (TMG_2dien). The related complex $[Fe^{IV}(TMG_2dien)(NCCH_3)(O)]^{2+}$ was synthesised and shown to be significantly more reactive than $[Fe^{IV}(TMG_3tren)(O)]^{2+}$ in the oxidation of CHD and DHA. $[Fe^{IV}(TMG_2dien)(NCCH_3)(O)]^{2+}$ was also shown to be an order of magnitude more reactive in these reactions than $[Fe^{IV}(TMC)(NCCH_3)(O)](OTf)_2$ and $[Fe^{IV}(N_4py)(O)]^{2+}$ but not as reactive as $[Fe^{IV}(Me_3NTB)(O)]^{2+}$. This suggests that while the spin state of these complexes is an important factor in determining reactivity, steric and thermodynamic considerations regarding the different ligand environments must also be taken into account.[84] This sentiment is further echoed in the work of both the Borovik and Chang groups. Chang and co-workers have isolated the tren derived $[Fe^{IV}(tpa^{Ph}(O))]^-$ species and showed that while it is capable of oxidisng CHD to give benzene, it does not react with DHA or xanthene.[85] Similarly, Borovik and co-workers have shown that while the S = 2 complex $[Fe^{III}(H_3buea)(O)]^{2-}$ is reactive towards HAA, the bulky *tert*-butyl groups sterically shield the metal-oxo moiety, tempering the reactivity.[86] These examples once again demonstrate that steric accessibility to the metal-oxo moiety is a key factor in promoting reactivity. Que and co-workers have also

reported the synthesis and characterisation of $[Fe^{IV}(TQA)(NCCH_3)(O)]^{2+}$.[87] This complex shows the highest rate of HAA towards cyclohexane (as well as other more reactive hydrocarbons) to date, with k_2= 0.35 M^{-1} s^{-1}, compared to k_2= 0.25 M^{-1} s^{-1} for $[Fe^{IV}(Me_3NTB)(O)]^{2+}$. This data suggests that a S = 2 ground state may be favourable in generating more reactive metal-oxo based oxidants.

1.4.3 Iron (V) Model Complexes

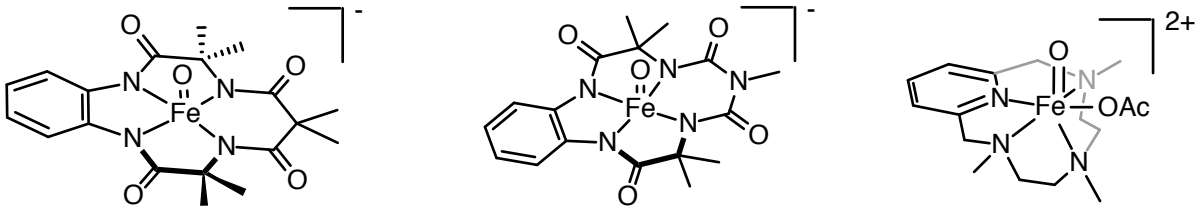

Figure 1.9: Examples of Fe^{V}=O complexes.

While the Fe^{IV}=O model complexes discussed above mimic the reactivity observed in some non-haem enzymes, the mechanisms proposed for the catalysts discussed in 1.3 as well as cytochrome P450 invoke Fe^{V} oxidants. The first Fe^{V}=O model complex reported was by Collins and co-workers,[88] and was supported by a tetra amido macrocyclic ligand (TAML) (Figure 1.9). The high oxidation state of the metal is stabilised by the tetra anionic nature of the ligand. Collins showed that $[(TAML)Fe^{V}=O]^{-}$ reacted as an electrophilic oxidant with triphenylphosphine and thioanisole to give the corresponding OAT products. Furthermore, it was shown to react with hydrocarbons such as DHA, ethyl benzene and cyclohexane *via* HAA.[88,89] A drawback of this particular TAML system is that the complex is only stable between -60 °C and -40 °C therefore the discovery of an Fe^{V}=O complex based on the Biuret containing TAML (Figure 1.9), which was stable at room temperature marked a significant advancement. Again, the reactivity of the Fe^{V}=O was investigated

and the biuret containing TAML complex was found to be capable of oxidising a range of hydrocarbons including cyclohexane.[90]

The exceptionally strong amido σ-donor ligands of TAML are significantly better at stabilising the Fe^{V} oxidation state compared to the neutral polypyridyl and/or amine ligand environments employed in both the iron based catalysts and model complexes discussed above. Therefore, it is difficult to draw direct comparisons between the reactivity of Fe^{V} *vs.* Fe^{IV} oxidants or make any mechanistic inferences with regards to the catalysts. An important breakthrough therefore was the discovery of an Fe^{V}=O supported by a neutral 3,6,9-trimethyl-3,6,9-triaza-1(2,6)-pyridinacyclodecaphane ($PyNMe_3$) ligand (Figure 1.9). Costas and co-workers showed how a putative $[Fe^{V}(PyNMe_3)(O)]^{3+}$ intermediate was capable of activating strong C-H bonds, such as those in cyclohexane, at fast reaction rates. Remarkably, this complexes showed the highest k_2 value; reacting with cyclohexane an order of magnitude faster than the Me_3NTB complex and four orders of magnitude faster than the TAML complexes shown in Figure 1.9. Unlike the TAML complexes, the $PyNMe_3$ complex was shown to turnover catalytically. This complex was shown to be site selective in substrates with multiple C-H bonds and also to react with a high degree of stereoretention. This represents an incredibly elegant example of model complex chemistry because the reactive intermediate was able to be characterised and displayed highly selective reactivity.

To date, only a single example of an HO-Fe^{V}=O exists. Using variable temperature mass spectrometry, Costas and co-workers were able to identify an HO-Fe^{V}=O oxidant, like those invoked in the catalytic cycles of the iron based oxidation catalysts.[91] Structurally characterising such a species is one of the challenges remaining in the field.

1.4.4 Manganese Model Complexes

As well as non-haem iron model complexes, non-haem manganese-oxo models have also been synthesised. In general, studies into these systems are significantly more scarce than their iron counterparts; nevertheless there are several examples that warrant discussion in this thesis.

As discussed above, the majority of the manganese based catalytic systems invoke high-valent $Mn^{V}\equiv O$ as the active oxidant. Collins was the first to report X-ray crystal structures of $Mn^{V}\equiv O$ species, generated from the reaction of Mn^{III} precursors with OAT reagents such as *tert*-butyl hydroperoxide.[92,93] Both of these complexes were supported by TAML ligands, which aided in the stabilisation of the high oxidation state of the metal. However, these complexes showed no OAT reactivity towards any substrates and were remarkably stable at room temperature. Collins subsequently showed that the addition of redox inactive metal ions, such as zinc, to the reaction mixture drove these complexes to react *via* OAT.[94] O'Halloran and co-workers later showed that a similar tetra-anionic ligand, 1,2-*bis*(2,2-diphenyl-2-hydroxyethanamido)benzene (H_4PHAB), was capable of forming the corresponding Mn-oxo complex, $[(PHAB)Mn^{V}\equiv O]^{-}$. This complex was formed by the reaction of a dimanganese(III) precursor with dioxygen and was subsequently shown to react *via* OAT with phosphines, ethers and olefins.[95] More recently, Nam and co-workers have reported the synthesis of a $Mn^{V}\equiv O$ supported by a TAML, by reaction of a Mn^{III} precursor with a hydrocarbon in the presence of dioxygen. The metastable $Mn^{V}\equiv O$ was then shown to react with triphenyl phosphine.[96] The Borovik group have reported an intriguing series of complexes, based on their 1,1′,1″-(nitrilotris(ethane-2,1-diyl))tris(3-(*tert*-butyl)urea) (H_6buea) ligand framework. The formation of a Mn^{III}–O complex was observed upon the reaction of a Mn^{II} precursor with dioxygen. This complex was shown to be reactive towards

substrates with weak C-H bonds such as DHA and CHD as well as hydrogen atom donors such as 2,6-diisopropylpiperidin-1-ol (TEMPO-H).[97] Interestingly, the driving force of this reactivity has been identified as the high O-H BDE of the $[(H_3buea)Mn^{II}\text{-}OH]^{2-}$ product, which was also isolated. The Mn^{III}–O was then sequentially chemically oxidised to the corresponding Mn^{IV}=O and Mn^{V}≡O. The Mn^{IV}=O was found to be unreactive towards PPh_3 however, oxidation of PMe_2Ph was observed.[98] While the reactivity (if any) of the Mn^{V}≡O is yet to be reported, its isolation represented the first example of a high spin Mn^{V}≡O, validating its inclusion as a reactive intermediate in the catalytic cycles of enzymes.[99] The manganese-oxos described above are all stabilised by powerfully electron donating ligands. Consequently, their reactivity is tempered. However, there are also several reports of Mn^{IV}=O stabilised by polypyridine ligands. For example Bn-TPEN and N_4py have both been utilised to form reactive Mn^{IV}=O species. $[(N_4py)Mn^{IV}(O)]^{2+}$ was shown to oxidise ethyl benzene.[100] Interestingly, the corresponding $[(Bn\text{-}TPEN)Mn^{IV}(O)]^{2+}$ complex was found to oxidise ethyl benzene at a rate five times faster than the N_4py analogue. $[(Bn\text{-}TPEN)Mn^{IV}(O)]^{2+}$ was also found to react with cyclohexene, cyclohexane, benzyl alcohol, napthalene and thioanisole; making it the most reactive $Mn^{IV}(O)$ described to date.[101] Nam and co-workers have gone on to describe how the reactivity of both the N_4py species and the Bn-TPEN species can be tuned through the binding of redox innocent lewis acids or triflic acid.[102–104] With the exception of $[(Bn\text{-}TPEN)Mn^{IV}(O)]^{2+}$, $Mn^{IV}(O)$ generally show significantly lower reactivity than their iron counterparts *i.e.* they are only capable of activating weak C-H bonds.

The discussion of these manganese-oxo species has been limited to include non-haem species in which the active oxidant has been proposed as a terminal metal-oxo. A multitude of porphyrin based species have also been described in the literature. In such species, a Mn^{V}≡O is also postulated to act as an oxidant.

While they are beyond the scope of this thesis, Talsi and Bryliakov have recently published a comprehensive review on this subject.[105]

1.5 The Oxo Wall

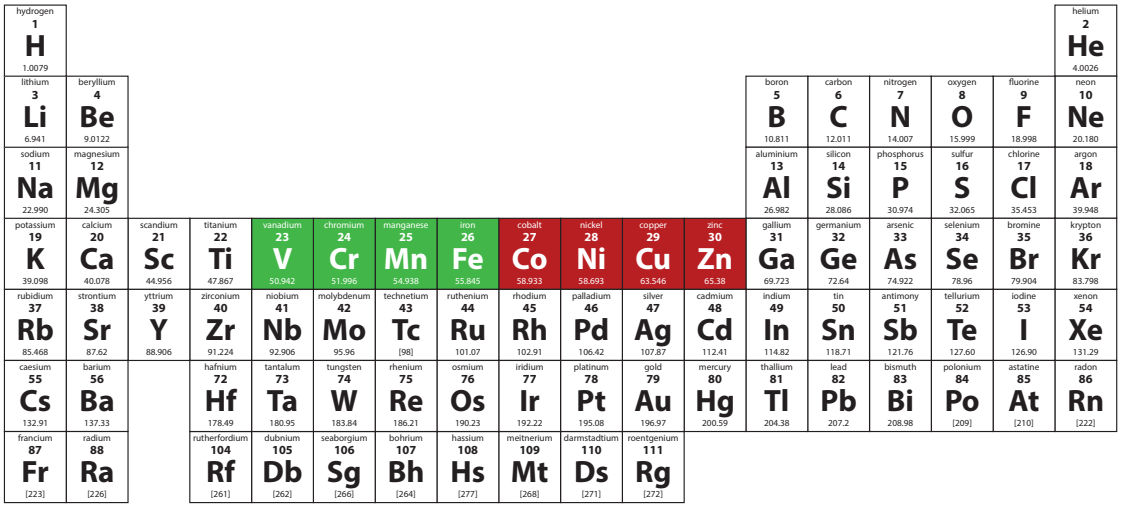

Figure 1.10: The oxo wall. Metal-oxos containing metals from groups 5-8 are numerous, those from 9 onwards are not.

From the above discussion in section 1.4 it is evident that while metal-oxos containing metals from groups 5-8 are numerous, those from 9 onwards are not (Figure 1.10). In order to understand the reason for this it is necessary to consider the molecular orbital approach to the bonding in these species, developed by Ballhausen and Gray.

Fundamentally, an oxo ligand can be thought of as a water molecule bound to a Lewis acidic metal, whose Brönsted acidity is, consequently increased to the extent that both protons are lost.[106] The resultant oxo ligand is formally O^{2-} and a highly electronegative σ donor. The metal-oxo moiety can be significantly stabilised through π donation of the orthogonal lone pairs on O^{2-} into the molecular orbitals of appropriate symmetry; forming a metal oxygen triple bond. The relative stability of this metal-oxygen bond is therefore inherently linked to the ligand field around the metal centre.[107,108]

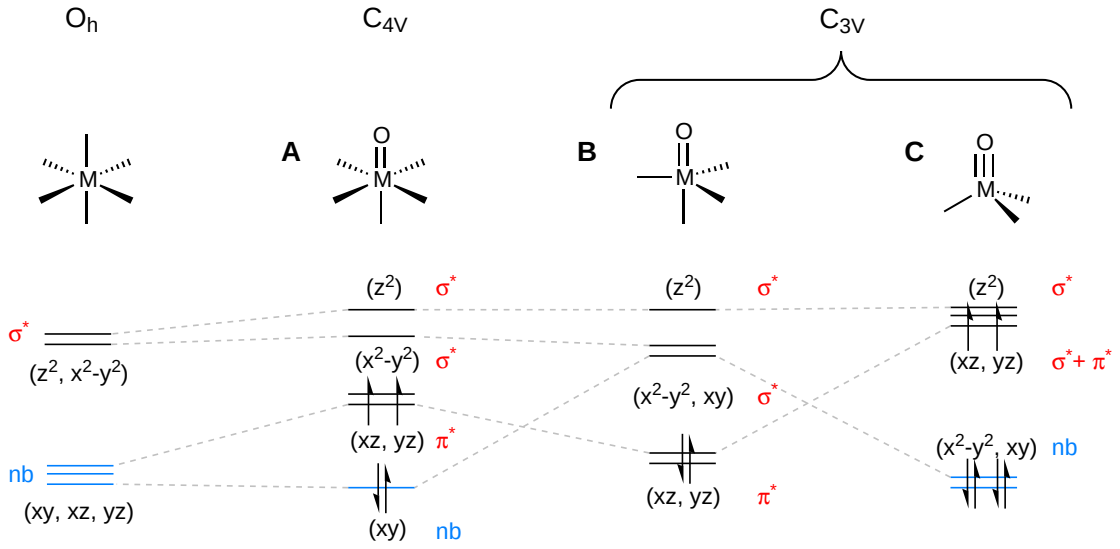

Figure 1.11: Metal-oxo Ligand Field Diagram for (A) tetragonal ligand field, (B) trigonal-bipyramidal ligand field and (C) tetrahedral ligand field.

A simple ligand field diagram for metal-oxo species in an octahedral environment can be derived by replacing an axial ligand of an octahedron with an O^{2-}.[106–110] As this newly introduced metal-oxygen bond is short, the degeneracy of the five *d*-orbitals is lost relative to the octahedral parent. Consequently, orbitals with a *z*-component are raised in energy while those without a *z*-component are lowered in energy. Standard ligand field considerations can then be applied to give the relative energies of the orbitals in other ligand fields.

In this model, the bonding orbitals are considered to be filled by the *s* and *p* electrons from both the metal and oxygen atoms, giving a formal metal-oxygen bond order of three. This metal-oxygen bond is formed through interaction of the O p_z and the metal d_{z^2} orbitals to give a σ bond and a π bond is formed through interaction of the O p_x and p_y orbitals with the metal d_{xz} and d_{yz} orbitals. Therefore, although the $d_{x^2-y^2}$ and d_{xy} orbitals are formally σ^* antibonding with respect to the equatorial ligands, they are non-bonding with respect to the metal oxygen bond. The remaining non-bonding and anti-bonding orbitals depicted

in Figure 1.11 are then populated only after the addition of d-electrons. Thus, *d*-electron count directly influences metal-oxygen bond order.

1.5.1 Metal-Oxos in a Tetragonal Ligand Field and The Oxo Wall

Figure 1.11A shows a metal-oxo in a tetragonal field. This diagram is derived as discussed above. The (d_{xz}, d_{yz} and d_{z^2}) are raised in energy relative to the octahedral parent whereas the ($d_{x^2\text{-}y^2}$ and d_{xy}) are lowered in energy. Thus, it is apparent from Figure 1.11 that a metal-oxygen bond order of three is maintained for d^2 configurations as the first two *d*-electrons populate non-bonding orbitals. However, addition of two further *d*-electrons populates the anti-bonding d_{xz} and d_{yz} orbitals, reducing the metal-oxygen bond order to two.

This logic has given rise to the concept of an 'oxo wall' which states that metal-oxos in a tetragonal ligand field are stable only up to a *d*-electron count of 4. Configurations of $d^{>4}$ lead to the loss of any metal-oxygen multiple bond character. This results in highly basic M-O moieties which are exceptionally susceptible to attack by protons or electrophiles. Therefore, as we traverse the transition metals, and add more *d*-electrons to the system, the metal-oxo units become progressively more unstable. The higher oxidation states that would be required to stabilise these metal-oxos become progressively more unattainable thus explaining the dearth of metal-oxos from group 9 onwards.

1.5.2 Metal-Oxos in a Trigonal Bipyramidal Ligand Field

Several of the model complexes discussed in 1.4 adopt trigonal bipyramidal geometry. Extending the oxo-wall logic to these systems (Figure 1.11B) allows us to arrive at the conclusion that we would expect only low spin $d^{\geq 2}$ and high

spin d^4 metal-oxo complexes to be stable. This principle was used by Que and co-workers to synthesise the first S = 2 Fe=O, which has a d^4 configuration.[83]

1.5.3 Metal-Oxos in a Tetrahedral Ligand Field

Figure 1.11C shows the interesting case of a tetrahedral ligand field. Lowering the coordination number of the metal to four (compared to six) in the parent octahedral complex frees up orbitals that were previously involved in bonding with the equatorial ligands. Consequently, the lowest lying orbitals are a pair of degenerate non-bonding orbitals ($d_{x^2\text{-}y^2}$ and d_{xy}). These orbitals can accommodate four *d*-electrons without destabilising the metal-oxygen triple bond. Therefore, configurations of up to $d^{\geq 6}$ are predicted to be stable in a tetrahedral ligand field. Interestingly, experimental results have shown that the antibonding nature of the d_{z^2} orbital can be significantly mitigated through mixing with the 4*s* and $4p_z$ orbital.[111] This has led Ray to conclude that the d_{z^2} can be considered non-bonding. This implies that *d*-electron counts of up to eight can be tolerated in a tetrahedral ligand field.[109]

Based on this argument, we hypothesise that by enforcing a tetrahedral co-ordination environment around the metal centre, we will be able to stabilise transition metal-oxos with high *d*-electron counts *i.e.* we will be able to form late transition metal-oxos.

1.5.4 Why Hurdle the Oxo-Wall

In section 1.1, the potential utility of selective hydrocarbon oxidation was outlined. In summary, the facile and selective oxidation of hydrocarbons is still something which eludes chemists. In section 1.2, it was demonstrated that enzymes are capable of utilising high-valent metal-oxos to activate some of the

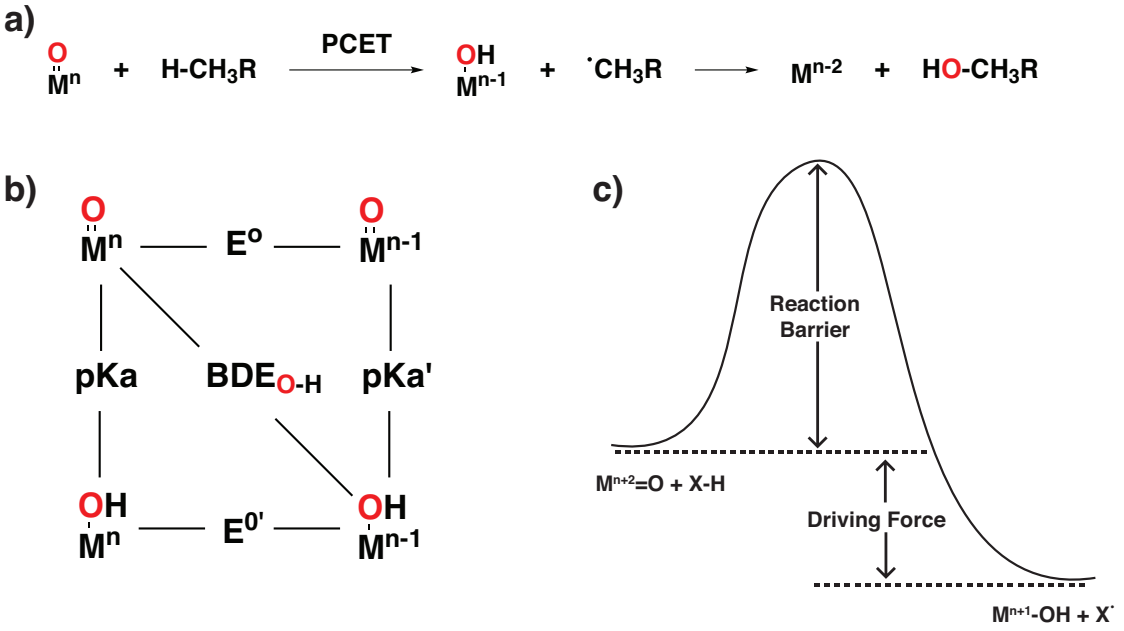

Figure 1.12: Factors that determine the reactivity of metal-oxo species. a) A general reaction scheme for the hydroxylation of a hydrocarbon *via* HAA; b) A general scheme illustrating the relationship of the reduction potential of the metal, p*K*a of the oxo ligand and the $BDE_{O\text{-}H}$ of the reduced hydroxo product; c) A schematic representation of the driving force for HAA reactions.

strongest C-H bonds. Inspired by this, chemists have synthesised a library of model complexes, described in 1.4, which have been shown to activate C-H bonds such as those in cyclohexane, *via* HAA. We believe that this reactivity can be improved upon and stronger C-H bonds can be activated utilising metal-oxos. In order to rationalise how this could be achieved. We must consider the factors which effect HAA reactions.

A general scheme for the hydroxylation of a C-H bond through HAA by a metal-oxo is shown in Figure 1.12a. The hydrogen atom is abstracted by the M=O intermediate. The resulting hydroxo product then rebounds with the alkyl radical to form the hydroxylated product. HAA reactions fall into a class of reactions known as proton coupled electron transfer (PCET).[112,113] In these reactions, the transfer of the proton and electron (*i.e.* a hydrogen atom) is a concerted process. For transition metal based oxidants such as metal-oxos, the

electron is transferred to the metal centre and the proton is transferred to a basic ligand. Therefore, both the reduction potential of the metal and the p*K*a of the hydroxo group are important in determining the rate of PCET. Extensive studies by the Mayer group have shown that these quantities can be related by box diagrams such as those shown in figure Figure 1.12b. Importantly, Mayer has shown that the main factor governing HAA reactivity is the thermodynamic driving force *i.e.* the free energy of the reaction. Furthermore, it has been shown experimentally that this quantity can be directly related to the difference in BDE of the C-H bond in the reactants *versus* the O-H bond in the product.[112,113] Therefore in order to activate stronger C-H bonds, we must form stronger O-H bonds.[112–114] Based on the box diagram in Figure 1.12b, in order to form a stronger O-H bond, we must engineer a metal-oxo in which the metal centre is highly oxidising and the reduced form is highly basic.

These are properties we would expect of late transition metal-oxos.[115] As we traverse the transition metals from left to right, the ionisation energies of each atom increases as a result of increasing effective nuclear charge. This manifests in an increase in oxidation potential and means higher oxidation states are more unstable in late first row transition metal complexes *i.e.* these metal centres are highly oxidising. Furthermore, we believe that by increasing the *d*-electron count in metal-oxo species, we will further polarise the metal-oxygen bond as the increased population of the antibonding orbitals will lead to lengthening of the bond and an increase electron density located on the oxygen atom. We hypothesise that this will increase the basicity of the oxo ligand consequently forming a less acidic M^{n-1}-OH product with a higher O-H BDE.

Other theories regarding the reactivity of late transition metal-oxos have been proposed. Of particular note is the theory of exchange enhanced reactivity developed by Shaik.[116,117] This theory proposes that metal-oxos with high spin ground states are more reactive towards HAA as the number of exchange

interactions between unpaired electrons is higher, compared to low spin systems, increasing the relative stability of the high spin transition state. This concept has been extended to low spin systems with accessible high spin excited states such as the Me_3NTB complex discussed above. Similarly, Solomon has proposed that frontier molecular orbitals and consequently sterics play a key role in influencing HAA reactivity.[118] While both of these concepts may indeed be applicable in predicting the reactivity of transition metal oxo complexes, we believe that these differences are minor when compared to the thermodynamic driving force. As Mayer argues, while these factors are important, they merely contribute to the reaction barrier, and therefore indirectly influence the reactivity of transition metal-oxo complexes. To summarise, we believe that by hurdling the oxo-wall and synthesising late transition metal-oxos, we will generate extremely potent oxidants.

1.6 Beyond the Oxo Wall

As the discussion of the oxo wall (*vide supra*) implies, reports of elements multiply bonded to late transition metals are rare. However, there are several noteworthy examples in the literature which warrant consideration here.

1.6.1 Metal-Oxos Beyond the Wall

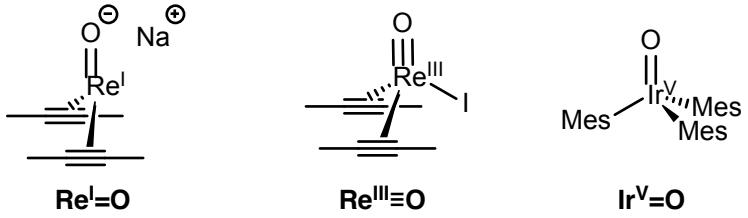

Figure 1.13: Metal-oxos beyond the oxo-wall. Re^{I} and Re^{III} oxos reported by Mayer,[119,120] as well as the Ir^{V}=O reported by Hay-Motherwell[121] which appear to violate the concept of the oxo-wall.

Mayer and co-workers have reported a d^6 Re^{I}=O (Figure 1.13).[119] The Re=O unit is stabilised as the molecule adopts approximate threefold symmetry *i.e.* it is not tetragonal. Furthermore, the metal *d*-orbitals engage in a significant backbonding interaction with the supporting alkyne ligands, stabilising the M=O bond. A d^5 Re^{III}=O has also been reported in a similar ligand environment (Figure 1.13).[120] Additionally, Hay-Motherwell and co-workers have reported the synthesis of a stable Ir^{V}=O complex (Figure 1.13).[121] In this instance, the unusually high oxidation state of iridium supported by the strongly electron donating mesityl groups; as well as the *pseudo*-tetrahedral adopted by the complex help to stabilise the Ir^{V} unit. Borovik has reported the synthesis of the intriguing $[Fe^{III}(H_3buea)(O)]^{2-}$, already discussed in section 1.4.2.[86] Formally Fe^{III}, this complex therefore has a d^5 configuration. Analysis of the X-ray structure of this complex showed a particularly long Fe-O bond length,

interpreted as a metal-oxygen bond order of one. This suggested that the high *d*-electron count was significantly stabilised by hydrogen bonding to the adjacent urea groups. Also of note is a [Cu^{III}=O] species observed in the gas phase and shown to react with alkanes such as ethane.[122]

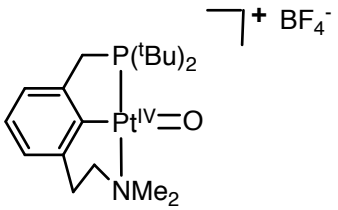

Figure 1.14: A Pt^{IV}=O. An example of a terminal late transition metal-oxo whose stability is owed primarily to the low coordination number of the ligand.[123]

Perhaps the most interesting report of a late transition metal-oxo is Milsteins d^6 [NCP(Pt^{IV}=O)] complex (Figure 1.14).[123] Importantly, unlike those discussed above, this complex is not stabilised by powerful electron donating or withdrawing ligands. Computational studies have suggested that the high stability of the Pt=O bond in this complex is a result of significant delocalisation of electron density from the compact 5*d*-orbitals to the more diffuse 6*s* and 6*p* orbitals. These findings are in agreement with NMR data obtained for the complex in which the ^{195}Pt signal is relatively downfield, indicating a loss of electron density around the metal centre. This terminal oxo is stable at room temperature and shows the expected reactivity patterns of a terminal oxo although it is not reactive towards strong C-H bonds. Crucially, this provides an example of a terminal late transition metal-oxo whose stability is owed primarily to the low coordination number of the ligand.

1.6.2 "Scandium-Capped" Metal-Oxos

Several reports have emerged in the literature of redox inactive Lewis acidic metal ions, such as Sc^{3+}, bound to metal-oxos. It has been postulated that

addition of these metal ions are capable of stabilising late transition metal-oxos through Lewis acid type interactions with the oxygen atom of the oxo moiety. Based on this principle, Ray and co-workers have reported a complex formulated as [(TMG_3tren)Co^{IV}-O-Sc] which they describe as a scandium capped oxo, implying no covalent interaction between the oxygen and scandium atoms.[124] This complex was shown to undergo OAT reactions with PPh_3 and HAA reactions with DHA. The oxidation state of the cobalt was assigned based primarily on electron paramagnetic resonance (EPR). A later report by Borovik and co-workers suggested that this data better fit a Co^{III} assignment.[125] The Ray group reported a second scandium capped Co^{IV}=O utilising a TAML ligand.[126] Again this complex was shown to perform OAT and HAA reactivity. While both of these complexes have been assigned as Co^{IV}–O–Sc species the EPR data reported by Borovik, suggests that they are better assigned as Co^{III}–O–Sc *i.e.* bimetallic species; with the scandium formally bonded to the oxygen atom. Thus, to date, there are no reports of late first row transition metal-oxos.

1.6.3 Metal-Oxygen Adducts

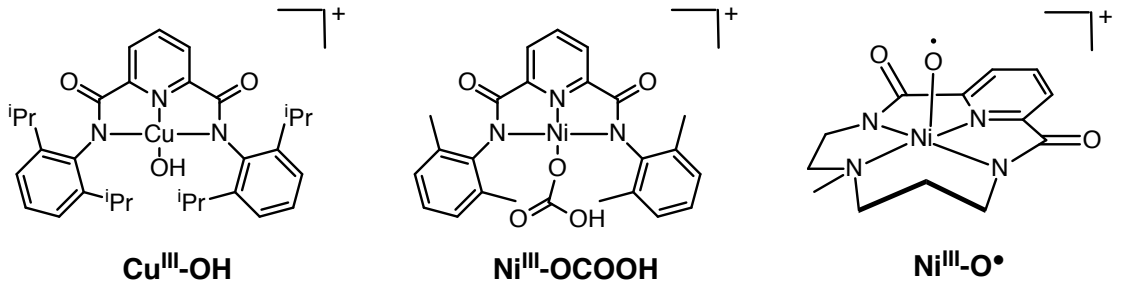

Figure 1.15: Metal-oxygen adducts. Tolmans [Cu^{III}–OH], McDonalds Ni^{III}–OCO_2H and Companys Ni^{III}–$O^{\bullet}$ have all shown reactivity towards hydrocarbons.[127–132]

Recently, several groups have reported the synthesis of late transition metal oxygen adducts. All of these complexes have been supported by a dianionic

dicarboxamide ligands, which posses N^- donor atoms. These strong σ-donors help in stabilising the high oxidation states of the metals.

The first of these complexes isolated was Tolmans [Cu^{III}–OH](Figure 1.15), which was shown to react rapidly *via* HAA with phenols and DHA.[127–130] Remarkably, the HAA reactivity of this complex is comparable to the most reactive terminal metal-oxos reported. This high reactivity was later ascribed to the high BDE (90 kcal mol^{-1}) of the O-H bond formed after HAA.[129]

There have also been reports of nickel oxygen adducts in the literature. The Ray group have described the formation of, what they assign to be, a Ni^{III}–O(H) species which is capable of oxidising PPh_3 and abstracting a hydrogen atom from DHA.[133] Although the reactivity profile of this compound reflects what would be expected of a terminal nickel-oxo, structural characterisation of this complex is lacking. While the EPR spectrum confirmed the assignment of the Ni^{III} oxidation state, it also showed that a mixture of two compounds was present. Furthermore, there is no data to suggest that the oxygen atom is in fact coordinated to the metal as the assignment of the Ni^{III}–O(H) core was based mainly on evidence obtained from mass spectrometry.

Within our group, we have reported the synthesis of a Ni^{III}–OCO_2H complex (Figure 1.15).[131] This was achieved through the one electron chemical oxidation of a well-characterised Ni^{II}–OCO_2H precursor. This complex was shown to react with substrates with weak C-H bonds such as phenols as well as oxidising PPh_3. However, Ni^{III}–OCO_2H did not react with C-H bonds. This Ni^{III} complex was well characterised. Extended x-ray absorption fine structure (EXAFS) data collected indicated that the Ni centre remained four coordinate after oxidation and that the primary coordination sphere comprised of N or O donor atoms. DFT calculations supported the assignment as Ni^{III}–OCO_2H, indicating that the bicarbonate was likely to stay bound in a monodentate fashion and the complex

likely to remain square planar. The assignment of a square planar geometry was also supported by the axial EPR signal, which also confirmed the unpaired electron was located on the metal. Interestingly, recent unpublished results suggest that an analogous acetate complex Ni^{III}–OAc is remarkably reactive towards C-H bonds.

Finally, Company and co-workers have reported the synthesis of a complex formulated as a Ni^{III}–$O^{\bullet}$ (Figure 1.15).[132] This complex was formed through the reaction of a Ni^{II} precursor with *m*CPBA. Observation of *meta*-chlorobenzoic acid as the reaction product suggests that O-O bond scission, after coordination of *m*CPBA, is heterolytic. This would result in the formation of a Ni-oxygen adduct. X-ray absorption near edge spectroscopy (XANES) suggests that this EPR silent adduct is best assigned as Ni^{III} while EXAFS supports the assignment as a Ni^{III}–$O^{\bullet}$, with antiferromagnetic coupling of the d^7 centre with the oxyl radical accounting for the EPR silence. Importantly, resonance Raman spectroscopy suggests the presence of a Ni-O bond. Ni^{III}–$O^{\bullet}$ was shown to be able to oxidise alkenes, sulphides and C-H bonds (xanthene, DHA and fluorene).

The above discussion highlights the fact that metal-oxygen adducts of the type M-O(X) (where M=Ni,Cu, X= H, OCO_2H) are reactive towards hydrocarbons, despite the fact that the oxygen atom is involved in a covalent bond with another non-metal atom therefore is not a true terminal-oxo. This is particularly true in the case of Tolmans [Cu^{III}–OH], where the rates of oxidation are comparable to previously reported terminal oxos. This suggests that should late transition metal-oxos be isolable, one would expect them to be exceptionally potent oxidants. Therefore, late first-row transition metal oxos are key synthetic targets in this field of study.

1.6.4 Copper Model Complexes

Fully characterised, stable, terminal copper-oxos are absent from the literature. Despite this, several model systems have provided a glimpse at the oxidising power of terminal copper-oxos. Of particular note is the zeolite Cu-ZSM-5 which has been shown to contain a well-defined copper active site and is capable of selectively oxidising methane to methanol.[134] Vibrational spectroscopy was extensively used to identify the active species as a [Cu-O-Cu] core.[135] DFT calculations have ascribed this remarkable reactivity to two factors. The first is that the [Cu-O-Cu] core is polarised towards a highly reactive $Cu^{+}O^{\bullet-}$ (*i.e.* an oxyl species). The second is that a strong O-H bond (90 kcal mol$^{(}$-1)) is formed in the [Cu-OH-Cu] intermediate generated after HAA, providing a strong driving force for the reaction (*vide infra*).[136]

These results give a tantalising glimpse into what could potentially be achieved using late transition metal based oxidants. In particular, they suggest that terminal copper-oxos are exceptionally potent oxidants. Therefore in order to methodically probe the reactivity of these species it is imperative that systems are developed which allow for their isolation.

1.6.5 Late Transition Metal Imido Complexes

A number of low coordinate late transition metal imido complexes have been reported in the literature. These complexes warrant special consideration as they are valence isoelectronic to a metal-oxo. That is to say that the same orbitals involved in forming M=O multiple bonds are also involved in forming M=N-R bonds. Quantitatively, the splitting of the *d*-orbitals affected by an oxo is expected to be the same as an imido.[109] Therefore the same criteria for stability discussed above applies. Notably, Co^{III},[137–144] Co^{IV},[145,146] Ni^{II},[147–150] and Cu^{III}

imidos have all been prepared utilising low-coordinate ligands. Importantly, structural analysis shows that the tetrahedral, d^6, Co^{I}II-imidos maintain a metal-nitrogen multiple bond despite the fact the antibonding d_{z^2} orbital is fully occupied. This illustrates practically that the d_{z^2} orbital can be considered non-bonding. Furthermore, Ni^{II} and Cu^{III} imidos both feature the d^8 electron count expected for a Cu^{III} oxo. This clearly illustrates that high *d*-electron count systems can be stabilised should an appropriate ligand system be identified.

1.7 Tridentate Ligands

As the above discussion in sections 1.5 and 1.6 discuss, we hypothesise that late transition metal-oxos will be stabilised in a tetrahedral coordination environment with a coordination sphere containing strong σ-donor atoms. As such, we surveyed the literature to assess appropriate ligand candidates. From the outset, this survey was limited to N-donor ligands, and alternatives such as phosphines and alkoxides were ruled out. N-donor sets have important advantages over these systems. Firstly, they are oxidatively robust and would not be oxidised should a metal-oxo be generated in close proximity. This is in stark contrast to phosphines, which are readily oxidised, hence their use as a substrate to assess oxidative reactivity (*vide supra*). Secondly, they are synthetically more versatile and can be readily derivitised to tune steric bulk or electronic properties, unlike alkoxides for example. The use of N-donor ligands has a phenomenal precedence in the biomimetic field, as is clear to see from the above discussion, because of these properties.

1.7.1 Triaza- Macrocycles

As the TMC framework has been remarkably successful in stabilising an array of metal-oxo species,[80] a logical starting point was tridentate analogues, such as 1,4,7-triazacyclononane (TACN) or 1,5,9-triazacyclododecane (TACDD). Studies detailing the coordination chemistry of TACN are numerous. This highly basic family of ligands forms extremely kinetically stable complexes owing to the mesocyclic nature of the ligand. Within the biomimetic field, the Tolman group showed that while 1:1 ligand to metal complexes could be synthesised using various alkylated derivatives of TACN, oxo-bridged dimers were quick to form upon reaction with O_2.[153] This is due to the fact that the metal sits

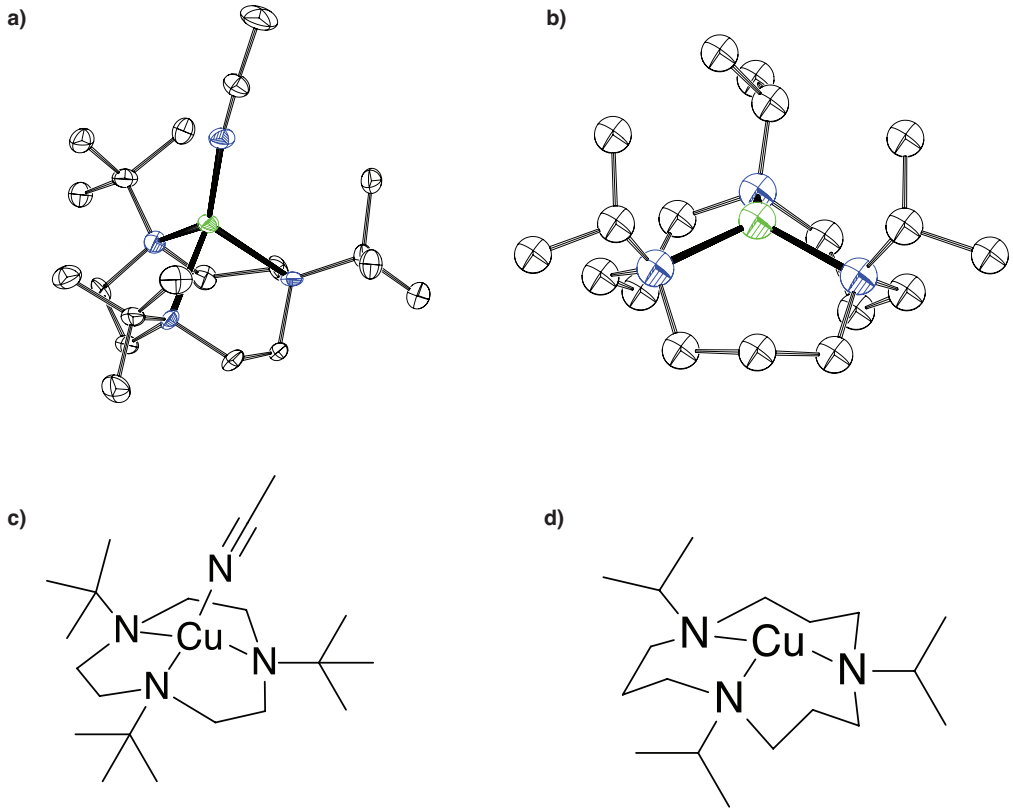

Figure 1.16: Representative crystal structures of Cu^{I} complexes of TACN (a)[151] and TACDD (b).[152] Ellipsoids are shown at 50% and counter ions have been omitted for clarity. c) and d) show the chemdraw representations of a) and b) respectively.

out of the NNN plane, therefore the putative oxo intermediate is not sterically protected and free to react. Recently, the Scarborough group have reported the introduction of *t*-butyl and adamantane substituted TACN and the related complexes.[151] Once again, while these ligands can form 1:1 complexes on binding a metal, 2:1 di-copper peroxo species on exposure to O_2.[154] This clearly demonstrates that TACN derived ligands are unsuitable for our purpose as they form 2:1 complexes upon oxidation, regardless of the bulk of the *N*-alkyl substituent. One potential strategy to combat this is to expand the ring size. This allows for the metal to sit closer to the NNN plane, as is the case in TACDD derived ligands. The Tolman group has exemplified this through synthesising a 10 and 12 membered triazamacrocycles. Although the 10 membered ligands gave similar results to TACN complexes, an interesting result was obtained

in the case of the Cu^{I} TACDD complex. The Cu^{I} centre was found to be in a 3-coordinate, pyramidal geometry, compared to distorted tetrahedral found for the Cu^{I} complex of TACN.[152] The lack of reactivity of this complex with O_2 was attributed to the high redox potential of the Cu^{I} centre due to the fact that the pyramidal coordination geometry greatly favours Cu^{I} over Cu^{II}. This highlighted the fact that the metal centre must still be accessible or else reactivity may be lost altogether. The only other structure in the Cambridge structural database of TACDD is that of a tetrahedral Zn^{II}-OH complex. Encouragingly, in this instance the zinc centre was found to be in a tetrahedral coordination environment, with the supporting ligand being identified as a particularly good σ-donor.[155]

1.7.2 Diazacyclooctane and Derivatives

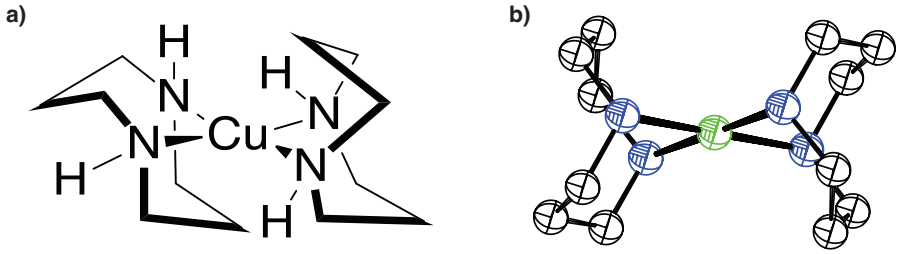

Figure 1.17: a) Chemdraw representation of a $[Cu(daco)_2]^{2+}$ complex. b) Representative crystal structure of a Cu^{II} DACO complex.[156] Ellipsoids are shown at the 50% probability level, counter ions are omitted for clarity.

After considering the above reports, we were convinced that pursuing a meso-/macrocyclic framework would provide a kinetically robust ligand platform for the synthesis of late-transition metal-oxos. This was further enforced by studies on a mesocyclic, tetrahedral Cu^{I} complex by the Itoh group, which formed an isolable end-on superoxo on reaction with O_2.[157–160] To date, this system has not been able to stabilise a metal-oxo species, most likely due to the metal-binding pocket being relatively exposed and the ligand framework

susceptible to oxidation. The supporting ligand in this work was derived from the diazamesocycle 1,5-diazacyclooctane (DACO).

DACO possesses several properties which make it an excellent ligand.[161] Firstly, The nitrogen atoms in these systems are particularly strong σ-donors, owing to the high directionality of the lone pairs. Secondly, the formation of two six-membered chelate rings upon coordination giving rise to kinetically stable complexes. The unique coordination chemistry of DACO has been well studied.[161] Reaction of Ni^{II} and Cu^{II} salts with DACO has been shown to generate the corresponding, square planar complexes of the general formula $[M(DACO)_2]^{2+}$.[156,162] In contrast, $[Co^{III}(Cl)(DACO)_2]^{2+}$ displayed a 5-coordinate square pyramidal structure.[163] Analysis of the crystal structures of these complexes showed that, in all cases, both of the coordinated DACO ligands were bound to the metal with the ligand displaying a boat-chair configuration. The boat-chair configuration is defined by metal coordination that results in the formation of two six membered chelate rings (containing the metal atom, the two donor atoms and one of the propylene linkers, Figure 1.18). One of these rings adopts a boat configuration while the other adopts a chair configuration. Importantly, this means that the methylene groups at the three and/or seven positions are ideally located to prevent the coordination of ligands along the z-axis. Consequently, DACO is ideally suited to forming low coordinate complexes.

The DACO framework is also readily functionalised. In order to introduce pendant arms containing ligating functional groups, several derivatives of DACO have been developed, almost exclusively through N-alkylation. Square pyramidal Ni^{II}, Co^{II} and Zn^{II} complexes of 1,5-diazacyclooctane-*N*,*N*-diacetic acid (DACODA) were synthesized by Legg and co-workers.[164–166] Darensbourg and co-workers synthesized bis-mercaptoethyl, (2-mercaptoethyl)-1,5-diazacyclooactane (bme-DACO).[167–169] Unusually, this square planar

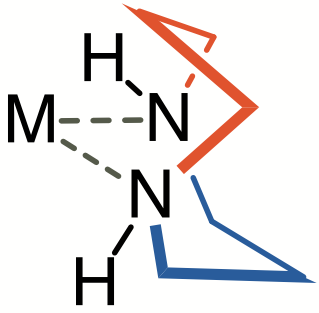

Figure 1.18: The Boat Chair Conformation of 1,5-diazacyclooctane. An Illustration of the boat fragment is shown in red while the chair fragment is shown in blue.

N_2S_2 coordination environment places the 1,5-DACO ring in a boat-boat conformation. Alkylation of the S-donor atoms with methyl iodide results in the formation of the usual boat-chair conformation. Halfen and co-workers have reported Fe- and Mn- complexes of the N,N-pyridyl-substituted derivative *N,N*-bis(2-pyridyl)-1,5-diazacycloactane ($DACOpy_2$).[170–172] A mono-N-pyridyl, tridentate analogue was also developed by the same group with the capability to form mono- and bi- nuclear Cu^{II} complexes.[173] Crucially, these complexes demonstrate that DACO can be readily *N*-functionalised and importantly, this generally has little effect on the coordination conformation of the ligand *i.e.* coordination along the z-axis is still restricted and the formation of low-coordinate complexes is preferred.

1.7.3 1,1,1-Tris(aminomethyl)ethane and Derivatives

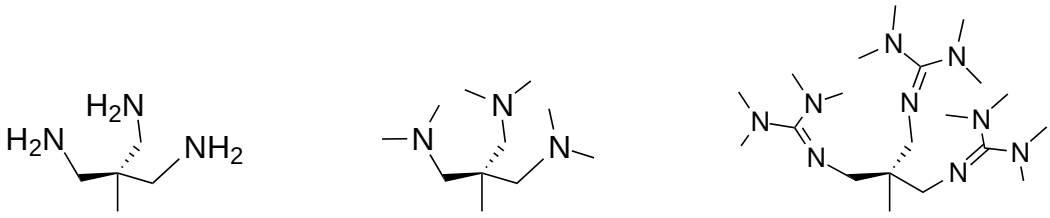

TAME **Me_6TAME** **guanTAME**

Figure 1.19: Chemdraw representations of TAME, Me_6TAME and guanTAME.

As is the case with Itoh's Cu^{I} complex described above, *N*-functionalisation of DACO fails to produce complexes with sufficient steric bulk or oxidative robustness to stabilise highly oxidising intermediates. Without *N*-alkylation, 2:1 complexes are formed. Notwithstanding, the DACO framework is a highly desirable moiety to incorporate into our ligand design. Therefore we decided to explore the possibility of functionalising this framework at the three (or seven) position. To this end, a simple scifinder search for tripoal triamines pointed us in the direction of 1,1,1-tris(aminomethyl)ethane (TAME).

The coordination chemistry of TAME (Figure 1.19) and its derivatives has been extensively studied. Due to the lack of steric bulk in this ligand, 2:1 complexes are often formed. Increasing the steric bulk via alkylation of the amine donors in TAME to give 1,1,1-tris(*N*,*N*-dimethylamino)methylethane (Me_6TAME) (Figure 1.19) resulted in the ligand switching from binding to metals in a tripodal tridentate fashion, to a bidentate binding mode, with one of the ligands remaining unbound.[174] Similarly, the more bulky guanidine derivative of TAME, 1,1,1-tris(2*N*- 1,1,3,3-tetramethylguanidino) methylethane (guanTAME) (Figure 1.19) has been shown to exhibit variable denticity. While Chang and co-workers have isolated the pseudo-tetrahedral complex [Co(guanTAME)Cl](OTf) (OTf = trifuoromethanesulfonate) where guanTAME binds as a tripodal facially capping ligand,[175] Wittmann and co-workers have reported a bidentate binding mode for guanTAME in both [Mn(guanTAME)$(Cl)_2$] and both [Zn(guanTAME)$(Cl)_2$], with the remaining ligand arm unbound in both cases.[176] This variable denticity of TAME and guanTAME is highly undesirable and, we believe, is a factor which needs to be addressed before such ligands will achieve a consistent denticity.

1.8 Conclusions

Developing the ability to selectively bring about the facile oxidation of aliphatic hydrocarbons is one of the grand challenges facing chemists. Reactions of this type would be of phenomenal environmental and economic importance as it would provide new avenues to important chemical feedstocks as well as allow for the more efficient utilisation of natural feedstocks such as methane.

Studies on a plethora of enzymatic systems have shown that nature can achieve the selective functionalisation of hydrocarbons under ambient conditions, most notably the methane monooxygenase (MMO) family of enzymes is capable of oxidising the incredibly strong bond in methane to form methanol. Furthermore, it is increasingly apparent that metal-oxos are the reactive intermediates responsible for this functionalisation. A growing number of biomimetic catalytic systems have been developed that can oxidise C-H bonds with predictable reactivity and selectivity. However they are currently limited by the strength of the bonds which they can activate. In order to further our understanding of these natural and synthetic catalytic systems, a library of metal-oxo model complexes have been developed. These complexes have been shown to oxidise strong C-H bonds such as those in cyclohexane but to date have not been able to activate the strongest of C-H bonds such as those in methane. In general, these complexes are supported by polyamine or polypyridyl ligands, with the metal centres in tetragonal symmetry. A direct consequence of this is the problem which has been dubbed the oxo-wall for tetragonal symmetry. Using ligand field theory this concept predicts that in tetragonal symmetry, metal-oxos with a *d*-electron count greater than 4 (or 5 in high spin systems) will be unstable. This idea is used to explain the absence of late transition metal-oxos containing Co, Ni or Cu; as these metals possess unstable *d*-electron configurations, even in high oxidation states.

Late transition metal-oxos are of great interest to us as we believe that they will be incredibly potent oxidants. This is based on Mayers theory that the thermodynamic driving force is strongly correlated to the strength of the O-H bond formed after HAA by the metal-oxo in these reactions. This determines the strength of the C-H bond which can be oxidised. We would expect the O-H bonds formed by late transition-metal oxos to be particularly strong as the metal centres are highly oxidising and the reduced M-OH products are less acidic. Therefore these species should be capable of oxidising the strongest of C-H bonds. The strong oxidising ability of late transition metal oxygen adducts has already been hinted at through a variety of Ni and Cu model complexes. Furthermore, the strategy we propose to employ to stabilise these species, the enforcement of a *pseudo*-tetrahedral ligand field, has already been demonstrated to stabilise the valence isoelectronic metal-imido species.

1.9 Aims

The aim of this project was to investigate the factors that effect the reactivity of late transition metal-oxo species. By identifying the relevant structure/function relationships, we envisioned being able to guide the design of the next generation of hydrocarbon oxidation catalysts towards the activation of stronger C-H bonds. In pursuit of this goal, we identified late transition metal-oxos as our key synthetic targets. We then sought to identify a ligand framework which would allow us to stabilise these late transition metal-oxo species. This ligand must be tripodal, tridentate and oxidatively robust. Additionally, the ligand should possess strong σ-donor atoms. Consequently, we have identified aliphatic, alkyl amine species as ideal targets. After surveying the literature, we were unsatisfied that existing ligands that meet this criteria would be sufficient for our needs. Therefore, we set ourselves the challenge of synthesising a ligand which would stabilise late transition metal-oxo species (Figure 2.1, **1**). This compromised the key short term goals of our project, which forms the basis of this thesis. We have designed the ligand framework **1** which we believe meets all the necessary criteria we have outlined within this introduction. Furthermore, we have incorporated a mesocyclic structural motif which we believe will overcome the issues traditionally associated with tridentate ligands.

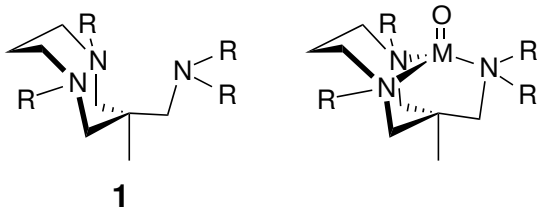

Figure 1.20: Left) A chemdraw representation of the target ligand **1**. Right) A generic tetrahedral metal-oxo.

The aims of this project can be summarised as follows:

- To pursue versatile synthetic routes towards the synthesis of the target ligand framework, **1**.
- To explore the coordination chemistry of the ligands developed with late first row transition metals.
- To optimise the design of the ligand based on our coordination chemistry investigations.

We aimed to scout synthetic routes to four target molecules (Figure 1.21), which are derivatives of **1**. Synthesis of **2** and the subsequent investigation of its coordination chemistry gave an indication of the effect of the DACO ring on the coordination behaviour of this system. This allowed us to compare **2** against TAME and therefore, evaluate our ligand design. We also aimed to alkylate **2** to give **3** and **4**. This increased the steric bulk associated with the ligand framework (**1**) whilst also increasing the σ-donor strength of the ligand. Finally,

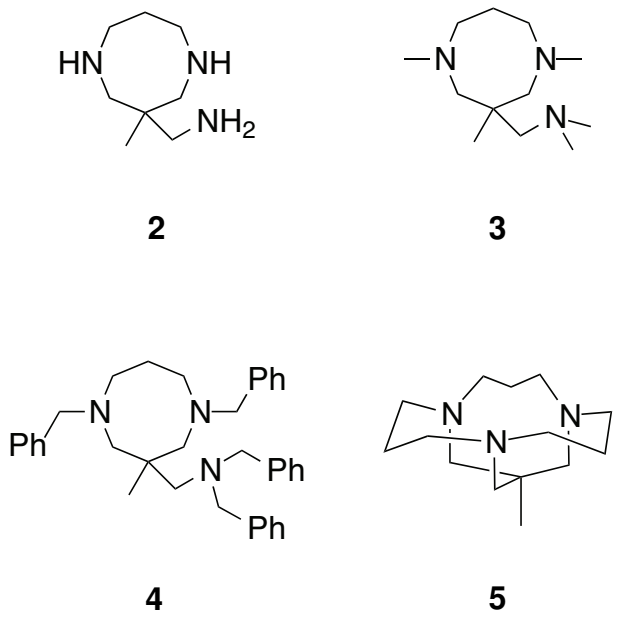

Figure 1.21: Chemdraw representations of the key synthetic targets of this thesis.

we aimed to isolate the tricyclic macrocycle **5** which we anticipated would act as an excellent chelating ligand. By isolating these target ligands, we aimed to study their coordination chemistry with first row transition metals in order to determine the structural factors that dictate complex formation. This will guide us in our overall goal of isolating a late transition metal-oxo.

Chapter 2

Synthesis and Characterisation of a Mesocyclic Tripodal Triamine Ligand

Publications resulting from work in this Chapter: Andrew D. Ure, Isabel Abnades Lzaro, Michelle Cotter, Aidan R. McDonald, *Org. Biomol. Chem.*, **2016**, 14, 483-494

2.1 Introduction

It has been postulated that late transition metal-oxos would be stabilised in a *pseudo*-tetrahedral ligand field and therefore, we have set ourselves the goal of synthesising a ligand capable of stabilising such a species. We have outlined several criteria which this ligand should meet. First of all, the ligand must be tripodal and facially capping, so as to enforce a *pseudo*-tetrahedral coordination environment. Secondly, the ligand must contain strong σ-donors in order to stabilise the anticipated high oxidation states at transition metal-oxo centres. Furthermore, it is crucial that the donor atoms as well as the ligand skeleton are oxidatively robust, so as to maintain the structural integrity of the desired designed complex in what would potentially be a highly oxidising environment. For this reason, we focused our attention on tertiary amine donor atoms.

Meso- and macrocyclic, peralkylated amine ligands have been used to great success in stabilizing early transition metal-oxo complexes (metal = Mn, Fe),[80,177–181] and late transition metal-superoxide and -peroxide complexes.[157–160,182–186] Meso- and macrocyclic frameworks add further stability to complexes bearing these ligands, because of the macrocyclic effect.[187] Based on these considerations, we set out to prepare mesocyclic **1** (Figure 2.1), which meets all of the above criteria. **1** can be considered as a hybrid of the triamine 1,1,1-tris(aminomethyl)ethane (TAME) and 1,5-diazacyclooctane (DACO) frameworks. We postulate that the mesocyclic nature of **1** and the steric bulk around the putative metal-binding site will ensure **1** would bind in a tridentate fashion yielding 1:1 complexes. Furthermore, we envisioned that

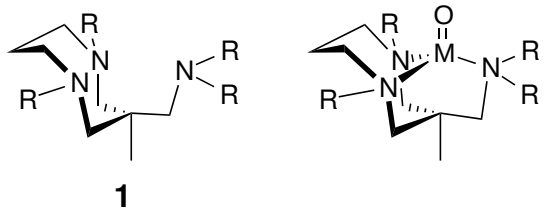

Figure 2.1: Left) The target ligand framework for this thesis. **1** is tripodal, tridentate and contains strong σ-donor atoms. R = H, alkyl group. Right) A generic tetrahedral metal-oxo complex which is the ultimate synthetic target of this work.

introducing a third donor atom to DACO at the 3-position of the DACO ring, rather than through *N*-alkylation, would present several benefits. Firstly, introduction of ligating functionalities at the 3-position would ensure a facially capping ligand (and a *pseudo*-tetrahedral complex), whereas *N*-alkylated derivatives of DACO are mainly meridional binders. Secondly, organic functionalities can be readily introduced through *N*-alkylation in **1**, allowing us to readily modulate the electronic and steric properties of the triamine **1**.

2.2 Synthesis of 1,5-Diazacyclooctane Derivatives

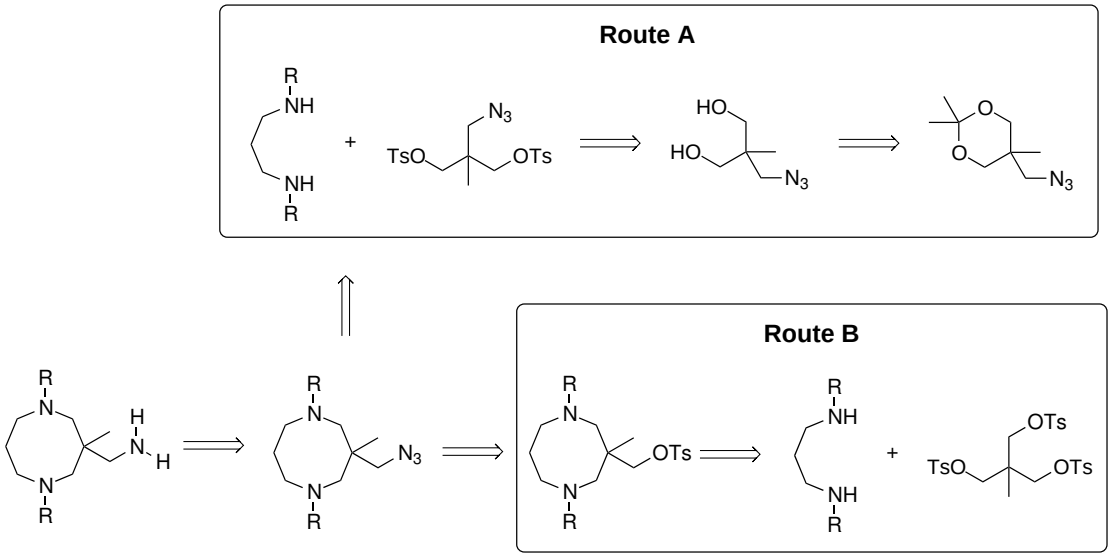

Figure 2.2: Retrosynthetic anaylsis of target ligand framework, **1**. Route A shows how the *exo*-cyclic arm of **1** may be independently addressed. Route B shows how initial formation of the 1,5-diazacyclooctane ring could be followed by *exo*-cyclic functionalisation. R = *p*-tolylsulphonyl

Reterosynthetic analysis of our target ligand framework identified two possible routes to the synthesis (Figure 2.2). In the first of these, route A, (Figure 2.2) we envisioned first selectively addressing the *exo*-cyclic arm of the ligand before forming the 1,5-diazamesocyclic ring. In the second of these, route B, (Figure 2.2) we envisioned first forming the 1,5-diazamesocyclic ring fragment before functionalising the remaining free *exo*-cyclic arm to give our target. We reasoned that route A would ultimately allow us greater control over the functionalisation of our ligand, because the cyclic and *exo*-cyclic amine moieties could be addressed independently. Furthermore, we believed that this route would minimise the possibility of oligimer formation during the cyclisation step. Therefore, we pursued route A first.

2.2.1 Route A - Synthesis of 1,5-Diazacyclooctane Derivatives *via* initial diol protection

We identified the commercially available triol, **6**, as the ideal starting material as it contains the required neopentyl backbone as well as reactive functional groups. We first attempted to protect two of the three hydroxyl groups, in order to leave the third free to react. **6** was readily converted into the 1,3-dioxane, **7**, through reaction with acetone in the presence of a catalytic amount of tosylic acid to give the desired 1,3-dioxane protected product, **7**, in a 92% yield (Scheme 2.1). ^{1}H NMR confirmed the formation of **7**, in accordance with the previously reported spectral data.[188] The 1,3-dioxane, **7**, was then reacted with tosyl chloride in pyridine to give the corresponding tosylated 1,3-dioxane (80%), **8**, utilising the procedure reported by Gash (Scheme 2.1).[189] The ^{1}H NMR spectrum of **8** was found to match that reported by Nobuyasu.[190] The corresponding azide, **9**, was then generated by nucleophilic substitution of the tosyl group in **8** using sodium azide according to the procedure reported by Liu (Scheme 2.1).[191] With **9** in hand, we were faced with two possibilities.

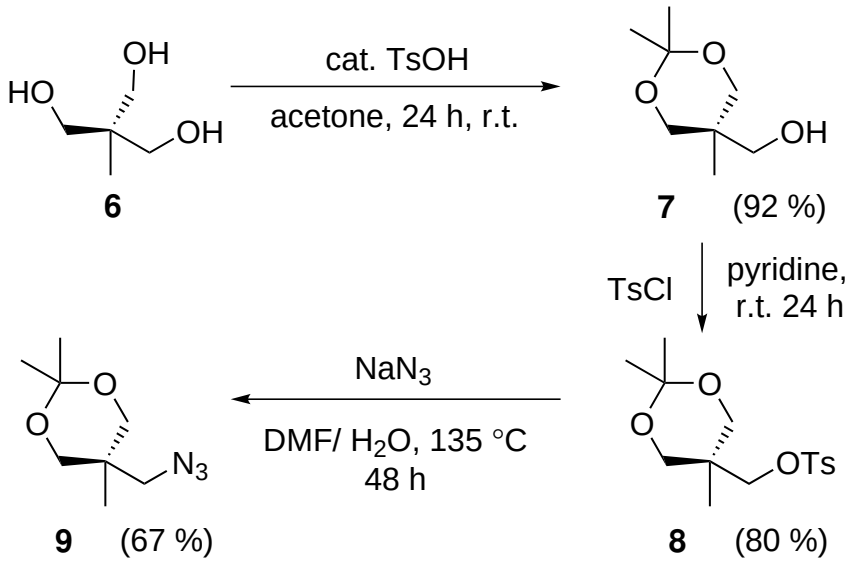

Scheme 2.1: Synthesis of 1,3-dioxane protected azide **9**. Two of the hydroxyl groupls in **6** were protected as a 1,3-dioxane (**7**). The remaining hydroxyl group was activated to give the tosylated species **8**, which could then be substituted with an azide group to give **9**.

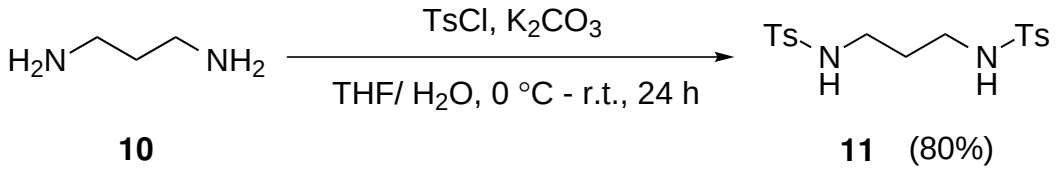

Scheme 2.2: Synthesis of activated diamine **11** *via* the procedure reported by Halfen.[172] **11** is a requisite synthon of the Richman-Atkins cyclisation.[192]

The first of these was to utilise the azide moiety in **9** as a masked amine and proceed with the Richman-Atkins cyclisation, in which a activated diol is reacted with a *bis*-tosylamide.[192] We first synthesised the requisite synthon to form the DACO ring. 1,3-diaminopropane (**10**) was reacted with tosyl chloride in the presence of K_2CO_3 (Scheme 2.2) to give the activated diamine, **11**, according to the procedure reported by Halfen.[172] The resulting white crystals were ground to a fine powder using a pestle and mortar and dried overnight under high vacuum in order to remove any residual water.

We then turned our attention to removing the 1,3-dioxane protecting group in **9**. **9** was dissolved in tetrahydrofuran (THF) with several drops of concentrated hydrochloric

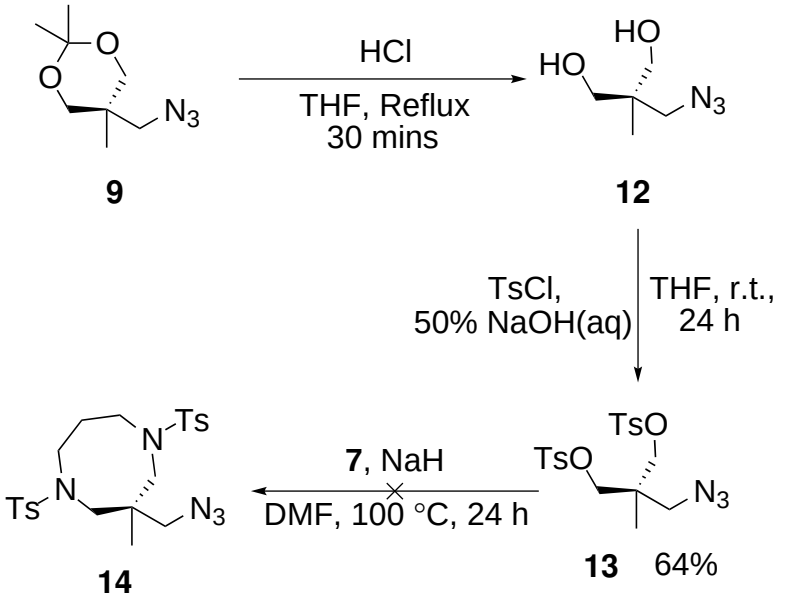

Scheme 2.3: Synthesis of *bis*-tosylazide **13**. The 1,3-dioxane protecting group in **9** was cleaved to give the diol **12** which could then be activated for cyclisation through reaction with tosyl chloride to give **13**. The attempted cyclisation of **13** with **11** was unsuccessful due to the instability of **13** under the harsh reaction conditions.

acid and refluxed for 30 minutes to generate the diol, **12** (Scheme 2.3).[191] The crude diol, **12**, was then activated without isolation through reaction with tosyl chloride and sodium hydroxide in THF to give the *bis*-tosylate, **13**. ^{1}H NMR of **13** showed no evidence for the two diastereotopic 3H methyl peaks associated with the dioxane in **12**. Furthermore, the appearance of aromatic peaks associated with the newly installed tosyl groups, confirmed the formation of **13** (Scheme 2.3).

In order to perform the Richman-Atkins cyclisation step, the activated *bis*-tosylamide, **11**, was dissolved in anhydrous *N,N*-dimethylformamide (DMF) and reacted with two equivalents of sodium hydride in order to generate the corresponding di-sodium salt *in situ* (Scheme 2.3). A solution of *bis*-tosylate, **13**, in anhydrous DMF was then added dropwise and the reaction heated at 100 °C for 24 hours. Analysis of the product by electrospray ionisation mass spectrometry (ESI-MS) showed no evidence for formation of the desired cyclised product, **14**. Similarly, ^{1}H nuclear magnetic resonance (NMR) spectrum showed the presence of a significant amount of unreacted activated diamine, **11**. We attributed this to the organic azide being unstable due to decomposition under the harsh reaction conditions. Additionally, it is possible that adventitious water may have been present in the *bis*-tosylazide as it is inadvisable to purify these compounds to complete dryness due to risk of explosion. This could have resulted in re-protonation of the sodium salt of *bis*-tosylamide, **11** and would explain the significant presence of *bis*-tosylamide, **11** post reaction.

As a consequence of this negative outcome, we revisited our retrosynthetic analysis (Figure 2.2). We concluded that rather than utilising the azide **9** as a masked amine, it would be more pertinent to first reduce the azide before attempting to form the ring; as one would expect the amine functionality to be more stable to decomposition than the azide. To this end, rather than cleaving the dioxane group in **9**, we first reduced the azide moiety. This was achieved using 5% w.t. Pd/C and ammonium formate in methanol to give the primary amine **15** in a 50% yield. The amine, **15** was characterised using ^{1}H NMR spectroscopy which showed a broad 2H singlet at 0.99 ppm assigned, using heteronuclear single quantum coherence (HSQC) NMR spectroscopy spectroscopy, to the newly introduced NH_2 moiety. Furthermore, ESI-MS

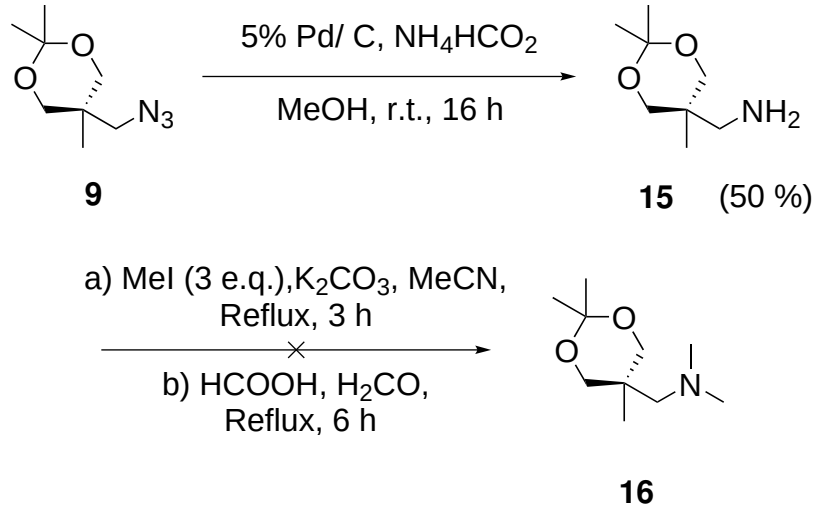

Scheme 2.4: Synthesis of amine **11**. The azide functionality in **9** was readily reduced to the primary amine in **15**. Our attempts to methylate led to either over alkylation (MeI) or decomposition of **15** (HCOOH, H_2CO).

showed a single mass peak at m/z = 160.1342 for $C_8H_{18}NO_2$ (expected m/z = 160.1338), corresponding to the desired product, **15**. We then attempted to methylate the amine, **15** to give the dimethyl species, **16**. We first attempted this by reacting the amine **15** with three equivalents of iodomethane (Scheme 2.4). However, ESI-MS analysis of the reaction product showed a distribution of all the possible methylation products. Peaks for the primary, secondary, tertiary and quaternary amines were all observed. While we had expected this to a certain extent, we had envisioned that by carefully controlling the reaction stoichiometry that we would be able to drive the reaction in the direction of the desired tertiary product, **16**, which we could isolate by column chromatography. Unfortunately, this proved not to be the case and the products in this mixture were inseparable. We therefore turned our attention to a more selective method of alkylation, the Eschweiler-Clarke methylation. As this reaction proceeds *via* an iminium cation intermediate, over alkylation to the quaternary product is not possible therefore, this reaction should generate only the desired tertiary product. As such, **15** was refluxed for 6 hours in the presence of excess formic acid and formaldehyde. Disappointingly, after work up, the ^{1}H NMR spectrum showed the disappearance of the two characteristic dioxane methyl peaks at 1.41 and 1.45 ppm, indicating that the dioxane protecting group had been cleaved under these reaction conditions, giving no

indication of formation of the desired product, **15**. While dioxane protecting groups are usually stable to weak acids, we believe the harsh reaction conditions employed here may have decreased the groups stability. Given these unexpected setbacks, we decided to focus our attention on route B, identified by our retrosynthetic analysis (Figure 2.2).

2.2.2 Route B - Synthesis of 1,5-Diazacyclooctane Derivatives *via* the Richman-Atkins Cyclisation

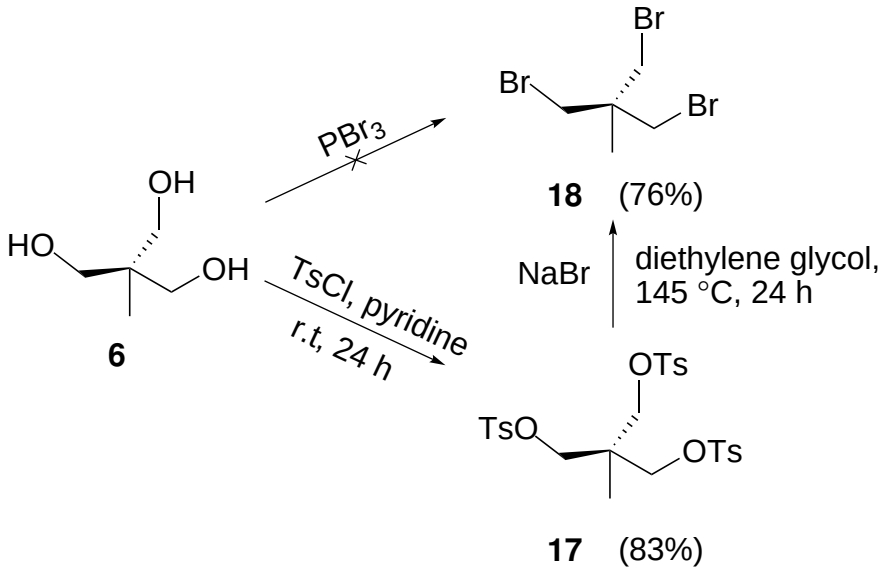

Scheme 2.5: Synthesis of activated triols **17** and **18** required for the Richman-Atkins cyclisation. The conversion of **6** directly to the *tris*-bromide **18** was not amenable to scale up. Tosylation of **6** gave the *tris*-tosylate **17** which could either be cyclised directly or cleanly converted to the *tris*-bromide **18**.

Due to the lack of success in synthesising our target *via* route A, we decided that rather than selectively addressing one arm of the triol, **6** (Scheme 2.5), we would instead attempt to first cyclise its activated derivatives, *tris*-tosylate **17** and *tris*-bromide, **18** (Scheme 2.5). Triol **6** was first activated through reaction with four equivalents of tosyl chloride in pyridine (Scheme 2.5) to give the *tris*-tosylate, **17**, in 83% yield. While **17** can be isolated simply by precipitation with ice-water, we found that the work-up reported by Lindhorst and co-workers,[193] in which **17** is extracted with ethyl acetate (EtOAc) and dried over $MgSO_4$, gave a rigorously anhydrous product. This was far better suited

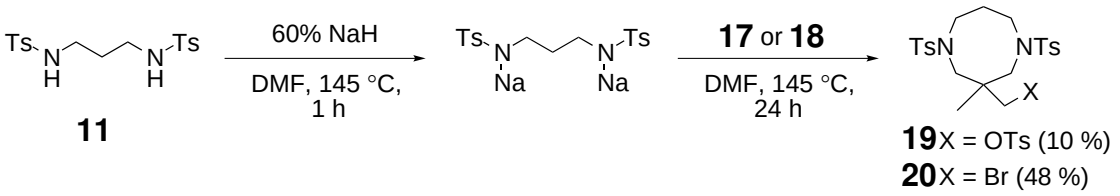

Scheme 2.6: Synthesis of diazamesocycles **19** and **20**. The disodium salt of **11** was generated *in situ* before reaction with either of the activated triols **17** or **18** to give the corresponding mesocycles **19** or **20**.

to our needs as the cyclisation reaction must be performed under strictly anhydrous conditions.

Crucially, we found that **17** could be cleanly converted to the *tris*-bromide **18** on a large scale. This was achieved through reaction of the *tris*-tosylate **17** with NaBr in diethylene glycol at 145 °C, as shown in Scheme 2.5. The synthesis of **18** has been previously reported and can be achieved through two routes. In a reaction analogous to that shown in Scheme 2.5, the benzenesulphonate analogue of **17** is reacted with NaBr under the same conditions.[194] In our hands, we found that this product required purification by distillation whereas the synthesis we developed did not. Additionally, **6** can be converted directly to **18** through reaction with PBr_3.[195] While we found this procedure useful on small scales, it was not amenable to scale up as a relatively large amount of PBr_3 was required as the reaction solvent. This meant that the two-step procedure towards **18** was our preferred route to this activated triol. Having isolated the two activated triols (**17** and **18**), we then set about forming the DACO mesocycle.

Based on the procedure outlined by Richman and Atkins,[192] we reacted the activated diamine, **11** (0.1 M, 100 mL) with two equivalents of sodium hydride in anhydrous DMF, generating the corresponding disodium salt *in situ*. Once the evolution of hydrogen gas had visibly ceased, the temperature was increased to 100 °C under argon for one hour. The activated triol (**17** or **18**) in DMF (0.2 M, 50 mL) was added dropwise. The resulting reaction mixture was heated at 145 °C under argon for a further 24 hours. These conditions yielded the desired cyclised products **19** or **20**. **19** and **20** were fully characterised using ^{1}H and ^{13}C NMR spectroscopy which were assigned in conjunction with HSQC and heteronuclear multiple-bond correlation (HMBC) spectra. Importantly,

the ^{1}H NMR spectrum displayed resonances typical of mesocyclic aliphatic protons, confirming that cyclisation had occurred. Furthermore, the ESI-MS showed single mass peaks corresponding to [M+H] in both instances. Additionally, single crystals of **20** were grown by slow evaporation of a solution of **20** in chloroform ($CHCl_3$) (Figure 2.4b). **20** was found to crystallise in the $P2_1/c$ space group. The data revealed that **20** had crystallised as a 50:50 mixture of two distinct boat-chair conformations, illustrated in Figure 2.3 a and b. Furthermore, the crystal structure suggested that during the crystallisation period, halide exchange between the solvent and **20** had occurred. This resulted in the formation of both bromide and chloride containing analogues of each of the two conformers. The Halide positions were modelled as 50% occupied in both conformers, split between bromide and chloride. This resulted in refined occupancies of Br1 35%, Cl1 15% and Br2 33%, Cl2 17%. This gave rise to the four discrete units shown in Figure 2.3.

Interestingly, we observed that no reaction product was formed if the reaction mixture was heated to temperatures lower than 140 °C. We attribute the fact that such harsh conditions are necessary to the typical sluggish S_N2 reactivity of the neopentyl backbone.[196] This arises because bulky vicinal substituents sterically shield the carbon atom which must be attacked by the amide in order for the reaction to proceed. We also attribute the fact that the yield of the cyclisation reaction utilising the *tris*-bromide, as opposed to the *tris*-tosylate, is significantly higher to sterics. In this instance, we propose that the smaller size of the bromide groups in **18** compared to the tosyl groups in **17** reduce steric clashes in the transition state and therefore give a higher yielding reaction. This is the opposite of the trend observed by Richman and Atkins, where tosylates were found to be more reactive.[192] Interestingly, we have also discovered that the inherently poor reaction kinetics act as an effective dilution, meaning that a saturated solution of **11** could be used. This was an important discovery as it allowed for this reaction to be significantly scaled up. We next sought to functionalise the remaining free arm.

In the first of these, we reacted the 1,5-diazamesocycle **19** with sodium azide in diethyleneglycol to give the corresponding azide **14** in a 44% yield (Scheme 2.7). The

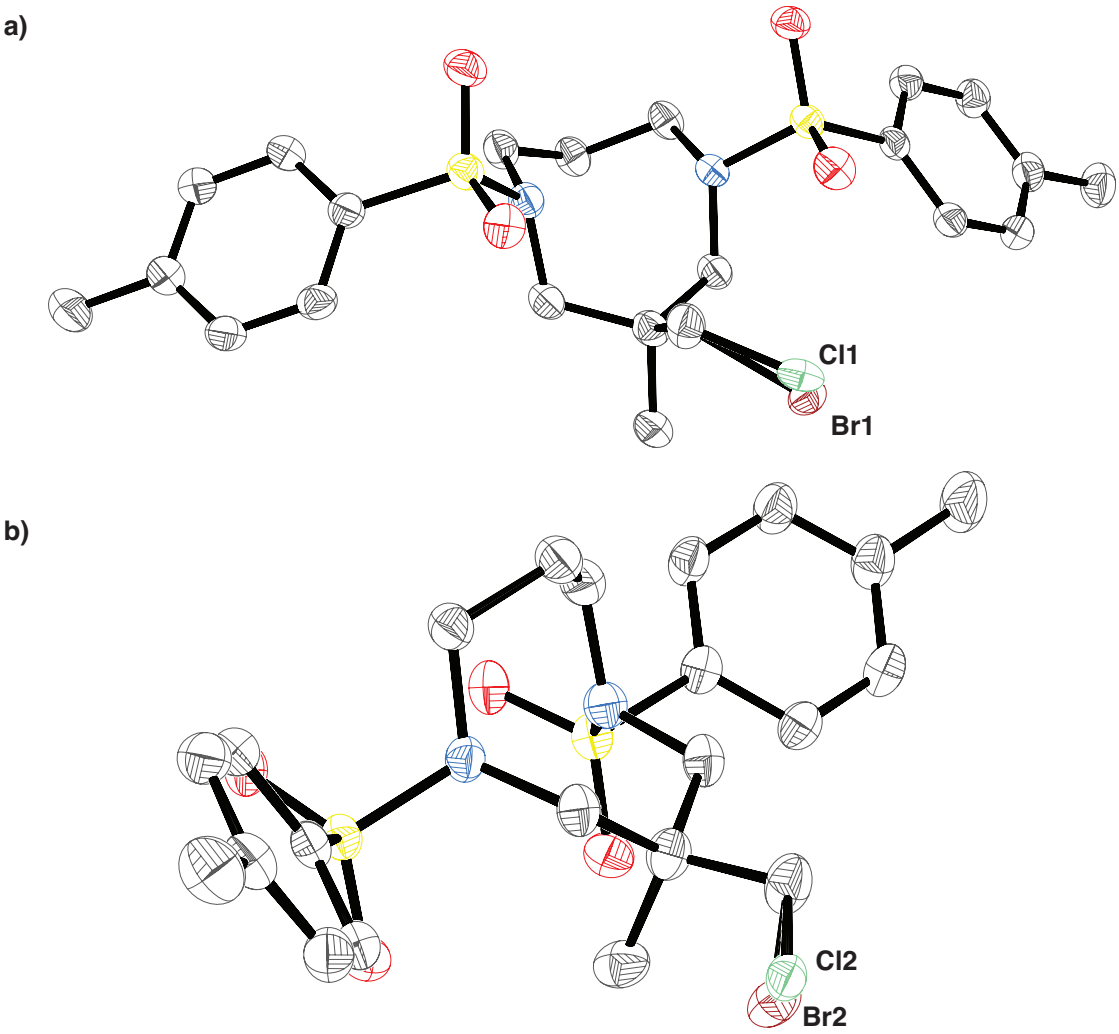

Figure 2.3: Thermal ellipsoid plot of **20**. Ellipsoids are shown at the 50% probability level. a) and b) depict the different conformers of the 1,5-DACO ring found in the unit cell.

formation of **14** was confirmed using ESI-MS and ^{1}H NMR, which showed no aromatic or methyl signals corresponding to the tosyl group in **19**. Importantly, the fourier transform infrared (FT-IR) spectrum showed the appearance of a strong vibration at 2103 cm^{-1} which we assign to a N_3 vibrational mode of the azide moiety. The azide in **14** was then reduced utilising 5% Pd/C and ammonium formate in methanol to give the primary amine **21** in a 53% yield (Scheme 2.7). Analysis of the FT-IR spectrum of **21** showed the disappearance of the band at 2103 cm^{-1}, associated with the azide, and the appearance of characteristic symmetric and asymmetric amine stretching frequencies at 3309 and 3151 cm^{-1}. This confirmed that the azide group in **14** had been reduced to the

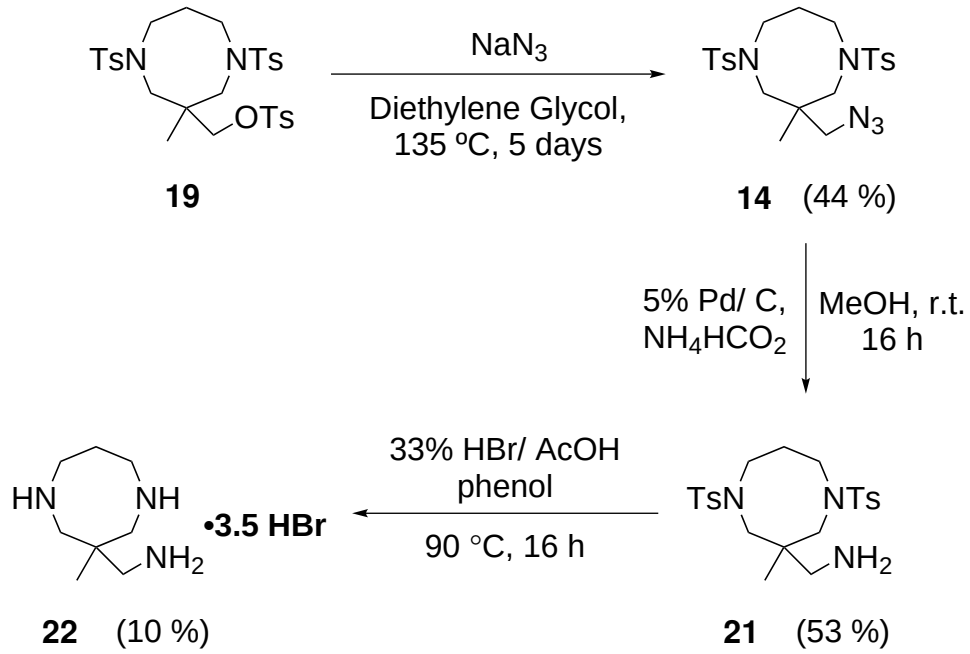

Scheme 2.7: Synthesis of 1,5-diazamesocycle **22** *via* reduction of azide **14** followed by deprotection of the *N*-tosyl groups using HBr in acetic acid.

primary amine in **21**. ^{1}H NMR and ESI-MS were also used to confirm the formation of **21**.

The *N*-tosyl protecting groups in **21** could then be removed *via* heating **21** to 90 °C in 33% HBr in acetic acid in the presence of an excess of phenol (Scheme 2.7). **22** was then isolated as the hydrogen bromide salt, **22**. The ^{1}H NMR spectrum of the mesocyclic triamine **22** showed no aromatic peaks, corresponding to the *N*-tosyl groups, indicating that they had both been successfully removed.

Unfortunately, we found the reduction of **14** poorly reproducible therefore we sought an alternative, more robust route to the HBr salt of the triamine, **22**. To this end, we

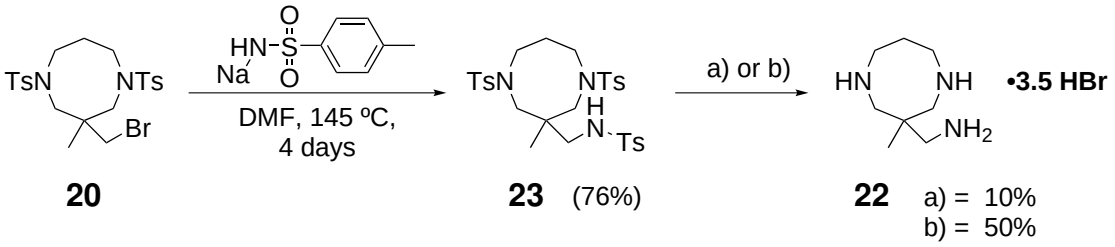

Scheme 2.8: Synthesis of 1,5-diazamesocycle **22** *via tris*-tosylamide **23**. a) 33% HBr in AcOH, Phenol, 90 °C, 16 h. b) H_2SO_4, 160 °C, 1 h.

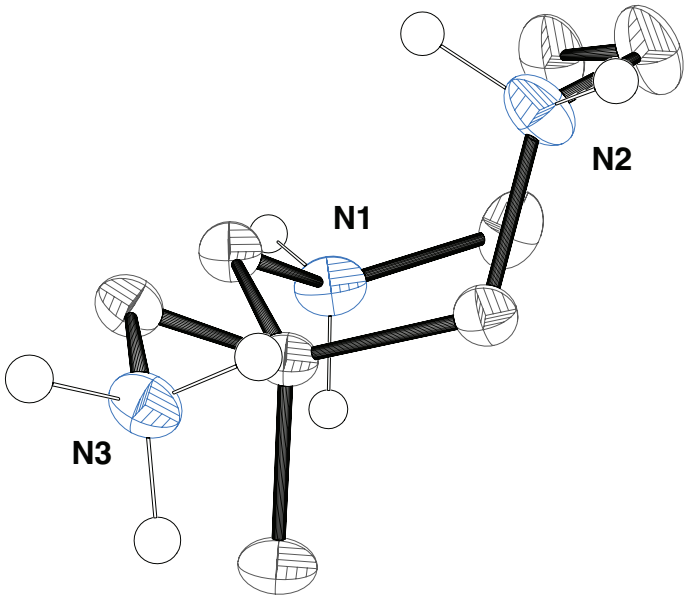

Figure 2.4: Thermal ellipsoid plot of 1,5-diazamesocycle **22**. Ellipsoids are shown at the 50% probability level. C-*H* atoms and counter ions have been omitted for clarity.

reacted the bromide **20** with sodium tosylamide at 145 °C to give **23** (Scheme 2.8). Analysis of the ^{1}H NMR spectrum of **23** showed the expected aromatic and aliphatic signals indicating the presence of the third tosylamide functionality. The identity of the assigned structure was then confirmed *via* ESI-MS, giving a peak at *m/z* = 620.1931 for $C_{29}H_{37}N_3O_6S_3$ (expected *m/z* = 620.1923). As above, the *N*-tosyl groups could be cleaved using HBr in acetic acid to give the triamine **22** in a 10% yield. In order to improve this poor yield, we investigated other routes towards *N*-tosyl deprotection. Notably, we found that heating **23** to 160 °C in concentrated H_2SO_4 to give **22** at a significantly higher yield of 50%. This corresponded to an overall yield of 20%, compared to 4% when employing HBr in acetic acid in going from **18** to **22**.

Colourless, needle like, single crystals of **22** suitable for X-ray diffraction were obtained by diffusing ethanol into an aqueous solution of **22** (Figure 2.4). **22** was found to crystallise in the R$\bar{3}$ space group (Table 2.3). The asymmetric unit was found to consist of one $[C_8H_{22}N_3]$ cation and three bromide anions. Additionally, one HBr unit was found per two $C_8H_{22}Br_3N_3$ units. Analysis of the crystal structure shown in Figure 2.4 showed that the 1,5-DACO ring in **22** was orientated in a boat-chair conformation.

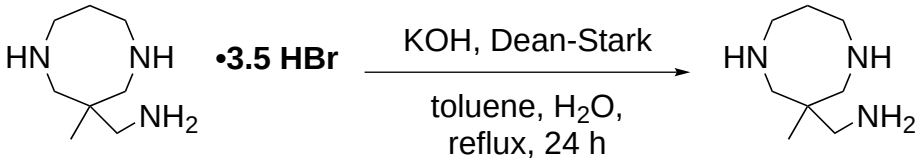

22 **2** (95%)

Scheme 2.9: Generation of freebase **22**. **22** was deprotonated in H_2O with KOH. The residual H_2O was then removed through azeotropic distillation with toluene to yield a toluene solution of **2**.

All bond lengths and angles were in good agreement with those previously reported for diprotonated DACO rings.[197] Curiously however, when compared to the other structures we have obtained (Figure 2.3) as well as those previously reported in the literature for diprotonated DACO moieties, the relative orientation of N1 and N2 would strongly disfavour complex formation. We reason that this arrangement allows for the maximum separation of the two positive charges located on the cyclic nitrogens therefore would be reasonably expected in the solid state.

In order to form *pseudo*-tetrahedral metal complexes, we require that the lone pairs of these nitrogens are on the same face of the ring so as to allow coordination to the metal centre. Therefore, we decided to probe the solution behaviour of **22** in order to better understand its conformation. In order to do this we utilised ^{1}H nuclear Overhauser effect (NOE) NMR spectroscopy, which can be used to elucidate through space coupling within a molecule. In order to carry out these studies, we first deprotonated **22**, to give the corresponding freebase **2**, (Scheme 2.9). This alleviated the repulsion between the cationic nitrogen atoms and allowed for a more accurate analysis. The ^{1}H NMR spectrum is shown in Figure 2.5a. Assignments of the observed signals were made conclusively with HSQC and HMBC NMR spectroscopy. The ^{1}H NOE spectrum arising from irradiating the multiplet at 1.72 ppm, corresponding to protons 4/4', is shown in Figure 2.5b. Importantly, this experiment demonstrated that through space coupling between protons 4/4' and all of the other protons in the molecule was present. Of particular significance is the through space coupling of 4/4' to the protons of the methyl group, 1, as well as protons 5 associated with the $-CH_2NH_2$ group. This indicated that protons 4/4' could see both faces of the mesocycle, and confirmed that **2** retained a

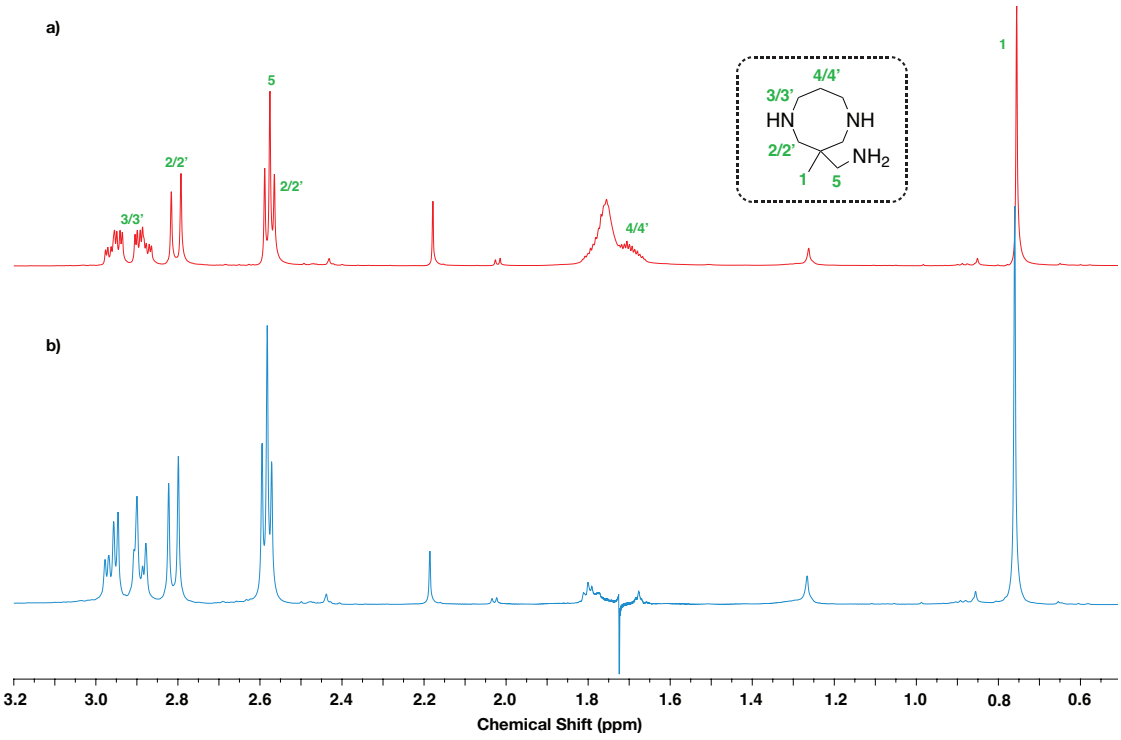

Figure 2.5: ^{1}H NMR spectra of freebase **2**. Inset shows the assignment of the resonances, made in conjunction with the corresponding HSQC spectrum. a) ^{1}H NMR spectrum of the freebase **2**. b) ^{1}H NOE NMR spectrum of **2** irradiated at 1.72 ppm.

high degree of structural flexibility in solution. Importantly, this suggested that the unfavourable conformation observed in the solid state for the protonated triamine **22** was not adopted in solution by the freebase **2** therefore would not act as a barrier to complex formation as **2** was highly flexible in solution.

2.2.3 Alkylation of the 1,5-diazamesocycle, 22

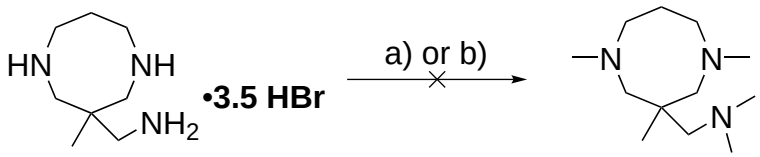

22 **3**

Scheme 2.10: Attempts at methylating cycle **22**. a) HCO_2H/ CH_2O, reflux, 8 h. b) MeI or MeOTs, K_2CO_3, MeCN, 16 h

Confident that **2** was capable of binding metals in the desired manner, we next attempted to methylate both the cyclic and *exo*-cyclic amines in **22** in order to increase the steric bulk, oxidative robustness and σ-donor strength of **22**.

To this end, we pursued several routes. We first attempted to synthesise the tetramethylamine, **3**, *via* an Eschweiler-Clarke methylation of **22**. **22** was refluxed in formic acid in the presence of an excess of formaldehyde. Analysis of the post reaction mixture using ^{1}H NMR indicated the formation of a mixture of products, none of which could be assigned as **3**. These ^{1}H NMR spectra also indicated that all of the starting material, **22** had been consumed during the reaction. We propose that rather than the reaction proceeding as depicted in Scheme 2.10, the intermediate imine which forms after the reaction of **22** with formaldehyde, reacts with an adjacent amine before it can be reduced by the formic acid. This results in the formation of aminal products, rather than the desired peralkylated product, **3**. In an attempt to prevent this intramolecular reaction, we attempted several reductive aminations using more powerful reductants. **22** was refluxed in formaldehyde in the presence of acetic acid and a reductant such as $NaBH_4$, KBH_4 or zinc powder. Unfortunately, similar ^{1}H spectra containing multiple singlets between 4 and 5 ppm, suggestive of aminal formation, were obtained in all cases. Similar reactivity has previously been observed for related complexes.[198]

We next attempted the synthesis of **3** using alkylating agents such as methyl iodide and methyl tosylate (Scheme 2.10). In this instance, we consistently obtained a majority of the over-alkylated products, with a small amount of the desired product **3**, as indicated

by the ^{1}H NMR spectrum and ESI-MS. This mixture of products was inseparable using column chromatography. At this juncture, we postponed our attempts to methylate **22** and focused our attention elsewhere.

Fortunately, we discovered that **22** reacted with benzyl bromide in the presence of excess base (K_2CO_3) to give the desired tetraalkylated product, **4** (Scheme 2.11). The formation of **4** was confirmed using ^{1}H NMR. Analysis of the spectrum of **4** showed the appearance of two new peaks at 3.64 and 3.74 ppm as well as a multiplet at 7.4 ppm. These peaks correspond to the aliphatic and aromatic protons of the benzyl groups respectively and were assigned in conjunction with HSQC and HMBC NMR spectra. The identity of **4** was confirmed by the presence of a peak at *m/z* = 518.3534 (expected *m/z* = 518.3535 for $C_{36}H_{44}N_3$). Curiously, we observed no evidence for the over alkylation of **22** in this reaction whereas in the reaction between **22** and iodomethane, we did. This is unusual as one would expect the more reactive benzyl bromide to be more reactive and therefore also form over alkylated products. We ascribed this marked difference in reactivity to the steric bulk of the benzyl groups retarding the rate of quaternisation of the amine functionalities. Importantly, this provides support to the idea that benzyl groups will form a well sterically shielded metal binding pocket.

As with **22**, we probed the solution behaviour of **4** using rotating-frame Overhauser effect spectroscopy (ROESY) experiments; which similarly to NOE are used to elucidate through space interactions (Figure 2.6).

We once again irradiated the sample at a frequency corresponding to the signal at 1.64 ppm for protons 4/4'. We observed that these protons showed through space coupling

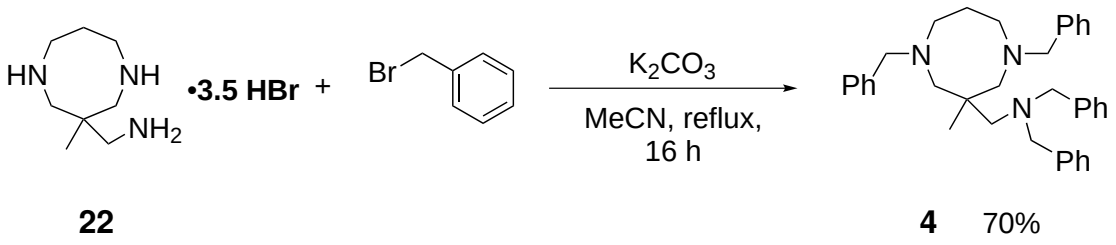

22 **4** 70%

Scheme 2.11: Benzylation of cycle **22**. Reaction of **22** with benzyl bromide lead to the clean formation of the tetraalkylated **4**.

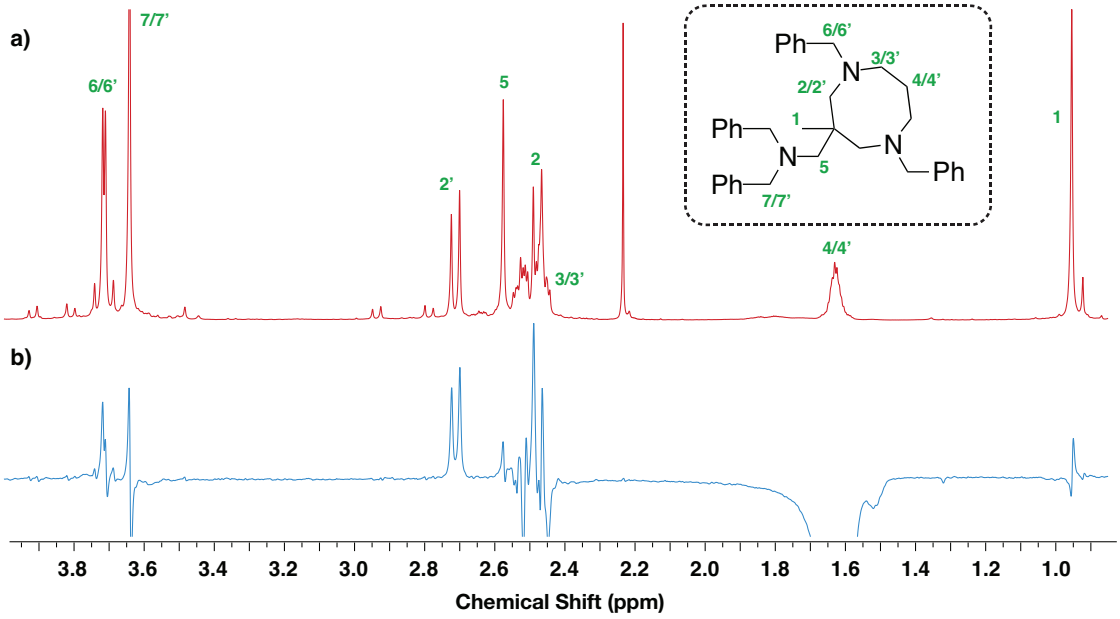

Figure 2.6: a) ^{1}H NMR spectra of **4**. Resonance assignments are shown in the inset and were made in conjunction with the corresponding HSQC spectrum. b) ^{1}H ROESY spectrum of **4** irradiated at 1.63 ppm. 600 MHz, $CDCl_3$

to all other protons within the DACO ring, the benzylic $-CH_2$ groups and, importantly, both of the *exo*-cyclic $-CH_2$ (5) and $-CH_3$ (1) groups. This strongly suggests that although we have alkylated all of the methyl groups in **22**, to give the tetrabenzylated analogue **4**, the molecule retains a high degree of structural flexibility in solution.

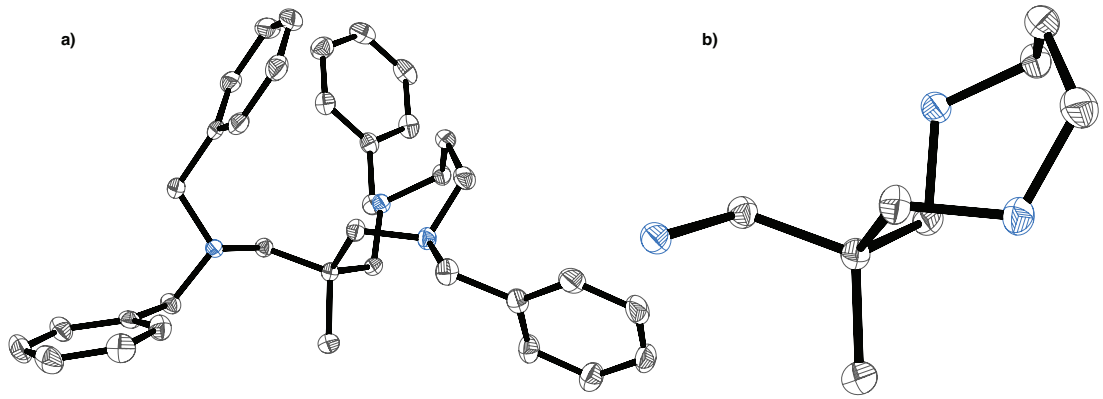

Figure 2.7: Thermal ellipsoid plot of **4**. H-atoms have been omitted for clarity. Ellipsoids are shown at the 50% probability level. a) Shows the full structure; b) Benzyl groups have been omitted in order to highlight the unusual conformation of the DACO ring.

Table 2.1: Selected bond lengths and angles.

	22	**20**	**4**	[**4**·H](PF$_6$)	[**4**·2H]((OTf)$_2$)
Mean cyclic C-C / Å	1.531	1.532	1.532	1.531	1.535
Mean C-N1 / Å	1.506	1.480	1.464	1.484	1.475
Mean C-N2 / Å	1.495	1.477	1.474	1.514	1.519
Mean C-N3 / Å	-	-	1.470	1.477	1.534
N1-N2 distance / Å	3.6325(2)	2.8572(1)	3.3160(2)	2.6906(1)	2.8003(1)
C3-N1-C5 fold angle / °	N/A[a]	115.369(2)	N/A[a]	111.408(2)	113.050(3)
C7-N2-C9 fold angle / °	N/A[a]	116.590(2)	N/A[a]	111.466(2)	113.569(3)

[a] **22** and **4** are not in the same boat-chair conformation as the other compounds listed therefore this angle is not listed for **22**

Single crystals of **4** were grown by slow evaporation of a dilute solution of **4** in acetonitrile (MeCN) to give colourless, block-like, crystals. **4** was found to crystallise in the P2$_1$/n space group. The asymmetric unit consists of one discrete $C_{36}H_{43}N_3$ moiety, shown in Figure 2.7a. Selected bond lengths and angles are shown in Table 2.1. Interestingly, the DACO ring in **4** displays a twist boat-chair conformation (Figure 2.7b), as this is the conformation which minimises the transannular strain between the two adjacent *N*-alkyl groups. This is reflected in the large N1-N2 distance measured in **4**

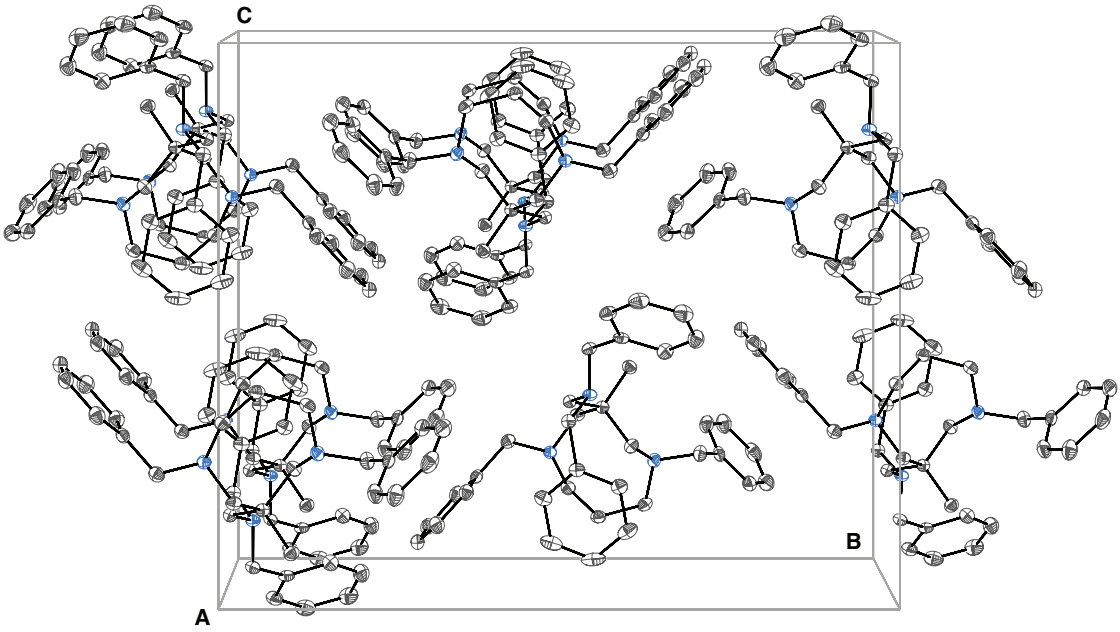

Figure 2.8: Thermal ellipsoid packing diagram for **4** illustrating the absence of π-stacking interactions. Ellipsoids are shown at the 50% probability level.

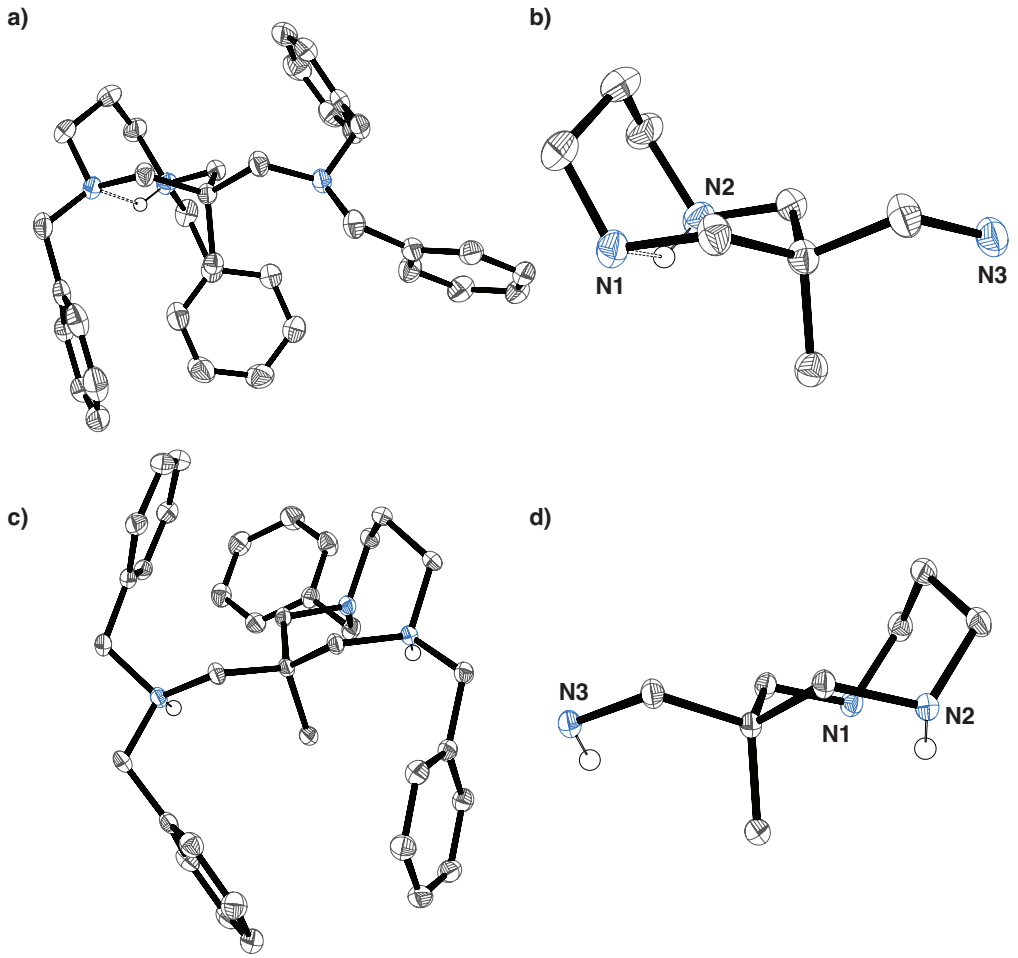

Figure 2.9: Crystal structures of [**4**·H](PF_6) and [**4**·2H](($OTf)_2$). a) Structure of [**4**·H](PF_6). Ellipsoids are shown at the 50% probability level. Counter ion and H atoms have been omitted for clarity. Hydrogen bond indicated by dashed line. b) Crystal structure of [**4**·H](PF_6) with benzyl groups removed for clarity. c) Crystal structure of [**4**·2H](($OTf)_2$). Ellipsoids are shown at the 50% probability level. Counter ions and H atoms omitted for clarity. d) Crystal structure of [**4**·2H](($OTf)_2$) with benzyl groups removed for clarity.

(3.316 Å) The mean cyclic C-C distance is 1.532 Å, in good agreement with those found for **20** and **22**. However, the average C-N distance is short when compared to **22** and is more comparable to those found in **20**, reflecting the fact that neither of these molecules are protonated whereas **22** is. Importantly, no π-stacking interactions are observed in the solid state (Figure 2.8) therefore these through space interactions, observed in the ROESY experiments can be confidently assigned as intramolecular rather than intermolecular. Serendipitously, crystal structures of both the monoprotonated and diprotonated congoners of **4** were also obtained (Figure 2.9). Colourless, needle like single crystals of [**4**·H](PF_6) precipitated after layering a reaction mixture of **4**, $CuCl_2$

and KPF_6 in wet MeCN with diethyl ether (Et_2O). Similarly, colourless block like crystals of [**4**·2H](($OTf)_2$) precipitated after layering a solution of **4** and $Zn(OTf)_2$ in wet MeCN with Et_2O.

[**4**·H](PF_6) crystallised in the $P2_1/c$ space group. The asymmetric unit was found to consist of a discrete $C_{36}H_{44}N_3$ cation and a disordered PF_6 counter anion (Figure 2.9). Selected bond lengths are reported in Table 2.1. The structure demonstrates unambiguously that the cyclic nitrogen, N2, is protonated before the acyclic amine; as would be expected based on their higher reported basicity.[199] Analysis of the crystal structure suggests a strong hydrogen bond (2.005 Å) is present between N1 and H-N2. This is reflected in the remarkably short N1-N2 distance (2.6906 Å), almost 1 Å shorter than that measured for **22**. Like **20**, the DACO ring in [**4**·H](PF_6) adopts a boat-chair conformation and has a C-N-C fold angle of 111°. This demonstrates that protonation has a significant conformational effect on **4**. The average cyclic C-C bond length remains similar to those discussed above at approximately 1.5 Å. However, protonation at N2 results in an increase in the average C-N2 bond length (1.514 Å) when compared to the unprotonated **20** (1.477 Å) and **4** (1.474 Å). These bond lengths and fold angles are similar to those previously reported for protonated DACO moieties as well as metal complexes containing the DACO moiety.[161,200,201] This suggests that *N*-alkylation should not hinder or alter the highly desirable binding properties of the DACO moiety.

[**4**·2H](($OTf)_2$) also crystallised in the $P2_1/c$ space group. The asymmetric unit was found to consist of a discrete $C_{36}H_{45}N_3$ cation and two CF_3SO_3 counter anions (Figure 2.9). Hydrogen atoms on N2 and N3 were located and refined. The DACO ring maintains the same boat-chair conformation as observed for [**4**·H](PF_6). As such, bond lengths and fold angles do not differ greatly from those reported fo [**4**·H](PF_6) (Table 2.1). This is to be expected as N3 is a considerable distance from the DACO ring consequently has little effect on its structural properties.

The ^{1}H NMR spectra of the crystals of **4**, [**4**·H](PF_6) and [**4**·2H](($OTf)_2$) were recorded and are shown in Figure 2.10. The resonances were assigned in conjunction with the corresponding HSQC and HMBC spectra. The ^{1}H NMR spectrum of **4** and [**4**·H](PF_6)

are shown in Figure 2.10a and b respectively. The spectra clearly shown that upon protonation at N2 (Figure 2.10b) the apparent singlet at 3.59 ppm arrising from $H_{6/6'}$ in **4** resolves into a pair of doublets at 3.84 and 3.65 ppm in [**4**·H](PF_6). The strong coupling constant (∼13 Hz) indicates that these doublets are a result of geminal coupling and no ^3J N-H coupling is observed. The difference in these chemical shifts (∼0.2 ppm) is a result of the relative axial/equatorial arrangement of these diastereotopic protons, arising from a change in local magnetic anisotropy brought about by protonation. An equivalent resolution of signals is observed after protonation at N3 (Figure 2.10c) as $H_{7/7'}$ are resolved into a pair of signals at 4.60 and 4.32 ppm. The doublet at 4.60 has a coupling constant (∼14 Hz) indicative of geminal coupling only, whereas the multiplet at 4.32 ppm is split further, possibly by ^3J HNCH coupling. The overlapping signals for $H_{3/3'}$ (2.46-2.39 ppm) and $H_{4/4'}$ (1.54 ppm) in **4** are resolved into pairs of multiplets for $H_{3/3'}$ (3.10 and 2.74 ppm) and $H_{4/4'}$ (2.07 and 1.74 ppm) in [**4**·H](PF_6). As above, the different chemical shifts for these pairs of protons is a result of their relative axial/

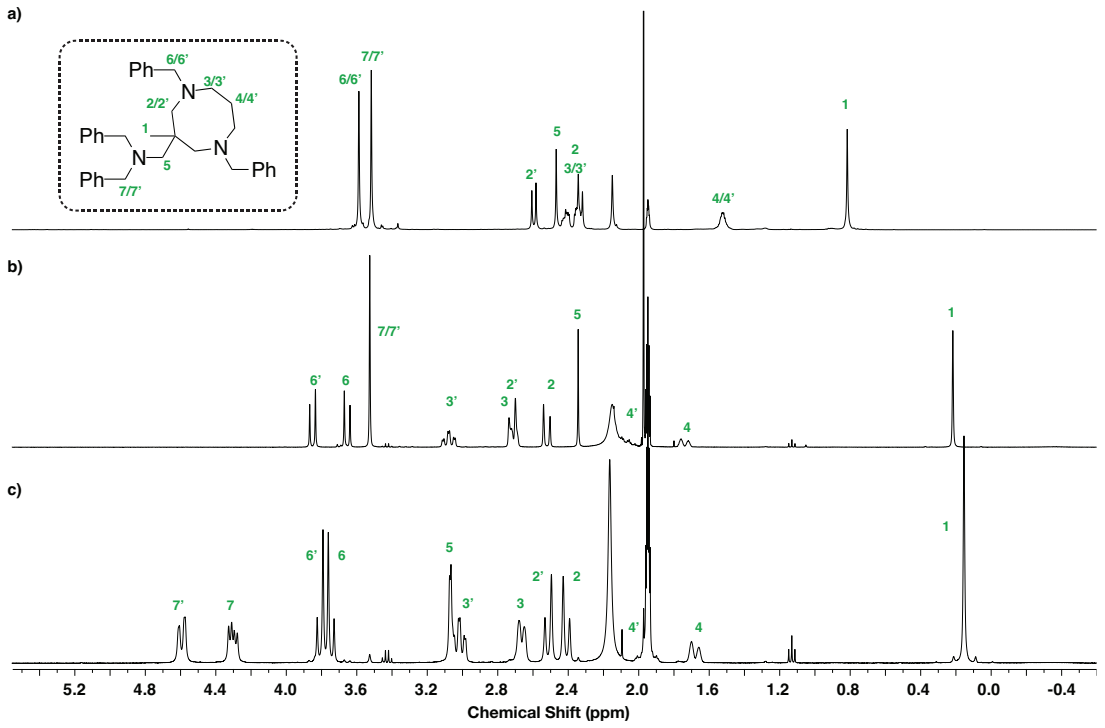

Figure 2.10: a) ^{1}H NMR spectra of **4** b) ^{1}H NMR spectra of **4** [**4**·H](PF_6). c) ^{1}H NMR spectra of **4** [**4**·2H](($OTf)_2$). 400 MHz, CD_3CN. Resonance assignments are shown in the inset and were made in conjunction with the corresponding HSQC and HMBC spectra.

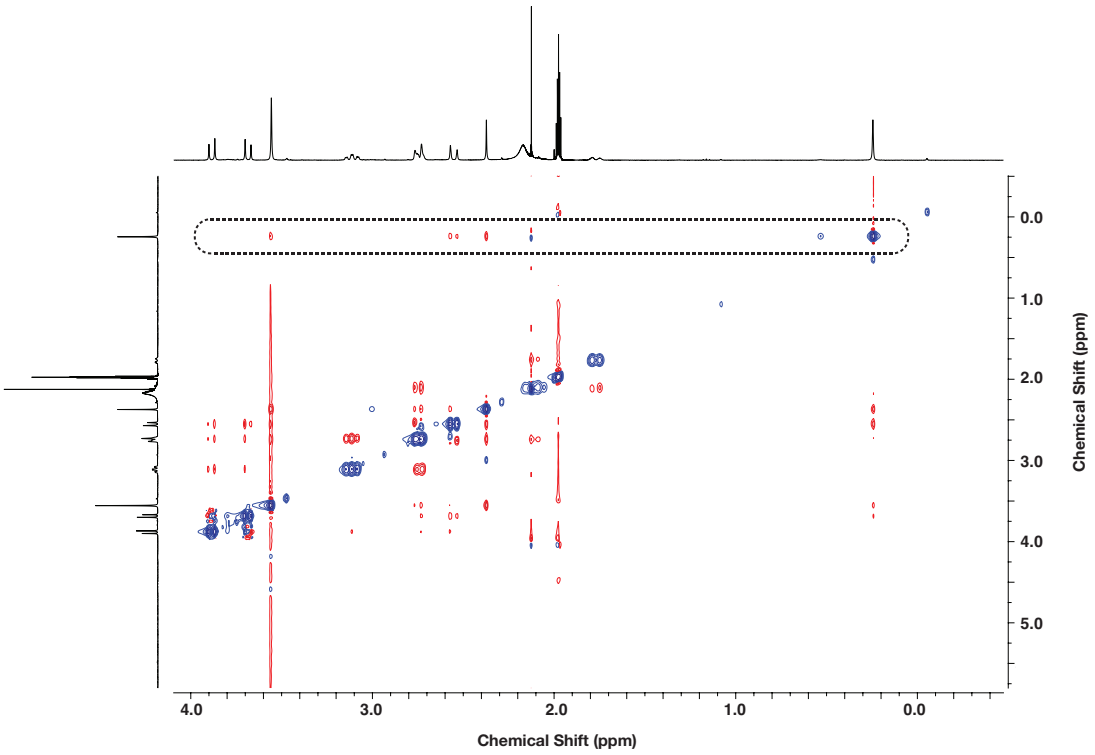

Figure 2.11: 2d ^{1}H NOE Spectrum of [**4**·H](PF$_6$). Dotted area highlights the region of the signals absent due to the decreased flexibility of [**4**·H](PF$_6$) after monoprotonation.

equatorial arrangement. Protonation at N3 ([**4**·2H]((OTf)$_2$), Figure 2.10c) results in the same general splitting pattern for the cyclic protons although their chemical shifts differ slightly.

Notably, 2d-NOE NMR experiments (Figure 2.11) shows an absence of through space coupling between H$_1$ and both H$_{3/3'}$ and H$_{4/4'}$, in stark contrast to **2** and **4** (Figure 2.5 and Figure 2.6). Furthermore, only coupling to one of the diastereotopic pair H$_{2/2'}$ is observed in [**4**·H](PF$_6$) whereas coupling to both is observed in the selective NOE NMR data reported for **4**. This is highly suggestive of a reduction in conformational flexibility of the DACO ring in **4** upon protonation at N2.

2.3 Conclusions

In conclusion, we have outlined several synthetic routes to our target ligand **1**; a novel, mesocyclic, tripodal, triamine ligand which, we have designed to stabilise late transition metal-oxos. Our modular approach to the synthesis of **22** and its derivatives has provided us with a library of synthons that will allow us to carefully tune the structural properties of metal complexes derived from **22**. Importantly, we have developed and optimised the synthesis of the mesocyclic fragment in **22**, utilising a Richman-Atkins cyclisation to give the mesocyclic compounds **19** and **20**. Furthermore, we have outlined a multitude of routes to the further derivitisation of these compounds, ultimately to give the HBr salt of the triamine skeleton, **22**, which we have shown can be alkylated to give **4**. We have probed the conformational flexibility of both **2** and **4** using a combination of NMR spectroscopy and X-ray crystallography studies. While the X-ray crystal structure obtained for **22** displayed an unusual configuration, we have shown that the corresponding freebase (**2**) maintains a high degree of flexibility in solution. Additionally, we have demonstrated that while **4** maintains a high degree of structural flexibility in solution, protonation at the N2 position results in a loss of conformational flexibility, as indicated by NMR studies. Having isolated these ligands, we now intend to study their reactivity with first row transition metals.

2.4 Experimental Section

2.4.1 Materials and Methods

All reagents and solvents were purchased from commercial sources and used as received, unless otherwise stated. All reactions with air-sensitive materials were conducted under an inert atmosphere using either standard Schlenk techniques or a nitrogen atmosphere glove box. Anhydrous DMF and MeCN were purchased and used without further purification. Anhydrous THF and Et_2O were dispensed through an Innovative Technology PureSolv EN solvent purification system and deoxygenated by purging with argon. Ammonium formate was recrystallised from ethanol before use. $CDCl_3$ was dried and de-acidified by stirring and subsequently storing over 4 Å molecular sieves and basic alumina. ^{1}H and ^{13}C NMR were recorded on either a Bruker DPX 400 MHz or Bruker Avance II 600 MHz spectrometer. ESI mass spectra were acquired using a Micromass time of flight spectrometer (tof), interfaced to a Waters 2690 HPLC. Fourier-Transform Infrared spectra were recorded using a Perkin-Elmer Spectrum I FT-IR spectrometer. Thin-layer chromatography (TLC) was performed with Analytical Chromatography alumina sheets coated with silica gel (0.25 mm). Spots were visualised under UV light. Flash column chromatography was conducted with Fluka Silica Gel 60 Å(230-400mesh).

2.4.2 Previously Reported Compounds

Table 2.2: Compounds Described which have been previously reported and their corresponding literature references.

Compound Number	Structure	Reference
7	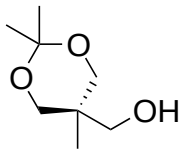	188
8	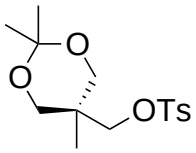	189,190
9	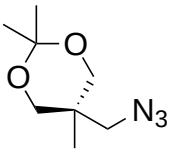	191
11	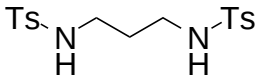	172
12	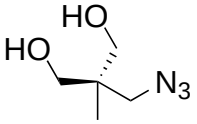	191
17	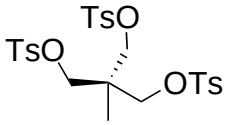	193

2.4.3 Synthesis of 2-(azidomethyl)-2-methylpropane-1,3-diyl *bis*-tosylate (9)

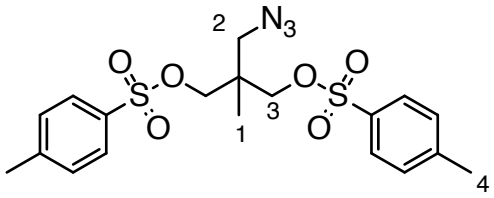

12 (3.53 g, 24 mmol)[191] was dissolved in THF (50 mL) and added to a solution of NaOH (9 g) in water (9 mL). Tosyl chloride (11.6 g, 61 mmol) in THF (10 mL) was added dropwise with vigorous stirring. The reaction mixture was stirred for a further 16 h at room temperature. The mixture was diluted with water (100 mL) and then extracted with $CHCl_3$ (3 x 50 mL). The organic layer was washed with brine (3 x 100 mL) then dried over $MgSO_4$. The solvent was removed *in vacuo* to give a colourless oil. The crude product was purified by column chromatography (Hexane: EtOAc, 4:1) to give **13** (7.2 g, 64%) as an off-white solid.

^{1}H NMR (400 MHz, $CDCl_3$) δ = 0.93 (s, 3H, H_1), 2.47 (s, 6H, H_4), 3.26 (s, 2H, H_2), 3.78 (s, 4H, H_3), 7.38 (d, *J* = 8.1, 4H, Ar-H), 7.76 (d, *J* = 8.1, 4H, Ar-H).

^{13}C NMR (101 MHz, $CDCl_3$) δ = 17.0, 21.8, 39.7, 53.6, 70.7, 128.0, 130.1, 132.1, 145.4.

ν_{max} /cm^{-1}: 2112.16, 1370, 1289, 1191, 1176, 1098, 1034, 965, 866, 832, 814, 665, 603, 554.

HRMS (*m/z* -ESI): Found: 476.0961 (M^+ + Na predicted mass: 476.0926 $C_{19}H_{23}N_3O_6S_2Na$)

2.4.4 Synthesis of 3-(azidomethyl)-3-methyl-1,5-ditosyl-1,5-diazocane (14)

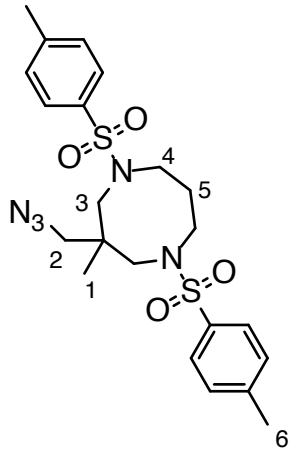

19 (800 mg, 1.3 mmol) was dissolved in diethylene glycol (25 mL). Sodium azide (252 mg, 3.9 mmol) was added and the reaction mixture was stirred at 135 °C for 5 days. The reaction mixture was cooled and diluted with water (25 mL). The result- ing emulsion was extracted with DCM (3 25 mL). The organic layer was collected and dried over $MgSO_4$ and the solvent removed *in vacuo*. The crude product was purified by column chromatography (EtOAc : Hexane : Triethylamine, 45 : 45 : 10) to give azide **14** (280 mg, 44%) as a white powder.

^{1}H NMR (400 MHz, $CDCl_3$) δ = 1.15 (s, 3H, H_1), 1.82-2.02 (m, 2H, H_5), 2.46 (s, 6H, H_6), 2.96-3.29 (m, 8H, $H_{3/4}$), 3.54 (s, 2H, H_2), 7.36 (d, *J* = 8.1, 4H, H-Ar), 7.68 (d, *J* = 8.1, 4H, H-Ar).

^{13}C NMR (101 MHz, $CDCl_3$) δ = 17.0, 21.8, 25.7, 39.7, 53.6, 68.0, 70.7, 128.0, 130.1, 132.1, 132.1, 145.4

ν_{max} /cm^{-1}: 1156, 1335, 2103.

HRMS (*m/z* -ESI): Found: 492.1730 (M^+ + H. $C_{22}H_{30}N_5O_4S_2$ predicted mass: 492.1695).

2.4.5 Synthesis of (2,2,5-trimethyl-1,3-dioxan-5-yl)methanamine (15)

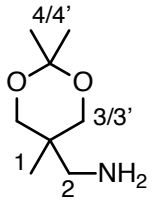

Azide **9** (3.52 g, 19 mmol) and ammonium formate (4.87 g, 76 mmol) were added to degassed methanol (100 mL) and stirred until the ammonium formate completely dissolved. 5% Pd/C (365 mg, 10 wt%) was then added and the reaction mixture stirred for 3 hours at room temperature. The reaction mixture was then filtered through a pad of Celite and the methanol removed *in vacuo*. The residue was taken up into distilled water (10 mL) and washed with Et_2O (3 20 mL). The aqueous layer was then basified with KOH (10 g) and extracted with CH_3CN (5 10 mL). The organic layer was collected and dried over $MgSO_4$. The solvent was removed *in vacuo* to give **15** (1.50 g, 50%) as a colourless oil.

^{1}H NMR (600 MHz, $CDCl_3$) δ = 0.80 (s, 3H, H_1), 0.99 (s, 2H, H_{NH_2}), 1.38 (s, 3H, H_4), 1.42 (s, 3H, $H_{4'}$), 2.78 (s, 2H, H_2), 3.57 (d, J = 11.7, 2H, H_3), 3.62 (d, J = 11.7, 2H, $H_{3'}$).

^{13}C NMR (151 MHz, $CDCl_3$) δ = 17.9, 21.0, 26.5, 34.2, 46.3, 67.2, 97.8.

HRMS (*m/z* -ESI): Found: 160.1342 (M^+ + H. $C_8H_{17}NO_2$ predicted mass: 160.1338).

2.4.6 Synthesis of 1,3-dibromo-2-(bromomethyl) -2-methylpropane (18)

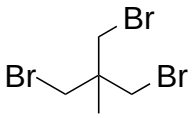

17 (46 g, 79 mmol) and NaBr (83 g, 790 mmol) were heated in diethylene glycol (250 mL) at 145 °Cfor 18 hours. After cooling, the reaction mixture was diluted with deionised water (250 mL), mixed vigorously, then transferred to a separating funnel. The more dense oil (**18**) was collected. The aqueous layer was washed with Et_2O (3 50 mL). The organic extracts were combined with the oil and dried over $MgSO_4$. The solvent was removed *in vacuo* to give **18** (18.5 g, 76%) as a pale yellow oil.

^{1}H NMR (400 MHz, $CDCl_3$) δ = 1.29 (s, 3H), 3.50 (s, 6H).[194]

2.4.7 Synthesis of (3-methyl-1,5-ditosyl-1,5-diazocan-3-yl)methyltosylate (19)

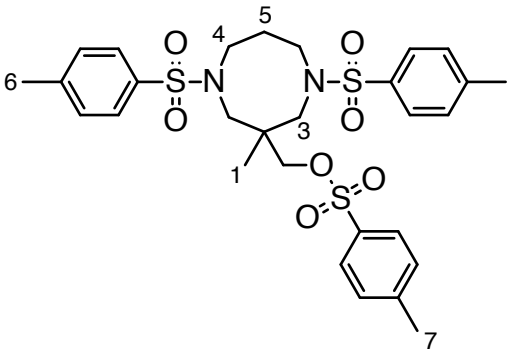

In a glove box, *N,N*-(propane-1,3-diyl)bis-tosylate **11** (3.80 g, 9.93 mmol) was dissolved in anhydrous DMF (100 mL). NaH, as a 60% dispersion in mineral oil (1.0 g, 20 mmol) was added and the solution stirred until the evolution of hydrogen gas ceased. The reaction vessel was transferred to a Schlenk line and heated at 145 °C for 1 hour. A solution of **17** (5.786 g, 9.9 mmol) in anhydrous DMF (60 mL) was then added drop-wise by cannula. The reaction mixture was then heated at 145 °C for a further 24 hours. The DMF was removed by distillation and the residue was taken up into $CHCl_3$. The organic layer was washed with water (3 50 mL) and brine (3 50 mL) then dried over $MgSO_4$. The solvent was removed *in vacuo*. The crude product was purified by column chromatography (EtOAc : hexane : triethylamine, 35 : 60 : 5) to give **19** (591 mg, 10%) as an off-white crystalline solid.

^{1}H NMR (600 MHz, $CDCl_3$) δ = 1.14 (s, 3H, H_1), 1.92 (m, 2H, H_5), 2.44 (s, 6H, , H_6), 2.45 (s, 3H, H_7), 3.11-3.21 (m, 8H,, $H_{3/4}$), 4.05 (s, 2H, H_2), 7.32 (d, *J* = 8.0, 4H, H-Ar), 7.36(d, *J* =8.1, 2H, H-Ar), 7.62(d, *J* = 8.2, 4H, H-Ar), 7.84 (d, *J* = 8.3, 2H, H-Ar).

^{13}C NMR (151 MHz, $CDCl_3$) δ = 21.6, 21.7, 21.8, 28.8, 39.8, 49.7, 53.2, 76.4, 127.5, 128.2, 130.0, 130.0, 132.7, 134.9, 143.9, 145.0.

ν_{max} /cm^{-1}: 1156, 1174, 1307, 1336.

HRMS (*m/z* -ESI): Found: 643.1580 (M^+ + Na. $C_{29}H_{36}N_2O_7S_3Na$ predicted mass: 643.1582).

Melting point: 86-88 °C.

2.4.8 Synthesis of 3-(bromomethyl)-3-methyl-1,5-ditosyl-1,5-diazocane (20)

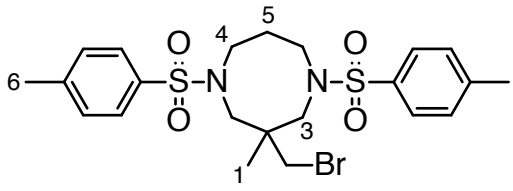

In a glove box, *N,N*-(propane-1,3-diyl)bis-tosylate **11** (4.7 g, 12.3 mmol) was dissolved in anhydrous DMF (200 mL). NaH, as a 60% dispersion in mineral oil (0.985 g, 24.6 mmol) was added and the solution stirred until the evolution of hydrogen gas ceased. The reaction vessel was transferred to a Schlenk line and heated at 145 °C for 1 hour. A solution of 1,3-dibromo-2-(bromomethyl)-2-methylpropane **18** (3.8 g, 12.3 mmol) in anhydrous DMF (50 mL) was then added dropwise by cannula. The reaction mixture was heated at 145 °C for a further 24 hours. The DMF was removed by distillation and the residue was taken up into Et_2O (150 mL). The Et_2O solution was washed with water (3 50 ml) and brine (3 50 ml) and dried over $MgSO_4$. The solvent was removed *in vacuo*. The crude product was purified by recrystalisation from the minimum amount of boiling methanol. The product was collected by vacuum filtration and washed with cold methanol (3 10 mL) to give **20** as an off white solid (3.1 g, 48%).

^{1}H NMR (400 MHz, $CDCl_3$) δ = 1.28 (s, 3H, H_1), 1.96 (m, 2H, H_5), 2.46 (s, 6H, H_6), 3.09-3.28 (m, 8H, $H_{3/4}$), 3.64 (s, 2H, H_2), 7.35 (d, *J* = 7.9, 4H, H-Ar), 7.69 (d, *J* = 8.0, 4H, H-Ar)

^{13}C NMR (101 MHz, $CDCl_3$) δ = 21.1, 23.1, 28.1, 39.1, 43.4, 49.1, 53.8, 127.0, 129.4, 134.3, 143.4.

ν_{max} /cm^{-1}: 547, 572, 653, 706, 755, 800, 845, 1018, 1089, 1156, 1260, 1306, 1335, 1383, 1457, 1494, 1598, 2860, 2870, 2924, 2963.

HRMS (*m/z* -ESI): Found: 551.0652 (M^+ + Na. $C_{22}H_{29}N_2O_4S_2Br$ predicted mass: 551.0650).

Melting point: 140-143 °C.

2.4.9 Synthesis of (3-methyl-1,5-ditosyl-1,5-diazocan-3-yl)- methanamine (21)

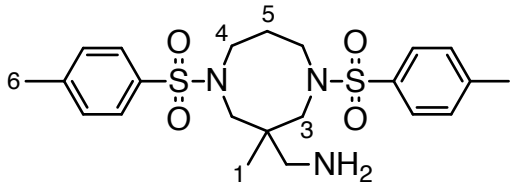

14 (0.280 g, 0.57 mmol) and ammonium formate (0.144 g, 2.28 mmol) were added to degassed methanol (100 mL) and stirred until the ammonium formate completely dissolved. 5% Pd/C (0.056 g, 20 wt%) was then added and the reaction mixture stirred for 18 h at room temperature. The reaction mixture was filtered through a pad of celite and the methanol removed *in vacuo*. The residue was taken up into distilled water (10 mL) and washed with Et_2O (3 20 mL). The aqueous layer was basified with KOH (10 g) and extracted with CH_3CN (5 10 mL). The organic layer was collected and dried over $MgSO_4$. The solvent was removed *in vacuo* to give **21** (0.140 g, 53%).

^{1}H NMR (600 MHz, $CDCl_3$) δ = 1.06 (s, 3H, H_1), 1.87 (m, 2H, H_5), 2.43 (s, 6H, H_6), 2.70 (s, 2H, H_2), 2.93 (d, *J* = 15.1, 2H, H_3), 3.08-3.25 (m, 6H, $H_{3'/4}$), 7.31 (d, *J* = 8.2, 4H, H-Ar), 7.66 (d, *J* = 8.2, 4H, H-Ar).

^{13}C NMR (151 MHz, $CDCl_3$) δ = 21.5, 28.1, 40.4, 47.8, 49.8, 53.5, 127.4, 129.8, 135.1, 143.6.

ν_{max} /cm^{-1}: 1151, 1327, 3151, 3310.

HRMS (*m/z* -ESI): Found: 466.1833 (M^+ + H. $C_{22}H_{32}N_3O_4S_2$ predicted mass: 466.1790).

2.4.10 Synthesis of N-((3-methyl-1,5-ditosyl-1,5-diazocan-3-yl)methyl)- tosylamide (23)

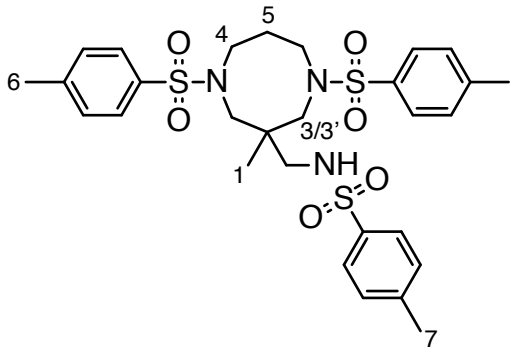

20 (9.0 g, 17 mmol) and sodium tosylamide (9.85 g, 51 mmol) were heated at 145 °C in anhydrous DMF (200 mL) for 4 days. Once the reaction mixture had cooled, the solvent was removed *in vacuo*. The crude reaction mixture was recrystallised in the minimum amount of boiling methanol. The resulting white precipitate was collected by filtration and washed with cold methanol to give **23** (8.0 g, 76%). The crude product was then recrystallised from acetone.

^{1}H NMR (400 MHz, $CDCl_3$) δ = 1.09 (s, 3H, H_1), 1.85 (m, 2H, H_5), 2.41 (s, 3H, H_7), 2.43 (s, 6H, H_6), 2.7-3.5 (m, 8H, $H_{2/3/4/4'}$), 3.48 (d, *J* = 5.0, 2H, $H_{3'}$), 7.27-7.37 (m, 4H, H-Ar), 7.63 (d, *J* = 8.0, 2H), 7.77 (d, *J* = 8.0, 2H, H-Ar).

^{13}C NMR (101 MHz, $CDCl_3$) δ = 21.7, 22.1, 28.5, 39.8, 48.1, 50.7, 127.0, 127.6, 129.9, 130.0, 134.4, 137.5, 143.2, 144.1.

ν_{max} /cm^{-1}: 3290, 2925, 2286, 2050, 1980, 1598, 1494, 1458, 1382, 1328, 1305, 1216, 1153, 1089, 1017, 967, 847, 811, 752, 739, 705, 653, 567.

HRMS (*m/z* -ESI): Found: 620.1931 (M^+ + H. $C_{29}H_{37}N_3O_6S_3$ predicted mass: 620.1931).

Melting point: 110-114 °C.

2.4.11 General procedure for the deprotection of N-tosyl protected amines to give 22 using 33% HBr in acetic acid and phenol

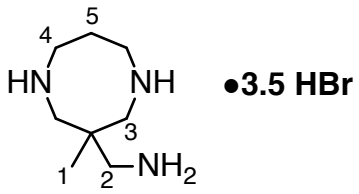

A solution of 33% HBr in acetic acid (1 mL) was added to the protected amine (0.25 mmol) and phenol (1 g). The reaction mixture was heated at 90 °C for 16 hours. The temperature was lowered to 60 °C and 33% HBr in acetic acid (1 mL) was added and the reaction mixture heated for a further 5 hours. The reaction mixture was cooled in the freezer at 40 °C overnight. The resulting white precipitate was collected by filtration and washed with Et_2O (5 mL). To give **22** as an off white solid (10%). Crystals of **22** suitable for X-ray diffraction were grown by slow diffusion of ethanol into a solution of **22** in water.

^{1}H NMR (400 MHz, D_2O) δ = 1.24 (s, 3H, H_1), 2.23 (m,2H,, H_5), 3.14 (s, 2H, H_2), 3.46-3.24 (m, 8H, $H_{3/4}$).

^{13}C NMR (101 MHz, D_2O) δ = 18.8, 19.2, 42.6, 43.8, 45.5, 47.5.

HRMS (*m/z* -ESI): Found: 158.1695 (M^+ + H. $C_8H_{20}N_3$ predicted mass: 158.1652).

Melting point: Decomposes at approximately 255 °C.

2.4.12 General procedure for the deprotection of *N*-tosyl protected amines to give 22 using concentrated H_2SO_4

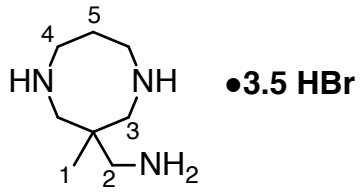

Concentrated H_2SO_4 (1 mL) was added to the protected amine **22** (1 mmol). The reaction mixture was heated under argon at 160 °C for 1 hour. The reaction mixture was cooled to 0 °C in an ice-bath and ethanol (10 mL) followed by Et_2O (8 mL) was added dropwise. The reaction mixture was cooled in the fridge at 2 °C for 16 hours. The resulting brown precipitate was collected by filtration onto a pad of celite. The precipitate and the celite were then transferred to a round-bottomed flask to which water (10 mL) and activated carbon were added. The mixture was refluxed for 1.5 hours. The insoluble materials were removed by filtration and the solvent was removed under reduced pressure. The resulting brown residue was taken up into 48% hydrobromic acid (1 mL) and to this solution ethanol (20 mL) was added dropwise. The resulting white precipitate, **22** (50%) was collected by filtration and washed with cold Et_2O (5 mL).

2.4.13 General procedure for the generation of freebase 2

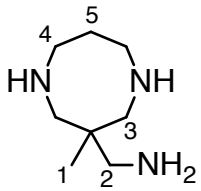

22 was dissolved in the minimum amount of deionised water. KOH (10 eq.) and toluene (20 mL) were then added. The toluene solution was then heated under reflux with a DeanStark trap for 24 hours. After cooling, any insoluble material was removed by filtration and the solvent removed under vacuum to give freebase **2** as a colourless oil.

^{1}H NMR (600 MHz, $CDCl_3$) δ = 0.76 (s, 3H, H_1), 1.65-1.77 (m, 2H, H_5), 2.58 (s, 2H, H_2), 2.58 (d, *J* = 14.1, 2H, H_3), 2.80 (d, *J* = 14.1, 2H, $H_{3'}$), 2.843.02 (m, 4H, $H_{4/4'}$).

^{13}C NMR (151 MHz, $CDCl_3$) δ = 20.98, 28.49, 38.59, 49.08, 49.20, 53.79.

ν_{max} /cm^{-1}: 3295, 2903, 2862, 1595, 1459, 1393, 1365, 1293, 1230, 1146, 1069, 880, 845, 810, 769, 747, 692, 639, 623, 616, 609, 601, 593, 585, 578, 570, 563, 555.

HRMS (*m/z* -ESI): Found: 158.1674 (M^+ + H. $C_8H_{20}N_3$ predicted mass: 158.1652).

2.4.14 Synthesis of N,N-dibenzyl-1-(N,N-1,5-dibenzyl-3-methyl-1,5- diazocan-3-yl)methanamine (4)

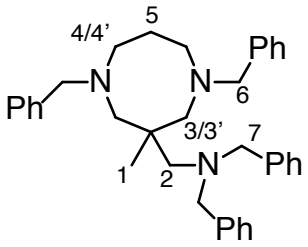

22 (1.1 g, 2.7 mmol) was suspended in CH_3CN (30 mL). Benzyl bromide (1.88 g, 1.3 mL, 11.0 mmol) and K_2CO_3 (7.6 g, 55 mmol) were added. The reaction mixture was heated at reflux for 16 hours. After this the insoluble material was removed by filtration and the solvent was removed *in vacuo*. The resulting yellow oil was dissolved in H_2O (5 mL) and added to a suspension of sodium hydroxide (5 g) in toluene (50 mL). The toluene solution was then heated under reflux with a DeanStark trap for 24 hours. After cooling, the insoluble material was removed by filtration and the solvent removed under vacuum to give **4** (0.988 g, 70%) as a white solid.

^{1}H NMR (600 MHz, $CDCl_3$) δ = 0.95 (s, 3H, H_1), 1.55-1.70 (m, 2H, H_5), 2.31-2.56 (m, 6H, $H_{3/4}$), 2.58 (s, 2H, H_2), 2.71 (d, J = 14.1, 2H, $H_{4'}$), 3.64 (s, 4H, H_7), 3.74 (m, 4H, H_6), 6.57-7.93 (m, 20H, H-Ar).

^{13}C NMR (151 MHz, $CDCl_3$) δ = 22.2, 28.3, 42.5, 54.5, 60.7, 61.6, 62.1, 65.0, 126.4, 126.6, 127.9, 127.9, 128.4, 129.1, 139.9, 141.9.

ν_{max} /cm^{-1}: 3084, 3063, 3025, 2965, 2949, 2939, 2922, 2888, 2814, 2780, 2711, 2049, 1940, 1870, 1803, 1602, 1585, 1493, 1468, 1451, 1357, 1332, 1302, 1283, 1243, 1212, 1192, 1176, 1145, 1115, 1090, 1071, 1062, 1045, 1027, 984, 972, 935, 922, 906, 888, 861, 838, 821, 760, 744, 731, 695, 632, 613, 583, 569, 555.

HRMS (*m/z* ESI): Found: 518.3530 (M^+ + H. $C_{36}H_{44}N_3$ predicted mass: 518.3535).

Melting point: 88-90 °C.

2.4.15 NMR Data for [4·H](PF$_6$)

^{1}H NMR (600 MHz, CD_3CN) δ = 0.23 (s, 3H), 1.69-1.77 (m, 2H) 2.03-2.10 (m, 2H), 2.34 (s, 2H), 2.52 (d, *J* = 14.2 Hz, 1H), 2.74-2.66 (m, 4H), 2.99-3.13 (m, 2H), 3.84 (d, *J* = 13.3 Hz, 2H), 3.65 (d, *J* = 14.7 Hz, 2H), 7.27-7.45 (m, 20H).

For assignments see Figure 2.10.

^{13}C NMR (151 MHz, CD_3CN) δ = 21.2, 21.4, 37.2, 56.7, 60.9, 61.7, 63.7, 129.4, 130.0, 130.0, 130.3, 131.7, 134.3, 140.4.

2.4.16 NMR data for [4·2H]((OTf)$_2$)

^{1}H NMR (600 MHz, CD_3CN) δ = 0.15 (s, 3H), 1.68-1.71 (m, 2H), 1.95-1.98 (m, 2H), 2.52 (d, *J* = 14.5 Hz, 2H), 2.42 (d, *J* = 14.5 Hz, 2H), 2.65-2.75 (m, 2H), 2.98-3.13 (m, 4H), 3.76 (d, *J* = 13.0 Hz, 2H), 3.82 (d, *J* = 13.1 Hz, 2H), 4.27-4.35 (m, 2H), 4.61 (d, *J* = 12.6 Hz, 2H), 7.23-7.69 (m, 20H).

For assignments see Figure 2.10.

^{13}C NMR (151 MHz, CD_3CN) δ = 18.9, 20.8, 35.4, 55.7, 56.1, 59.1, 63.2, 63.6, 129.2, 130.1, 130.2, 130.4, 131.6, 131.9, 133.6, 133.7.

2.4.17 Crystallographic Information

The X-ray intensity data were measured at the temperatures given in Table 2.3 using an Oxford Cryosystems low temperature device using a MiTeGen micromount. See Table 2.3 for collection parameters and exposure time. Bruker APEX software was used to correct for Lorentz and polarization effects. Data were corrected for absorption effects using the Multi-Scan method (SADABS). The structures were solved and refined using the Bruker SHELXTL Software Package

Table 2.3: Crystal data and refinement parameters for **22**, **20**, [**4**·H](PF_6) and [**4**·2H](($OTf)_2$)

.

	22	**20**	[**4**·H](PF_6)	[**4**·2H](($OTf)_2$)
Empirical formula	$C_{16}H_{45}Br_7N_6$	$C_{22}H_{29}Br_{0\cdot 68}Cl_{0\cdot 32}N_2O_4S_2$	$C_{36}H_{44}F_6N_3P$	$C_{38}H_{45}F_6N_3O_6S_2$
Formula weight	879.94	515.05	663.71	817.89
Temperature / K	100(2)	100(2)	100(2)	100(2)
Crystal system	Trigonal	Monoclinic	Monoclinic	Monoclinic
Space group	$R\bar{3}$	$P2_1/c$	$P2_1/c$	$P2_1/c$
Unit cell dimensions	a = 10.9261(5) Å	a = 10.9164(3) Å	a = 11.1337(5) Å	a = 19.6192(13) Å
	b = 17.0382(7) Å	b = 16.2651(4) Å	b = 124.2066(10) Å	b = 19.6192(13) Å
	c = 12.3817(3) Å	c = 19.0039(5) Å	c = 15.0351(6) Å	c = 22.6973(15) Å
	α= 90°	α= 90°	α= 90°	α= 90°
	β= 90°	β= 96.0531(13)°	β= 93.2134(9)°	β= 107.5700(10)°
	γ= 120°	γ= 90°	γ= 90°	γ= 90°
Volume / Å^3	7566.0(11)	2351.51(17)	3368.96(15)	3863.1(3)
Z	9	4	4	4
Density (calculated) / Mg m^{-3}	1.738	1.455	1.309	1.406
Crystal Size / mm^3	0.100 x 0.100 x 0.150	00.220 x 0.150 x 0.100	0.16 x 0.08 x 0.05	0.260 x 0.240 x 0.220
Reflections collected	25098	31099	122896	185743
Independent reflections	3863 [$R_{(int)}$ = 0.0281]	4316 [$R_{(int)}$ = 0.0410]	6919 [$R_{(int)}$ = 0.0.0212]	11856 [$R_{(int)}$ = 0.0381]
Final R indices [I>2σ(I)]	R_1 = 0.0337 wR_2 = 0.0742	R_1 = 0.0488 wR_2 = 0.1115	R_1 = 0.0482 wR_2 = 0.1204	R_1 = 0.0372 wR_2 = 0.0899
R indices (all data)	R_1 = 0.0429 wR_2 = 0.0777	R_1 = 0.0505 wR_2 = 0.1124	R_1 = 0.0533 wR_2 = 0.1252	R_1 = 0.0520 wR_2 = 0.0989

Chapter 3

An Investigation Into the Coordination Behaviour of Two 1,5-Diaza Mesocyclic Ligands

Publications resulting from work in this Chapter: Andrew D. Ure, Isabel Abnades Lzaro, Michelle Cotter, Aidan R. McDonald, *Org. Biomol. Chem.* 2016, **14**, 483-494.

3.1 Introduction

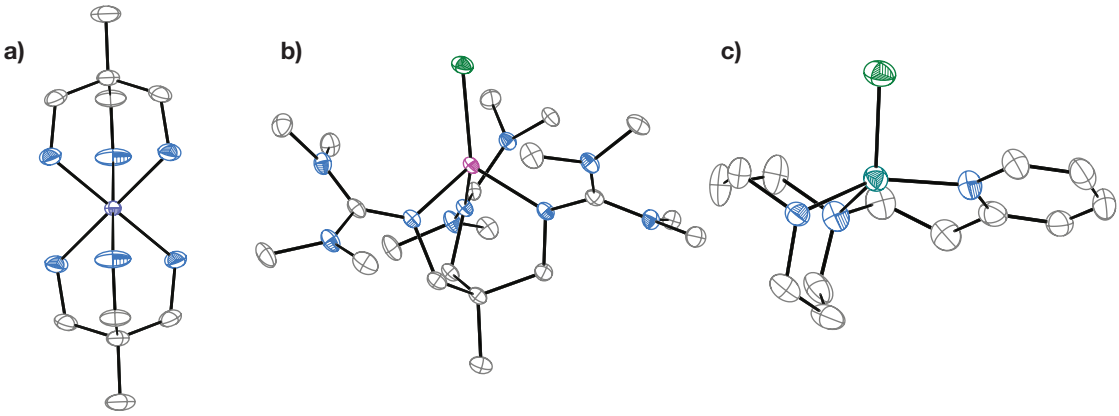

Figure 3.1: Representative examples of tridentate ligands. Thermal ellipsoid diagrams with ellipsoids shown at the 50% probability level. Counter anions and H-atoms have been ommited for clarity. a) $[Ni(TAME)_2](Cl)_2$[202] b) [Co(guanTAME)(Cl)](OTf)[175] c) [Cu(L8)Cl](BPh_4)[159] *N*-isopropyl group has been ommited for clarity.

In Chapter 1, we outlined a set of criteria that we believe, if met, would lead to the formation of stable terminal late transition metal-oxos. A key facet of this argument relied on our ability to synthesise *pseudo*-tetrahedral precursor complexes. Importantly, these precursor complexes must contain a vacant coordination site so as to facilitate the introduction of the oxo moiety. In order to achieve this, we reasoned that we would first require tridentate nitrogen donor ligands that are capable of binding metals in a tripodal manner. Several notable examples of this type of ligand exist in the literature and representative crystal structures of these are shown in Figure 3.1. Figure 3.1a shows the crystal structure of $[Ni(TAME)_2](Cl_2)$. This represents the typical binding mode of 1,1,1-tris(aminomethyl)ethane (TAME), which forms octahedral, 2:1 ligand to metal complexes.[202] This is a result of the lack of steric bulk associated with this ligand framework. Monoalkylation of each of the amino groups in TAME to give *N*,*N*′,*N*″-Trimethyl-1,1,1-tris(aminomethyl)ethane (Me_3TAME), failed to prevent the formation of 2:1 complexes while peralkylation of TAME to give 1,1,1-tris(*N*,*N*-dimethylamino)methylethane (Me_6TAME) resulted in the ligand binding in a bidentate mode.[174] This demonstrated that simply alkylating the amino groups of TAME was not a sufficient strategy to gain control over the coordination behaviour of this ligand.

Conversion of the amino functionalities in TAME to tetramethylguanidine groups gave 1,1,1-tris(2*N*- 1,1,3,3-tetramethylguanidino) methylethane (guanTAME). The corresponding cobalt complex, [Co(guanTAME)Cl](OTf), is shown in Figure 3.1b.[175] In obtaining the crystal structure of this complex it was demonstrated that guanTAME was capable of forming *pseudo*-tetrahedral metal complexes, albeit with a bound chloride in the axial position. This is most likely due to the increased steric bulk of the tetramethyl guanidine groups, which prevented the binding of a second molecule of guanTAME. These results suggested that with the correct ligand design, the TAME framework was capable of forming 1:1 complexes. However, in addition to this report of a *pseudo*-tetrahedral complex of guanTAME, other reports have described the binding of guanTAME in a bidentate manner.[176] From our perspective, this is undesirable as we require our ligand to bind reliably in a tripodal manner.

Interestingly, the Itoh group have reported the synthesis of a variety of Cu^{I} and Cu^{II} complexes of 1-isopropyl-5-(2-(pyridin-2-yl)ethyl)-1,5-diazocane (L8), based on the 1,5-diazacyclooctane (DACO) framework (Figure 3.2.[157–160] An X-ray crystal structure of a representative example of one of these complexes, [Cu(L8)Cl](BPh_4), is shown in Figure 3.1c.[159] L8 binds to the metal *via* an N3 donor set, resulting in distorted tetrahedral metal complexes. Importantly, on reaction with O_2, the Cu^{I} complexes have been shown to form mononuclear end-on Cu-superoxo species.[157–160] In contrast, the Itoh group also showed that complexes of the seven membered ring analogue of L8 gave rise to a bis(μ-oxido) dicopper(III) species upon reaction with O_2.[158] This difference in reactivity was attributed to the subtle differences in molecular geometry afforded by the

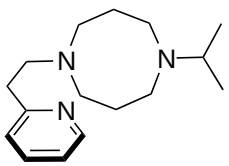

'L8'

Figure 3.2: A chemdraw representation of 1-isopropyl-5-(2-(pyridin-2-yl)ethyl)-1,5-diazocane (L8). This ligand has been shown to stabilise a Cu^{III}-superoxo species by the Itoh group.[157–160]

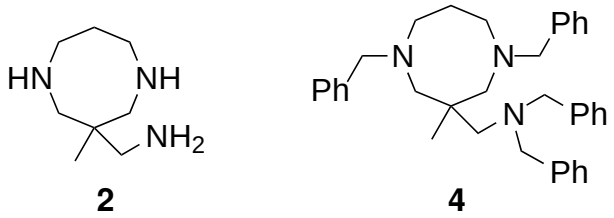

2 **4**

Figure 3.3: Ligands **2** and **4** synthesised in Chapter 2.

variation in ring size. In particular, the N-N distance within the cyclic diamine moiety of L8 (2.9 Å) was shown to be a key factor in driving the formation of the mononuclear species. While this family of complexes has be utilised to significantly advance our understanding of the reactivity of mononuclear copper-oxygen adducts, the system can not stabilise a terminal Cu-oxo species, as the ligand framework has been shown to be highly susceptible to oxidation.[157,159,160]

In Chapter 2 we reported the synthesis of two new ligands, **2** and **4**, which we believed would overcome the drawbacks of the tridentate, tripodal ligands discussed above. The triamines **2** and **4** incorporated several design features that we believed would favour the stabilisation of late transition metal-oxo species which, we argue will form potent oxidants. Both triamines **2** and **4** can be considered as derivatives of TAME in which we have linked two of the amino groups with a propane linker. In doing so, we have introduced a DACO mesocyclic moiety into our ligand design which, we believed would provide these ligands with a higher degree of structural pre-organisation with regards to complex formation (*c.f.* TAME). We reasoned that this would encourage the consistent binding of triamines **2** and **4** in a tripodal manner. We postulated that this would overcome the issue of variable denticity which has been observed in TAME and guanTAME. Additionally, we believed that inclusion of the DACO moiety would provide additional steric bulk to the ligand framework and prevent the formation of 2:1 complexes. We also showed that the steric bulk of the ligand could be readily tuned through *N*-alkylation of **2** to give **4**, which should allow us to carefully control the steric and electronic properties of the ligands and consequently, the resulting complexes.

In this chapter, we describe our investigations into the coordination chemistry of the

two ligands, **2** and **4**, synthesised in Chapter 2. While the overall goal of this project relates to the synthesis of late transition metal complexes, we wished to develop a thorough understanding of the coordination chemistry of **2**, in order to help evaluate and guide our ligand design.

3.2 Synthesis and Characterisation of Coordination Complexes of 2.

3.2.1 Iron Complexes of 2

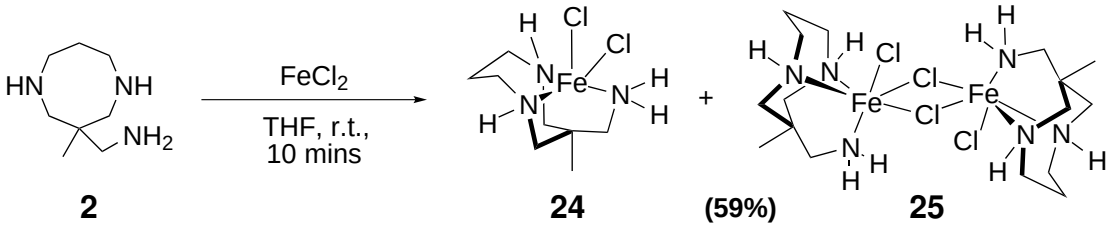

Scheme 3.1: Synthesis of Iron complexes of **2**. The drawn products, **24** and **25** were identified by x-ray crystallography. The yield reflects the total yield of the two products.

We reacted a colourless solution **2** in tetrahydrofuran (THF) with an orange/brown THF solution of anhydrous $FeCl_2$. Upon mixing, the intense colour of the reaction mixture began to fade to pale yellow. After 10 minutes, addition of diethyl ether caused the precipitation of a pale yellow solid. This precipitate was analysed by ^{1}H nuclear magnetic resonance (NMR) spectroscopy.

Figure 3.4 shows the paramagnetically shifted ^{1}H NMR spectrum of the product of the reaction shown in Scheme 3.1. Compared to a standard ^{1}H NMR spectrum, these signals are considerably broadened and spread over a wide ppm range. This is a result of the presence of unpaired electrons within the sample. The interaction of unpaired spin density on the metal with the ^{1}H nuclear spin significantly reduces the relaxation time of the protons within the molecule.[203] Therefore, in order to obtain a spectrum, experimental parameters must first be modified. Namely, a short aquisition time and short delay time are utilised. This allows the resonances to be observed in what is known as a paramagnetically shifted ^{1}H NMR spectrum.

Due to the broad nature of the peaks, the integration of the peaks in paramagnetically shifted ^{1}H NMR spectra is unreliable and any fine structure as a result of nuclear coupling is lost. Nevertheless, Figure 3.4 still provides a wealth of information. The

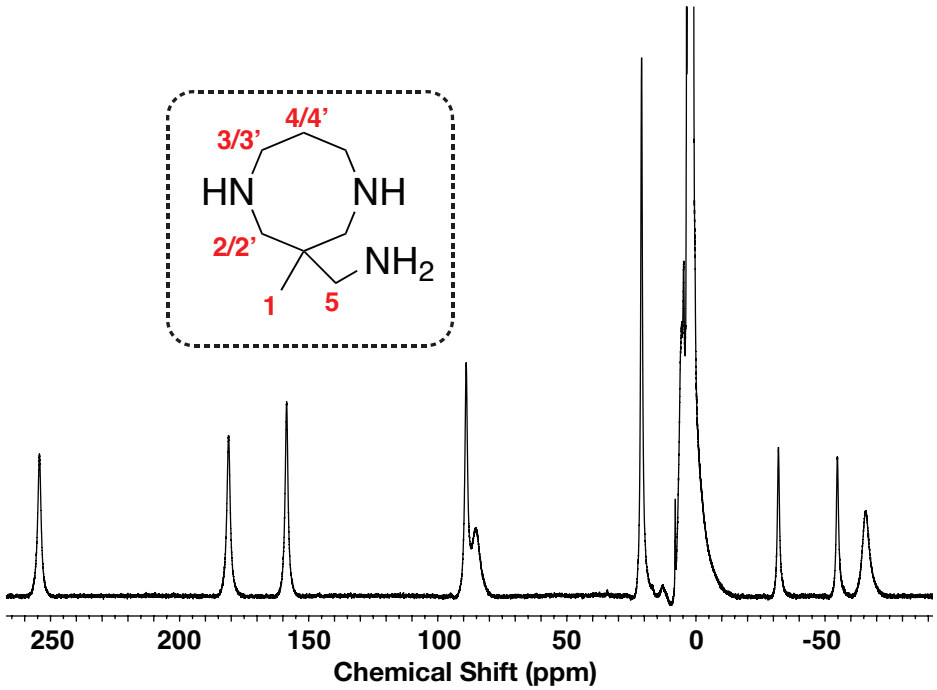

Figure 3.4: A Paramagnetically shifted ^{1}H NMR spectrum of the reaction product from Scheme 3.1 (**24**/**25**). CD_3CN 400 MHz. The inset indicates the expected number of distinct proton environments in the supporting ligand.

structure of the ligand (**22**) is shown in the inset of Figure 3.4. We would expect to observe resonances for each of the proton environments indicated in Figure 3.4, giving a total of eight expected aliphatic signals. In addition, we may expect to see a further two resonances from the N-H and NH_2 protons. Ten discrete signals were observed in Figure 3.4, which indicated the presence of ten unequivalent proton environments in the reaction product. This is consistent with the expected number of signals for the desired reaction product. Furthermore, the correct number of signals suggests the presence of a single species in solution.

Our efforts to further characterise **24** by fourier transform infrared (FT-IR) or electrospray ionisation mass spectrometry (ESI-MS) were significantly hampered by the sensitivity of the complex to O_2. Samples prepared for both FT-IR and ESI-MS changed colour before analysis was carried out, which suggested that the product had been oxidised. Fortunately however, we were able to obtain single crystals suitable for X-ray diffraction. Pale yellow, block-like single crystals of **24**/**25** were grown by layering an

Table 3.1: Selected bond lengths, angles and interatomic distances for **24** and **25**

	24	**25**
Fe1-N1 / Å	2.1355(12)	-
Fe1-N2 / Å	2.1388(12)	-
Fe1-N3 / Å	2.2476(12)	-
Fe2-N1′ / Å	-	2.1537(13)
Fe2-N2′ / Å	-	2.1953(11)
Fe2-N3′ / Å	-	2.2335(12)
N1-N2 Distance / Å	2.79	2.78
Mean N-N3 Distance / Å	3.07	3.07
Fold Angle / °	112.8	111.5
Fe-NNN Plane Distance / Å	1.82	1.83
Fe-Fe Distance / Å	-	3.72

acetonitrile (MeCN) solution of the reaction product from Scheme 3.1 with diethyl ether (Et_2O). This product was found to crystalise in the monoclinic space group $P2_1/c$. The resulting X-ray structures are shown in Figure 3.5. Selected bond lengths, angles and interatomic distances are shown in Table 3.1. Crystal data and refinement parameters are given in Table 3.5 in the experimental section of this chapter.

The asymmetric unit was found to consist of two neutral fragments. Figure 3.5a shows the monomeric fragment which consists of a mononuclear Fe^{II} centre ligated by **2** in a

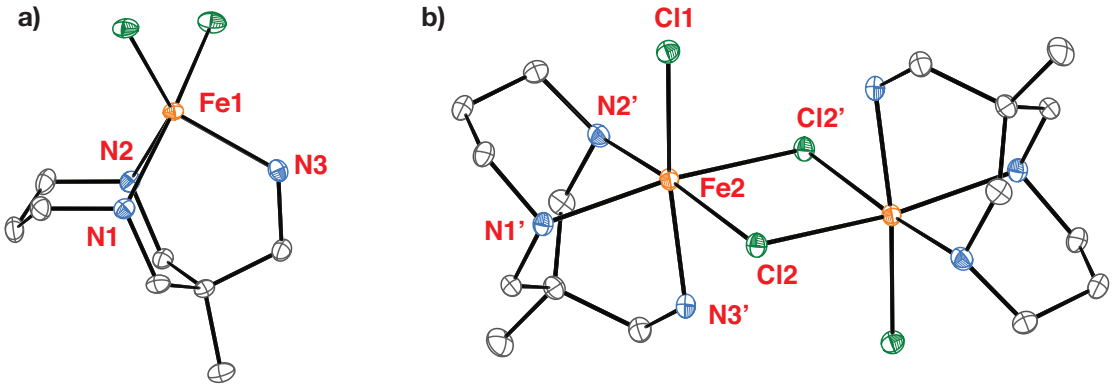

Figure 3.5: Thermal ellipsoid plots of **24**/**25**. a) Shows the monomeric fragment observed in the unit cell. b) Shows the μ_2-chloro bridged dimeric unit observed in the unit cell. Ellipsoids are shown at the 50% probability level. Hydrogen atoms have been omitted for clarity.

tridentate fashion. The coordination sphere of the metal atom is completed by two axial chloride ligands, resulting in a 5 coordinate iron centre. The coordination geometry of the metal centre was evaluated using the τ geometry index.[204] In the case of 5 coordinate complexes, the metal can either be trigonal bipyramidal (τ_5 = 1) or square pyramidal (τ_5 = 0). For **24**, it was calculated that τ_5 = 0.25. This suggested that the metal centre in **24** was in a distorted square pyramidal geometry.[204] The mean Fe-N distance in **24** is 2.17 Å, which is shorter than that previously reported for the similar 1,4,7-triisopropyl-1,4,7-triazcyclononane (^{iPr_3}TACN) complex [Fe^{II}(^{iPr_3}TACN)Cl_2] complex (2.26 Å).[205] Furthermore, the metal atom in **24** was shown to sit 1.82 Å out of the plane of the nitrogen atoms compared to 1.71 Å in [Fe^{II}(^{iPr_3}TACN)Cl_2]. This is a result of the relatively short and N1-N2 distance (2.79 Å) enforced by the rigidity of the DACO ring, which forces the metal atom out of the plane in order to accommodate the Fe-N bonds.

Figure 3.5b shows the dimeric fragment which consisted of two distorted octahedral Fe^{II} centres. The metal centres are bridged by two chlorides. The coordination sphere of the iron atom is completed by the tridentate **2** and an additional axial chloride ligand. The two triamine ligands (**2**) are symmetry equivalent, related through an inversion centre at the bridging chlorides. A similar diiron core has been reported for a diiron 1,4,8-triazacycloundecane (TACUD) complex, [$(Fe)_2$(TACUD)$_2$(μ−Cl)$_2$$Cl_2$].[206] The mean Fe-N bond distance in **25** is 2.19 Å and is similar to that reported in the TACUD complex (2.21Å). The distances are typical of high spin Fe^{II} bound to nitrogen. The metal atom in **25** sits 1.83 Å out of the nitrogen plane and is similar to that observed for **24** as well as the previously reported TACUD complex (1.88 Å). The mean Fe2-Cl2/Cl2′ bond length was found to be 0.08 Å longer than would be expected, when compared to previously reported values.[206] We attributed this to the higher steric bulk of **2** forcing the metal centres apart and consequently, increasing the bond length. The C-N-C fold angle of the DACO ring is similar to those previously reported for complexes containing the DACO moiety. Furthermore, the C-N-C fold angles found in **24** and **25** is similar to those observed in the structures of the unbound **20**, [**4**·H](PF_6) and [**4**·2H](($OTf)_2$). This suggests that the binding of the metal does not cause significant strain to the ligand framework. Obtaining this crystal structure was an important step as it demonstrated

that the ligand backbone is capable of binding metals in a tripodal manner. However, it also showed that **2** lacks the steric bulk to prevent the formation of dinuclear complexes.

The fact that two products, **24** and **25** were obtained in the solid state raised the question of which of these species is persistent in solution. The spectrum obtained (Figure 3.4) displayed sharp peaks and a low number of signals which suggested that either only one of the monomer or dimer is present or alternatively, they are exchanging faster than the NMR time-scale and the signals observed were an average of the two. The Fe^{II}, d^6, square pyramidal monomer would most likely posses a high spin $S = 1$ iron centre. This is based on the distribution of the 6 *d*-electrons into *d*-orbitals within a square pyramidal ligand field resulting in two unpaired electrons. Previously isolated square pyramidal Fe^{II} complexes with a similar N_3Cl_2 donor set have displayed the same $S = 1$ ground state.[207] Therefore, we would expect **24** to give a paramagnetically shifted ^{1}HNMR spectrum, like that observed in Figure 3.4. The dimeric unit on the other hand will possess two $S = 2$ centres, based on the distribution of the 6 *d*- electrons into the *d*-orbitals in an octahedral ligand field. These centres could either be coupled antiferromagnetically, resulting in an overall spin state of zero, or ferromagnetically to give a non-zero spin state. The observation of a paramagnetically shifted ^{1}H NMR spectrum suggests the absence of any strong antiferromagnetic interactions at room temperature. This is in agreement with the literature reports of similar diiron cores suggest that these centres are weakly ferromagnetically coupled, which would give rise to a paramagnetically shifted ^{1}H NMR spectrum. Therefore, based on the NMR data presented here it is not possible to conclude which of these species is present in solution. Interestingly however, Chavez and co-workers reported that the $[(Fe)_2(TACUD)_2(\mu{-}Cl)_2Cl_2]$ dimer was not stable in polar or coordinating solvents. Instead, under these conditions, the formation of a mononuclear species was observed. As the ^{1}H NMR spectrum shown in Figure 3.4 was collected in CD_3CN, which is both polar and coordinating, and the spectrum was indicative of the presence of only one species it is probable that this was the monomeric, **24**.

3.2.2 Nickel(II) Complexes of 2.

We next attempted the reaction of **2** with [$Ni(OAc)_2$]. We chose to carry out this reaction with [$Ni(OAc)_2$] rather than [$NiCl_2$] owing to its superior solubility in THF. We reacted a solution of **2** in THF with a pale green suspension of $Ni(OAc)_2$ in THF. Upon stirring, the solution gradually turned dark blue, accompanied by the dissolution of the sparingly soluble nickel salt. This indicated that a reaction had taken place. After stirring for 1 hour, addition of a large excess of anhydrous diethyl ether caused the formation of a blue precipitate. The nominal mass ESI-MS showed a dominant peak at m/z = 274 with an isotopic pattern corresponding to that expected for nickel. We have assigned this as $[Ni(\mathbf{2})(OAc)]^+$ (expected m/z = 274). None of the other minor peaks in the spectrum could be reasonably assigned to other structures containing Nickel as the isotopic pattern did not match that which would be expected.

The ^1H NMR spectrum of **26** is shown in Figure 3.6. In general, relatively sharp and well resolved paramagnetically shifted ^1H NMR signals are only observed for high-spin *pseudo*-tetrahedral or square pyramidal complexes of Ni^{II}. In the case of octahedral complexes, the observed resonances are usually significantly broadened in comparison.[203] Given that **22** formed a square pyramidal complex with Fe (**24**), this data suggested that a square pyramidal Ni^{II} complex was most likely persistent in solution. A total of eight discrete signals were observed in the spectrum. We assign these as resulting from the eight expected aliphatic resonances of the ligand, **2**, indicated in Figure 3.6. Therefore, the spectrum shown in Figure 3.6 corroborates the structure proposed of **26** from ESI-MS.

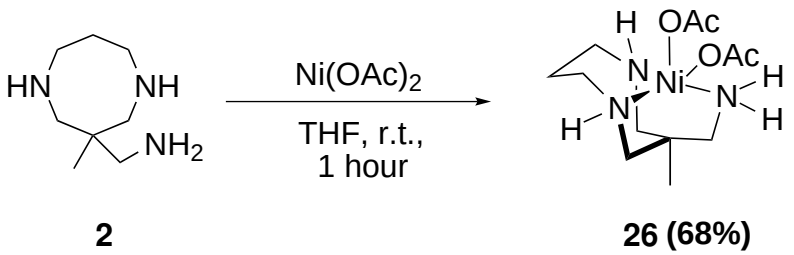

2 **26 (68%)**

Scheme 3.2: Synthesis of the nickel(II) complex, **26**.

We next attempted to grow single crystals of **26**. The blue precipitate obtained from the reaction shown in Scheme 3.2 was dissolved in acetonitrile. Diethyl ether was then allowed to slowly diffuse into this solution. This resulted in the formation of blue block-like single crystals. Curiously, X-ray analysis showed that these crystals consisted of a nickel cubane type structure, shown in Figure 3.7, rather than the monomer proposed on the basis of ESI-MS and ^{1}H NMR spectrum. The nickel cubane **27** was found to crystallise in the tetragonal space group $I4_1/a$. Selected bond lengths and inter atomic distances are shown in Table 3.2. Crystal data and refinement parameters are given in Table 3.5 in the experimental section of this chapter. The structure obtained form single crystal X-ray analysis has the general formula $[Ni_4(\mathbf{2})_4(\mu_3{-}OH)_4](OAc)_2$. Each of the nickel atoms is coordinated by one molecule of **2** which caps one face of the octahedron while three μ_3-hydroxide ligands complete the coordination sphere, resulting in an octahedral Ni^{II} centre (Figure 3.7a). These nickel centres were assembled into a tetra nickel cubane structure Figure 3.7b. Several examples of μ_3-hydroxide nickel cubane

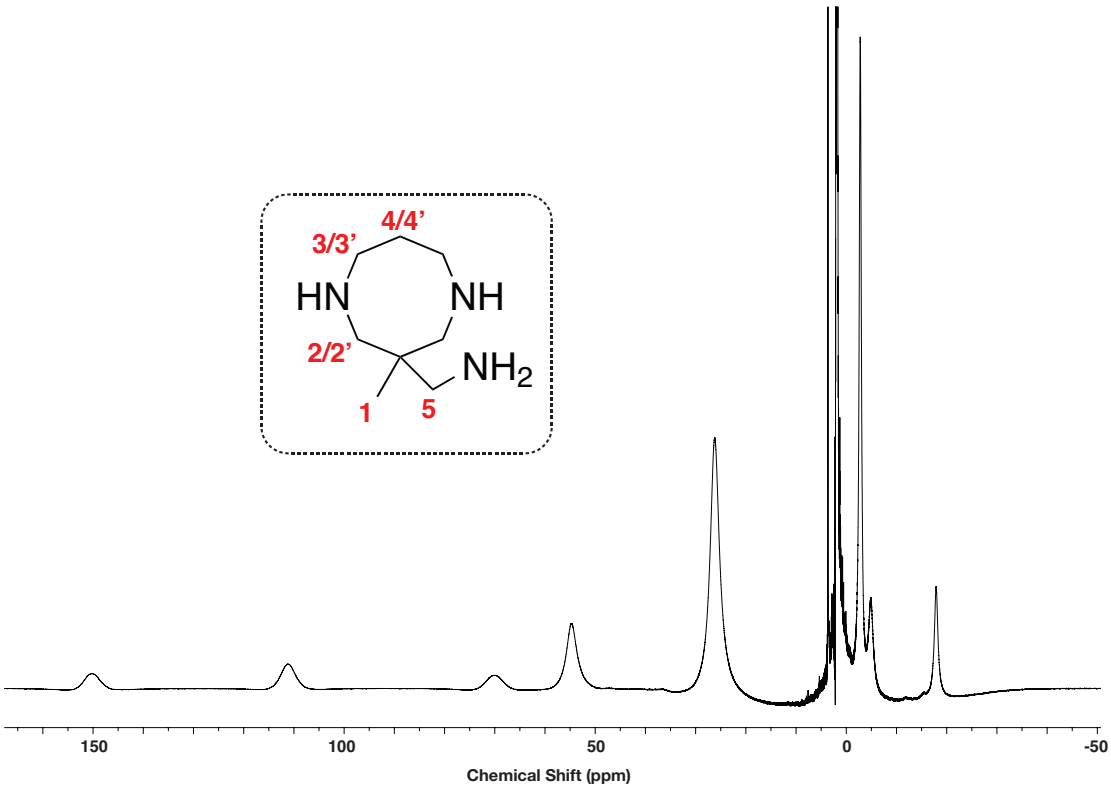

Figure 3.6: A Paramagnetically shifted ^{1}H NMR spectrum of **26**. CD_3CN 400 MHz. The inset indicates the number of unique proton environments in the supporting ligand.

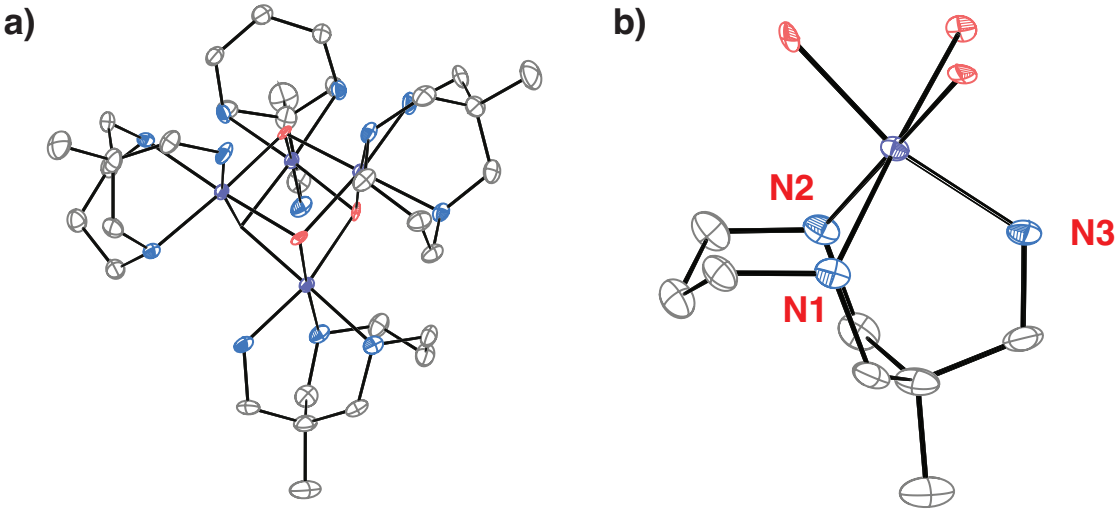

Figure 3.7: Thermal ellipsoid plot of the nickel complex **27**. a) Shows the μ_3-hydroxo tetra nickel cubane structure. b) Shows the octahedral nickel centre which forms the nickel cubane. Ellipsoids are shown at the 50% probability level. Hydrogen atoms and counter anions have been omitted for clarity.

structures have previously been reported in the literature.[208–210] **27** represented a rare example in which the nickel centres were not bridged by the organic ligand; only one other example of which has previously been reported.[211] The mean Ni-N bond length, 2.13 Å, is comparable to that of similar previously reported structures and is normal compared with the value expected for nitrogen bound to Ni^{II}. Similarly, the mean Ni-O bond length (2.08 Å) is in close agreement with those previously reported.[211] The Ni1-N1 and Ni1-N2 bond lengths (Table 3.2), are markedly longer than those observed in previously reported complexes of unalkylated DACO with Ni^{II} *e.g.* $[Ni^{II}(DACO)_2](ClO_4)_2$ (~1.97 Å). However, this is likely a result of the fact

Table 3.2: Selected bond lengths and interatomic distances for **27**

	27
Ni1-N1 / Å	2.080(4)
Ni1-N2 / Å	2.145(4)
Ni1-N3 / Å	2.164(4)
N1-N2 / Å	2.75
Fold Angle / °	110.2
Ni-NNN Plane Distance / Å	1.76

that $[Ni^{II}(DACO)_2](ClO_4)_2$ was square planar whereas **27** is octahedral. This results in longer metal-ligand bonds in the octahedral complex owing to the presence of more unfavourable steric and electronic interactions due to the greater number of ligands. The N1-N2 distance measured in **27** falls within the range of values which have been previously reported for $[Ni^{II}(DACO)_2](ClO_4)_2$ complexes and is comparable to that observed for **24** and **25**.[156] Similarly, the C-N-C fold angle is similar to those previously discussed. This again highlights the rigidity of the DACO ring. However, the nickel atom in **27** sits 1.76 Å out of the plane of the nitrogen atoms, which is considerably shorter than observed for **24** or **25**. This suggests that while the DACO ring itself is rigid, the remainder of the ligand architecture is slightly flexible.

Given that the ^{1}H NMR spectrum (Figure 3.6) suggested that the species observed in the spectra was not octahedral, given that relatively sharp paramagnetically shifted ^{1}H NMR signals were observed, and that ESI-MS data gave no indication for the presence of **27**, the acquisition of the crystal structure in which the nickel atoms were all in an octahedral coordination environment (Figure 3.7) was rather curious. Analysis of the samples using FT-IR suggested that this transformation had occurred during the recrystallisation process. Figure 3.8a and Figure 3.8b show the FT-IR spectra of **2** and $[Ni(OAc)_2]$ respectively. The $[Ni(OAc)_2]$ spectrum was assigned in conjunction

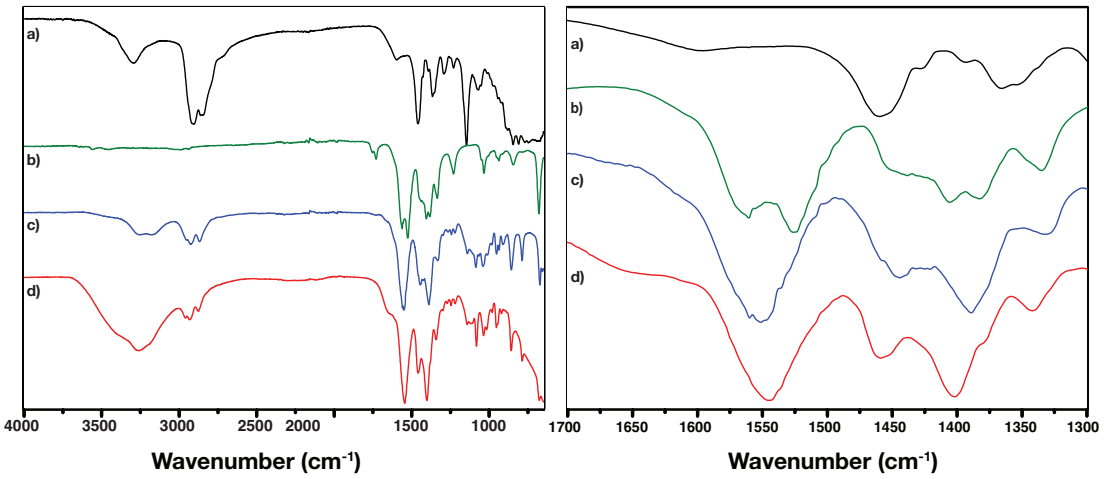

Figure 3.8: FT-IR Spectra of **26** and related compounds. Left: full spectrum. Right: Expansion of the acetate vibrations region. a) FT-IR spectrum of **2**; b) FT-IR spectrum of $Ni(OAc)_2$; c) FT-IR spectrum of **26**; d) FT-IR spectrum of **27**.

with the previously reported literature values. Vibrations at 1526 cm^{-1} ($\nu_{Asymm}COO^-$) and 1394 cm^{-1} ($\nu_{Symm}COO^-$) were clearly identifiable. Figure 3.8c shows the FT-IR of **26**. Importantly, bands for $\nu_{Asymm}COO^-$ (1551 cm^{-1}) and $\nu_{Symm}COO^-$ (1389 cm^{-1}) were both present and had shifted from those observed for $[Ni(OAc)_2]$. Furthermore, the large difference between $\nu_{Asymm}COO^-$ and $\nu_{Symm}COO^-$ (162 cm^{-1}) was indicative of the acetate ligand biding in an end-on manner, as proposed in Scheme 3.2. The FT-IR spectrum of **27** is shown in Figure 3.8d. Notably, a broad hydroxide vibration at $\sim$3250 cm^{-1} was observed which we ascribed to the presence of the μ_3-OH groups in **27**. Importantly, this band was not observed in Figure 3.8c. Furthermore, $\nu_{Asymm}COO^-$ (1544 cm^{-1}) and $\nu_{Symm}COO^-$ (1402 cm^{-1}) were both observed to shift compared to **26**. This suggests that there are structural differences between complexes **26** and **27**. These subtle yet important differences between Figure 3.8c and Figure 3.8d suggested that the transformation from the mononuclear **26** to the tetranuclear **27** *via* the inclusion of μ_3-OH bridges had occurred during the recrystallisation process. We have attributed this to the presence of adventitious water. Thus, the FT-IR data (Figure 3.8) shows that the crystal structure obtained for **27** does not contradict our assignment of the ^1H NMR spectrum and ESI-MS data in the formulation of **26**. However, further studies are required in order to confirm the identity of **26**.

3.2.3 Copper Complexes of 2.

After our success in synthesising the iron and nickel complexes discussed above, we next attempted to react **2** with salts of copper. Owing to its d^{10} configuration,

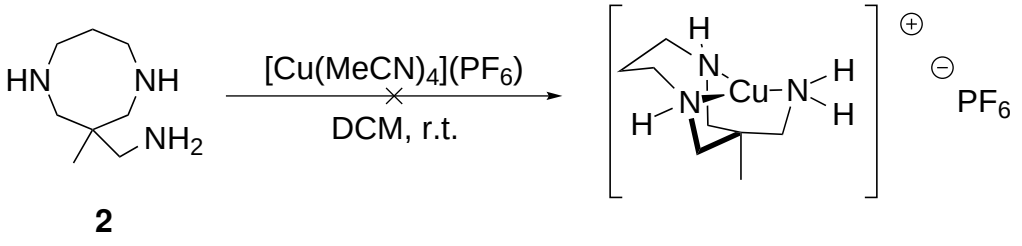

2

Scheme 3.3: The failed synthesis of Cu^I complexes of **2**. This reaction was found to lead to the disproportionation of Cu^I.

Cu^{I} generally has a preference for forming tetrahedral complexes.[212] Therefore, we attempted the reaction of **2** with $[Cu^{I}(MeCN)_4](PF_6)$. A solution of **2** in dichloromethane (DCM) was added to a suspension of $[Cu^{I}(MeCN)_4](PF_6)$, also in DCM. Upon mixing, the colour of the solution gradually became deep blue and a dark red precipitate began to adhere to the sides of the reaction vessel. We believe that this is a result of the disproportionation of the Cu^{I} starting material into Cu^{0} and unidentified Cu^{II} products. Similar observations have previously been made by Tolman and co-workers.[213] Disappointingly, the same outcome was observed regardless of the $[Cu^{I}X]$ starting material employed (X = Cl^-, I^-, 1,1,1-trifluoromethane sulphonate (OTf)).

As the results discussed above suggested that **2** was not capable of stabilising the Cu^{I} oxidation state, we next examined its reactivity towards Cu^{II} salts. A colourless solution of **2** in DCM was mixed with a DCM suspension of $[Cu(OAc)_2]$. An immediate colour change to deep blue was observed, suggesting complexation had occurred. Addition of a large excess of diethyl ether resulted in the formation of a blue precipitate. Nominal mass ESI-MS analysis of this precipitate gave a peak at *m/z* = 279 with an isotopic pattern expected of copper. We assigned this peak as corresponding to $[Cu(\mathbf{2})(OAc)]^+$ (expected *m/z* = 279). In an attempt to grow single crystals of this product, the remainder of the sample was dissolved in DCM and layered with Et_2O. Needle like single crystals grew over the period of one week and were analysed by X-ray diffraction. Surprisingly, the structure obtained did not correspond to that predicted by ESI-MS. The crystallographically determined structure is shown in Figure 3.9. Analysis of this structure revealed a five-coordinate copper centre, ligated by two organic moieties. In the first of these, three nitrogen atoms N1, N2 and N3 all form part of one molecule of **2**, which binds the metal in a tridentate fashion (Figure 3.9a), as has been shown in

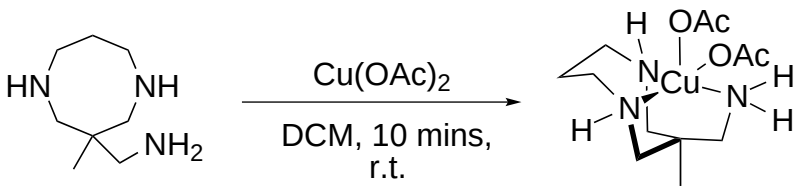

2 **28 (72%)**

Scheme 3.4: The synthesis of a Cu^{II} complex of **2**.

the complexes of iron (**24**/**25**) and nickel (**27**) discussed above. However, the second organic moiety is a modified analogue of **2**, where two adjacent nitrogen atoms (N5 and N6) have been connected by a methylene linker, forming an aminal (Figure 3.9b). Consequently, this second ligand is bound in a bidentate manner, through only one of the nitrogens belonging to the DACO ring (N4) as well the formerly *exo*-cyclic nitrogen, N6, which is now part of a six-membered ring. Closer inspection of the crystal structure revealed that while the initial reaction was carried out using $[Cu(OAc)_2]$, the +2 charge in **29** was balanced by two chloride anions. This suggests that the origin of the newly installed aminal group was most likely the solvent, DCM. Importantly, no peaks with *m/z* that could be attributed to **29** were found in the ESI-MS. While there is literature precedent for the reaction of DCM with amines to give aminals, it has been shown that these reactions are generally slow therefore, do not require consideration when employing DCM as a solvent to be used with amines.[214] However, in this instance the rate of the reaction may be significantly increased due to hydrogen bonding between the hydrogen atoms from the amino groups of the DACO moiety and the chloride leaving groups from DCM. This has been demonstrated to have a marked effect on

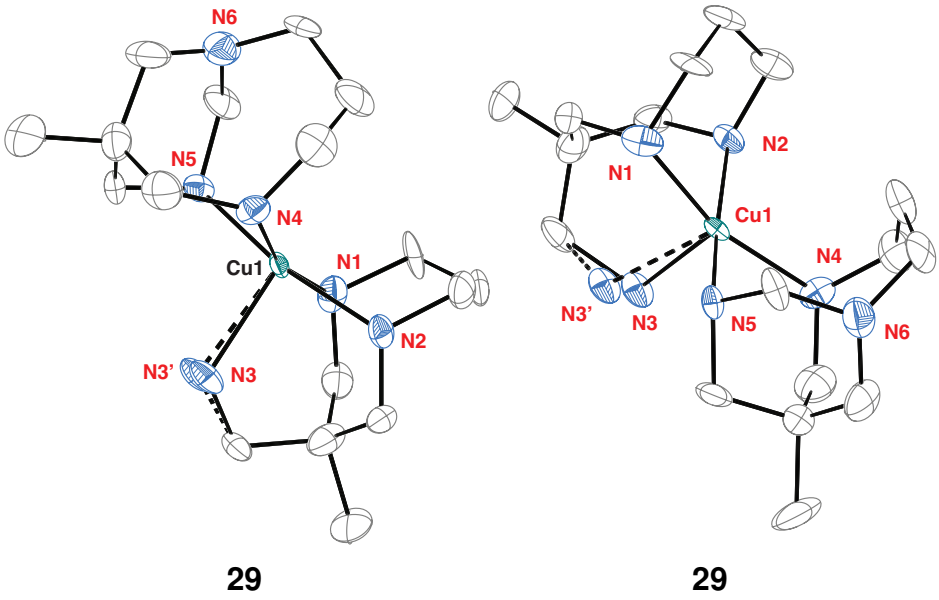

Figure 3.9: Thermal ellipsoid plot of **29**. a) Illustrates the tridentate binding mode of **2**. b) Highlights the aminal formation between N5 and N6. Ellipsoids are shown at the 50% probability level. Hydrogen atoms have been removed for clarity.

Table 3.3: Selected bond lengths and interatomic distances for **29**

	29
Cu1-N1 / Å	2.067(4)
Cu1-N2 / Å	2.038(4)
Cu1-N3 / Å	2.209(10)
Cu1-N3' / Å	2.199(11)
Cu1-N4 / Å	2.043(4)
Cu1-N5 / Å	2.039(4)
Cu1-N6 / Å	2.067(4)
N1-N2 / Å	2.71
Fold Angle / °	111.076
Cu-NNN Plane Distance / Å	1.85

the rate of fixation of DCM by macrocyclic amines in the Menshutskin reaction.[215] Importantly, this also supported our hypothesis that aminal formation was responsible for the failure of the Eschweiler-Clarke methylation reactions in 2.2.3 as it demonstrated the feasibility of this intramolecular reaction.

Despite the fact that this side reaction had occurred, **29** still presented a useful example to examine the coordination chemistry of **2**. **29** crystallised in the monoclinic space group C_2/c. Selected bond lengths and distances are shown in Table 3.3. Crystal data and refinement parameters are given in Table 3.5 in the experimental section of this chapter. The *exo*-cyclic amino group (N3 and N3') was found to be split in two positions equally. The copper centre was shown to be five coordinate, and square pyramidal (τ_5 = 0.02) with the metal atom found to sit approximately 1.85 Å out of the plane of the nitrogen atoms, similar to the iron complexes discussed above. The Cu1-N bonds to all N atoms except N3/N3' show bond lengths expected for nitrogen atoms bound to Cu^{II} ($\sim$ 2.0Å).[216,157] The Cu1-N3/N3' bonds are elongated ($\sim$ 2.2Å) due to a Jahn-Teller distortion, as this nitrogen atom binds in the axial position of the square pyramid. The formation of the aminal in Figure 3.9 clearly illustrated that DCM was a poor choice of solvent for recrystallising **28**. Therefore, we recrystallised the precipitate obtained from the reaction shown in Figure 3.9 in MeCN/Et_2O. Single crystals were obtained and analysed by X-ray diffraction. Unfortunately, the data collected was indicative of heavy twinning within the crystal lattice and no satisfactory solution could be found.

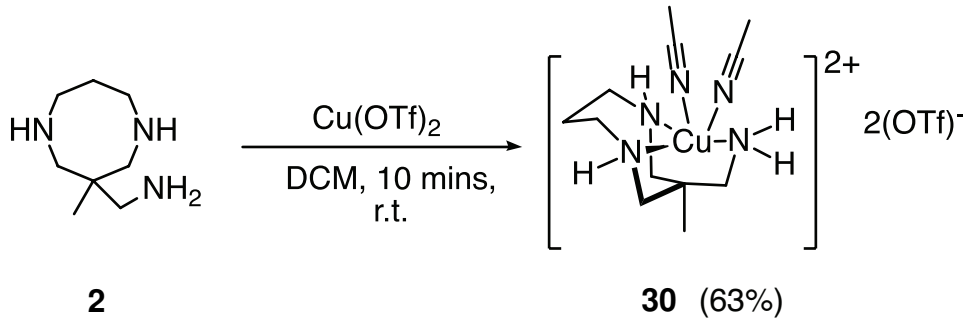

2 **30** (63%)

Scheme 3.5: Synthesis of **30**; a Cu^{II} complex **2**.

Consequently, we attempted the recrystallisation process utilising both co-solvents and entirely different solvent systems in order to circumvent this issue however, no single crystal growth resulted from these experiments. As a result of this, we repeated the experiment with a different Cu^{II} salt, [$Cu(OTf)_2$] (Scheme 3.5). A colourless solution of **2** in DCM was mixed with a DCM suspension of $Cu(OTf)_2$. An immediate colour change to deep blue was observed. Addition of a large excess of Et_2O caused the precipitation of a blue solid. This solid was recrystallised by layering a MeCN solution of the precipitate with Et_2O. Gratifyingly, we were able to obtain single crystals suitable for X-ray analysis. Unfortunately, we encountered difficulties in mounting the crystals.

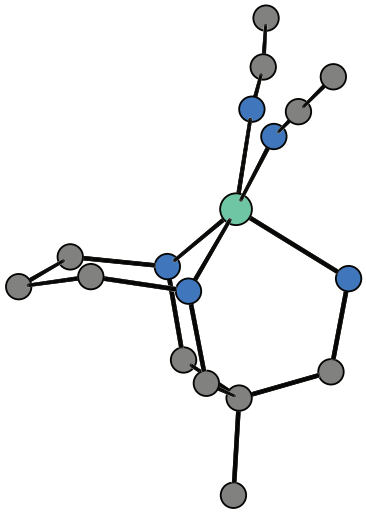

30

Figure 3.10: Connectivity diagram for **30**, illustrating the coordination environment around the copper centre. Obtained *via* X-ray diffraction.

The morphology of the crystals appeared to visibly change after they were removed from the mother liquor. While we were able to collect a complete data set, the structure solution we obtained from this data was unsatisfactory. The reasons for this are as follows. A significant amount of disorder was observed in the triflate anions found in the asymmetric unit and consequently, they were modelled using a large number of constraints and restraints. Similarly, a twinned fragment of **30** was present in the asymmetric unit which also had to be modelled with a high number of constraints and restraints. This meant that the model resulting from refinement of the X-ray data could not be used to determine bond lengths or angles. Nevertheless, we were able to obtain the connectivity diagram for **30** shown in Figure 3.10. While the bond lengths and angles are unreliable, this data can be used to elucidate the coordination environment of the copper centre. Importantly, the diagram shown in Figure 3.10 indicated that the copper centre was five-coordinate and in approximate square pyramidal geometry. This is in line with the data was collected on other monometallic species (**24** and **29**) *vide supra*. In obtaining this structure, we demonstrated that isolation of a monometallic complex of **2** was a feasible target should appropriate reaction conditions be employed this included, avoiding the use of dichloromethane as a solvent, the complete exclusion of adventitious water and avoiding the use of potentially bridging ligands (*e.g.* OAc, Cl^- *etc.*). However, unfortunately to date we have yet to isolate such a mononuclear Cu^{II} species.

3.2.4 A Zinc Complex of Triamine 2.

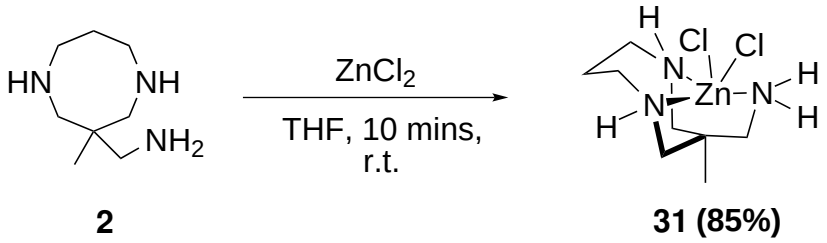

2 **31 (85%)**

Scheme 3.6: Synthesis of **31**, a Zn^{II} complex of **2**.

We next moved to investigate the synthesis of Zn^{II} complexes of **2**. We reasoned that

this would allow us the unique opportunity to investigate the coordination chemistry of this ligand using ^{1}H NMR as the d^{10} configuration renders these complexes diamagnetic. For comparison, the Fe^{II}, Ni^{II} and Cu^{II} complexes discussed above were all found to be paramagnetic.

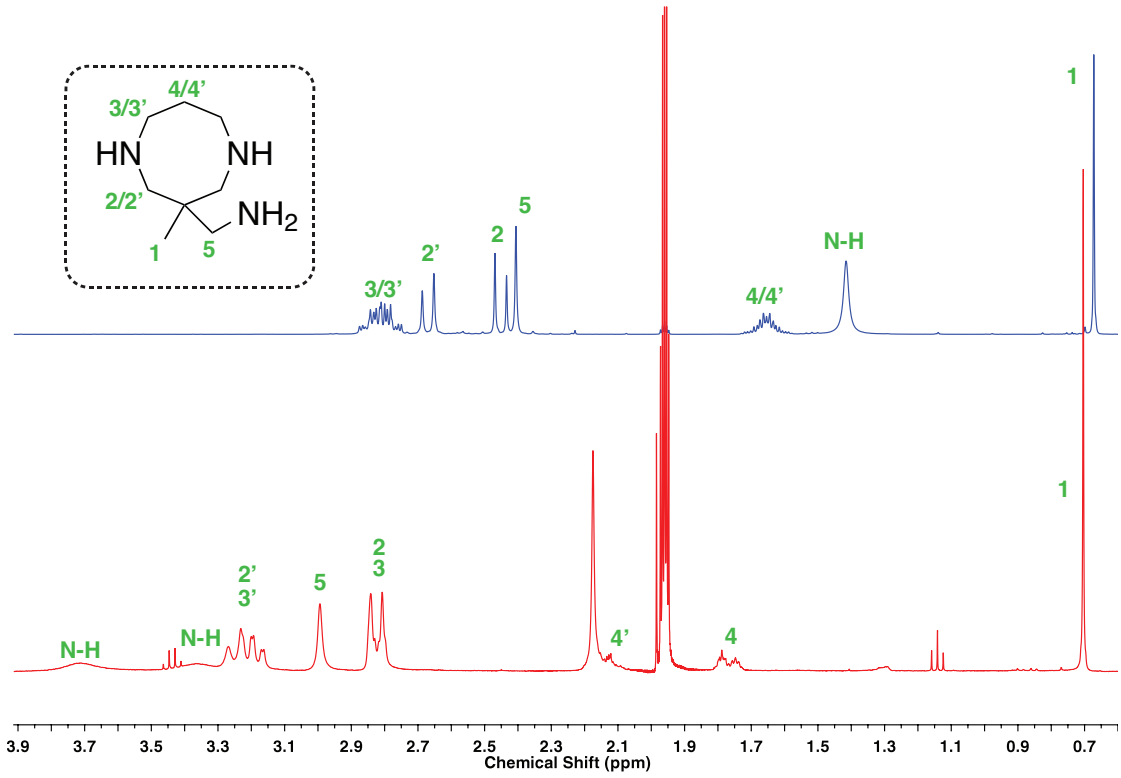

Figure 3.11: ^{1}H NMR spectrum of **31**. a) Shows the ^{1}H NMR spectrum of **2** (CD_3CN 400 MHz); b) a) Shows the ^{1}H NMR spectrum of **31** (CD_3CN 400 MHz).

Towards this goal, we reacted **2** with [$ZnCl_2$ in anhydrous THF. Addition of Et_2O afforded a white precipitate. The supernatant was decanted and the resulting powder dried under vacuum. Nominal mass ESI-MS showed a peak at m/z = 256 which we have assigned as $[Zn(\mathbf{2})Cl]^+$ (expected m/z = 256) which confirmed the identity of **31**. The ^{1}H NMR spectrum of the resulting precipitate (**31**) is shown in Figure 3.11b while the ^{1}H NMR spectrum of **2** is shown in Figure 3.11a. The resonances for both **2** and **31** were assigned in conjunction with their respective heteronuclear single quantum coherence (HSQC) and heteronuclear multiple-bond correlation (HMBC) spectra. Importantly, the resonances associated with the DACO ring in **31** were split into diastereotopic pairs, as was the case for [**4**·H](PF_6) and [**4**·2H](($OTf)_2$). Signals corresponding to $H_{2/2'}$, $H_{3/3'}$ and

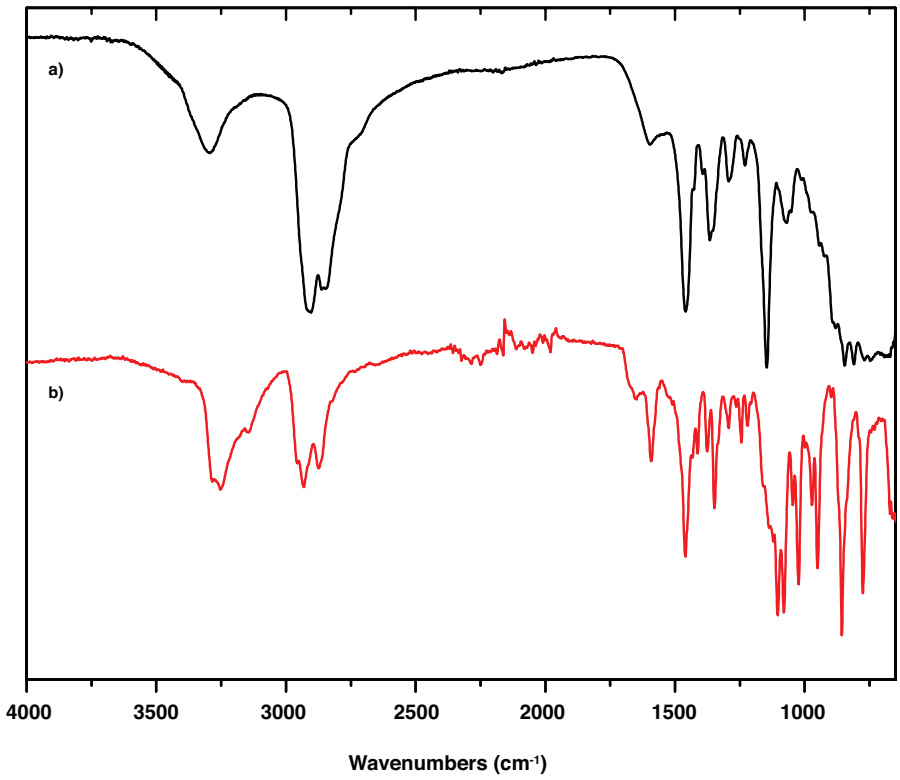

Figure 3.12: FT-IR spectrum of **31**. a) Shows the FT-IR spectrum of **2**; b) Shows the FT-IR spectrum of **31**. Assignments correspond to the structure shown in the inset.

$H_{4/4'}$ all showed pairs of signals corresponding to each of the diastereotopic protons. This result is indicative of complexation of zinc by the nitrogen atoms in the DACO ring. This significant difference in chemical shift for each proton of the diastereotopic pair is a result of inequivalent local magnetic anisotropy on each face of the ring, due to the presence of the metal atom. Furthermore, H_5 in **31** is shifted significantly downfield compared with the corresponding signal, while the *exo*-cyclic methyl signal, H_1 shifted only slightly. The signals associated with the N-H protons are also shifted significantly downfield. This is indicative of coordination of the nitrogen atoms as donation of the lone pairs to the metal results in deshielding of the associated proton signals. We suggest that **31** is most likely square pyramidal. This is based on the crystal structures of **24** and **29**, the connectivity diagram for **30**, as well as previously reported structures of TAME derivatives with $ZnCl_2$ which have all displayed this geometry.[174] Importantly, this diamagnetic NMR data corroborates the assignment paramagnetically shifted ^1H resonances reported for **24**/**25** and **26** in Figure 3.4 and Figure 3.6 respectively, as it

confirmed that eight C-H signals are expected from the aliphatic skeleton of **2** when coordinated to a metal. This was the number of signals observed in the ^{1}H NMR spectra of **24/25** and **26**. We also investigated the conformational flexibility of **31** using selective nuclear Overhauser effect (NOE) NMR experiments. Irradiating the multiplet at 1.76 ppm corresponding to H_4 showed through space coupling only to its diastereotopic counterpart $H_{4'}$ and the geminal $H_{3/3'}$. This is in stark contrast to **2**, in which $H_{4/4'}$ showed through space coupling to all of the other protons within the molecule. This strongly suggests that complexation of zinc by **2** significantly reduces the conformational flexibility of the DACO ring.

The FT-IR spectrum of **31** is shown in Figure 3.12 and is also highly indicative of complex formation. Notably, the amine stretching frequencies at 3253 and 2931 cm^{-1} in **31** (Figure 3.11b) show a significant reduction in intensity compared with the starting material, **2** (Figure 3.12b). This has been previously reported as being characteristic of amines binding to a metal centre and therefore suggests that the reaction (Scheme 3.6) leads to the formation of **31**.[174] The ESI-MS, ^{1}H NMR and FT-IR spectra reported above are all indicative of formation of a zinc complex of **2**. Unfortunately, to date, we have been unsuccessful in our attempts to grow single crystals of **31**.

3.3 Synthesis and Characterisation of a Copper(I) Complex of 4.

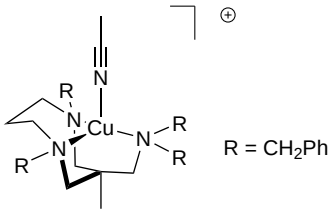

32

Figure 3.13: A chemdraw representation of **32**, which was only observed by ESI-MS.

As the X-ray structures of complexes containing **2** shown above suggested, while **2** could bind metals in a facially capping manner, the steric bulk associated with the amine donor atoms was insufficient to either prevent bridging between metal centres or promote the formation of low coordinate, *pseudo*-tetrahedral complexes. Consequently, we moved on to examine the reactivity of the tetraalkylated **4**.

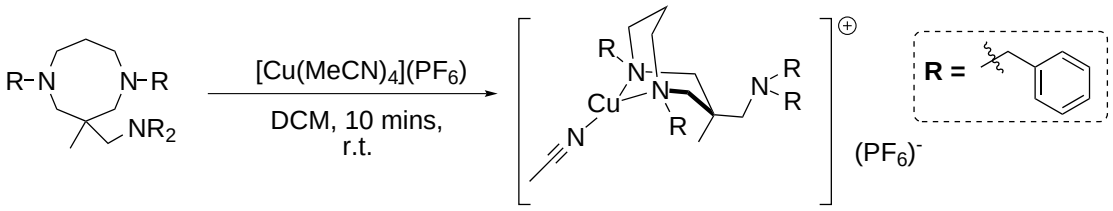

4 **33** **(65%)**

Scheme 3.7: Synthesis of **33**.

The alkylated triamine **4** was reacted with $[Cu^{I}(MeCN)_4](OTf)$ in anhydrous MeCN. Upon addition of a solution of **4** to the copper salt an immediate colour change from colourless to yellow was observed. ESI-MS analysis of an aliquot of this reaction mixture indicated a peak at *m/z* = 621 with an isotopic pattern typical of copper, which we assigned as $[Cu^{I}(\mathbf{4})(MeCN)]^{+}$ (expected *m/z* = 621) (Figure 3.13C). Encouragingly, no 2:1 (ligand:metal) species were observed in the ESI-MS spectra. Taken in conjunction with the X-ray structures determined for **2**, these observations suggested that **4** bound

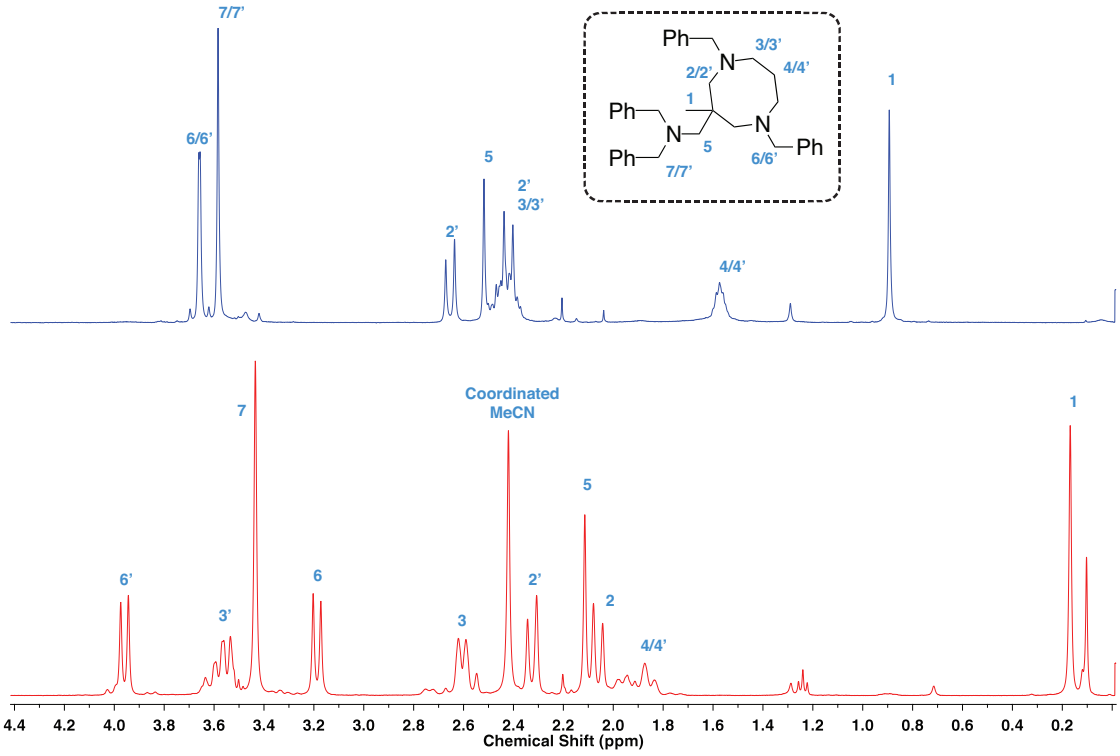

Figure 3.14: ^{1}H NMR spectrum of **33**. a) Shows the ^{1}H NMR spectrum of **4**; b) Shows the ^{1}H NMR spectrum of **33**. $CDCl_3$ 400 MHz.

the metal centre as a tripod yielding a four-coordinate complex. Unfortunately, work-up of this reaction mixture did not yield the desired complex.

Consequently, the same reaction was repeated utilising DCM as the reaction solvent (MeCN was eliminated from the reaction as we suspect the complex is unstable in MeCN). Figure 3.14 shows the ^{1}H NMR spectrum of the yellow solid obtained from the DCM reaction mixture. The new material displayed resonances distinct from those of **4**, [**4**·H](PF_6) and [**4**·2H](($OTf)_2$), which suggested that complexation of Cu^{I} by **4** had occurred. The signal assignments shown in Figure 3.14 were made in combination with HSQC spectra. This confirmed that the signals associated with the DACO ring in **33** had split into diastereotopic pairs. Encouragingly, this splitting paralleled that observed in the spectrum of **31** (Figure 3.11) as well as the protonated species [**4**·H](PF_6) and [**4**·2H](($OTf)_2$) (Figure 2.10). Notably, a resonance at 2.42 ppm (corresponding to 3 protons) was observed. We assigned this to a coordinated MeCN ligand (uncoordinated MeCN = 2.01 ppm). This assignment was confirmed by the presence of a high-

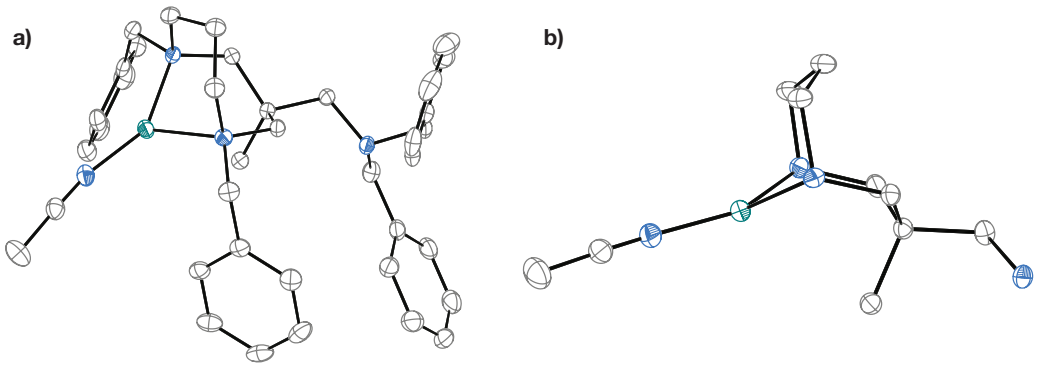

33

Figure 3.15: Thermal ellipsoid plot of **33** a) Shows the complete cationic fragment; b) Shows the cationic fragment with the *N*-benzyl groups removed for clarity. Ellipsoids are shown at the 50% probability level. Hydrogen atoms and counter anions have been omitted for clarity.

field signal at 2.9 ppm in the ^{13}C NMR spectrum, typical of a nitrile methyl group. Integration of the resonances in Figure 3.14 showed a 1:1 ratio of **4** to MeCN. This suggested that **4** was bound in either a bidentate or a tridentate manner giving a coordination number of either three or four. This is further corroborated by our ESI-MS data that indicated the formation of $[Cu^{I}(NCCH_3)\mathbf{4}]^+$.

Single crystals of **33** were grown by diffusing Et_2O into a DCM solution of the precipitate. The resulting pale yellow, needle-like crystals were found to crystallise in the monoclinic space group $P2_1/c$ (Figure 3.15). Selected bond lengths, angles and interatomic distances are shown in Table 3.4. Crystal data and refinement parameters are given in Table 3.5 in the experimental section of this chapter. Notably, in **33**

Table 3.4: Selected bond lengths, angles and interatomic distances for **33**

	33
N1-Cu1 /Å	2.0108(15)
N2-Cu1 /Å	2.1193(15)
N4-Cu1 /Å	1.8540(16)
N1-N2 /Å	2.97
N1-Cu1-N2 /°	91.76(6)
N1-Cu1-N4 /°	149.49(6)
N2-Cu1-N4 /°	113.79(6)

(Figure 3.15) the copper centre is three coordinate and is in a distorted trigonal planar coordination environment. This structure was in agreement with the ^{1}H NMR and ESI-MS data discussed above. The resonances associated with the DACO ring in **33** are split as a result of coordination to the metal centre, irrespective of the fact that the *exo*-cyclic amine remains unbound. The relative 1:1 integration in the ^{1}H NMR spectrum between the methyl group of the MeCN ligand compared to the protons in **33** also correlates with the structure obtained of **33**. Similarly, the ESI-MS was indicative of $[Cu^{I}(\mathbf{4})(MeCN)]^{+}$. The N1/N2-Cu bond lengths (Figure 3.15) were found to be slightly shorter than those observed for the complexes of **2** but still in line with the values expected for tertiary amines bound to Cu^{I}.[159] The N-Cu1-N bond angles, given in Table 3.4, deviate significantly from the expected 120°. This is due to the mesocyclic nature of the DACO moiety restraining the N1-N2 distance and consequently the N1-Cu1-N2 bond angle. This angle is also significantly larger than those observed for the complexes of **2** discussed above. We ascribe this to the absence of ligand field stabilisation energy associated with the formation of d^{10} Cu^{I} complexes. In this instance, the geometry around the metal centre is purely dictated by sterics, thus the N1-Cu1-N2 angle is maximised to reduce steric clashes between the substituents on the nitrogen donor atoms. This is also likely a contributing factor to **4** binding in a bidentate mode, rather in the tridentate fashion observed for **2**. In addition, we reason that steric clashes between the bulky benzyl substituents in **2** prevent all three nitrogen atoms from binding the same metal centre.

Curiously, the structural parameters observed for **33** are almost identical to those observed for [**4**·H](PF_6). In both of these structures, the lone pairs of the nitrogen atoms are on the same face of the DACO ring as the methyl group. This results in the *exo*-cyclic amino group residing on the opposite face of the mesocycle. In this conformation, **4** can not bind metals in a tridentate manner, as we have observed for **2**. Since this has been observed in these two instances it is reasonable to assume that this is the preferred orientation of complexes **4** and is once again most likely a result of the steric clashes between the bulky benzyl substituents. Comparison of the ^{1}H NMR spectrum of **33** and [**4**·H](PF_6) with that of **34** reveals a potentially useful spectroscopic

characteristic of the different binding mode of the ligand skeleton. In the complexes bidentate complexes **33** and [**4**·H](PF$_6$) H$_1$ is shifted significantly upfield compared to the free ligand **4**. We reason that this is a result of the methyl group residing on the same face of the DACO ring as the metal/ proton therefore, there is a significant change in local magnetic anisotropy and consequently the chemical shift. By comparison, in **31** where the methyl group is on the opposite face of the ring to the metal, the difference in chemical shift of H$_1$ is negligible. Therefore, the difference in chemical shift of H$_1$ can be used to distinguish between bidentate binding of the ligand and tridentate binding of the ligand.

3.4 Conclusions and Future Work

In conclusion, we have described our preliminary studies into the coordination chemistry of the two 1,5-DACO based ligands, **2** and **4**, synthesised in Chapter 2. We have investigated the reactivity of **2** towards [$FeCl_2$], [$Ni(OAc)_2$], [$Cu(OAc)_2$], [$Cu(OTf)_2$] and [$ZnCl_2$]. The data we have presented for the Fe, Cu, and Zn complexes suggested that, in the absence of bridging ligands, **2** tends forms square pyramidal complexes. Importantly, we have observed no evidence by for the formation of octahedral complexes with the general formula $[M^n(\mathbf{2})_2]^{n+}$, as has been previously described for complexes of TAME.[202] This indicated that our modifications to the TAME framework have increased the steric demands around the metal binding pocket such that formation of six coordinate 2:1 complexes is unfavourable. However, as stated in Chapter 1, we require that our ligand forms *pseudo*-tetraheral complexes in order to stabilise late transition metal-oxos therefore, these results suggested that **2** required further modification. Similarly, in the case of the solid state structures of the binuclear iron complex **25** and the tetranuclear nickel cubane **27**, we have demonstrated that the metal centres readily react with bridging ligands such as chloride or hydroxide to form polymetallic species. Consequently, we investigated the effect of *N*-alkylation on the coordination behaviour of **2**. We have investigated the reactivity of **4** towards $[Cu^{I}(MeCN)_4](OTf)$ and $[Cu^{I}(MeCN)_4](PF_6)$. X-ray crystallography conclusively showed that the installation of benzyl groups lead to the formation of a trigonal planar complex. We have ascribed this to the fact that the bulky benzyl groups are unlikely to be able to be accommodated around the metal centre should **4** bind in a tridentate fashion.

The results outlined in this chapter paint an exciting picture for the future of this project. There is significant scope for investigating further the coordination chemistry of both **2** and **4**. With regards to **2**, future work should be focused on understanding the factors that affect the formation of bimetallic species like the dimeric iron complex **25**. It is also crucial that the reactivity of **4** towards metals other than Cu^{I} is examined in order to

elucidate the feasibility of **4** binding in a tridentate fashion.

3.5 Experimental Section

3.5.1 Materials and Methods

All reagents and solvents were purchased from commercial sources and used as received, unless otherwise stated. $Cu(OTf)_2$, $[Cu(MeCN)_4](PF_6)$ and $[Cu(MeCN)_4](OTf)$ were prepared using previously reported procedures.[217,218] THF and Et_2O were distilled from sodium and benzophenone and stored under argon. MeCN and DCM were distilled from CaH_2 prior to use.

$CDCl_3$ was dried and de-acidified by stirring and subsequently storing over 4 Å molecular sieves and basic alumina. ^1H and ^{13}C NMR spectra were recorded on either an Agilent 400-MR Long Hold Mag. Res. Spectrometer 2 or a Bruker Avance II 600 MHz spectrometer. ESI mass spectra were acquired by direct injection to a Micromass time of flight spectrometer (tof). Fourier-Transform Infra-red spectra were recorded using a Perkin-Elmer Spectrum I FT-IR spectrometer.

3.5.2 Synthesis of [Fe^{II}(2)Cl_2] (24/25)

Anhydrous $FeCl_2$ (32.2 mg, 0.25 mmol) was suspended in a schlenk charged with anhydrous THF (2 mL). Triamine **2** (40.1 mg, 0.25 mmol) was added to a separate schlenk, which was then purged with argon and charged with anhydrous THF (2 mL). This colourless solution was then transferred by syringe to the suspension of $FeCl_2$. The intense red/brown colour of the reaction mixture immediately began to fade. The reaction was stirred for 10 minutes. The remaining inorganic insolubles were then removed by cannula filtration to give a pale yellow solution. A large excess of anhydrous Et_2O (15 mL) was added to the THF solution, which was stirred for 10 minutes then allowed to settle. The supernatant was decanted and the remaining pale yellow solid (43 mg, 59%) dried under vacuum. Crystals suitable for X-ray diffraction were obtained by recrystallisation from MeCN/Et_2O.

^{1}H Paramagnetic NMR (400 MHz, CD_3CN) δ = -65.6, -54.6, -31.8, 5.4, 21.7, 85.7, 88.9, 159.2, 181.3, 254.9

3.5.3 Synthesis of $[Ni^{II}(2)(OAc)_2]$ (26)

Anhydrous $Ni(OAc)_2$ (69.7 mg, 0.39 mmol) was suspended in a schlenk charged with anhydrous THF (2 mL). Triamine **2** (62.1 mg, 0.39 mmol) was added to a separate schlenk, which was then purged with argon and charged with anhydrous THF (2 mL). This colourless solution was then transferred by syringe to the suspension of $Ni(OAc)_2$. The pale green colour of the reaction mixture gradually began to turn intense blue. The reaction was stirred for 1 hour. The remaining inorganic insolubles were then removed by cannula filtration to give a dark blue solution. A large excess of anhydrous Et_2O (15 mL) was added to the THF solution, which was stirred for 10 minutes then allowed to settle. The supernatant was decanted and the remaining pale yellow solid, **26**, (90 mg, 68%) dried under vacuum. Crystals of **27** suitable for X-ray diffraction were obtained by recrystallisation of **26** from $MeCN/Et_2O$.

^1H Paramagnetic NMR (400 MHz, CD_3CN) δ = -18.0, -5.3, -2.6, 26.7, 55.2, 70.1, 111.6, 150.5

ν_{max} /cm^{-1}: 3178, 2926, 1551, 1389, 1086, 1040, 953, 858, 788, 673, 617.

Nominal ESI-MS (*m/z* -ESI): Found: 274 (M^+. $C_{10}H_{22}O_2N_3Ni$ predicted mass: 274)

3.5.4 Attempted Synthesis of [Cu^{II}(2)$(OAc)_2$] (28) which yielded 29

Anhydrous $Cu(OAc)_2$ (47.7 mg, 0.26 mmol) was dissolved in a schlenk charged with anhydrous DCM (2 mL). Triamine **2** (41.3 mg, 0.26 mmol) was added to a separate schlenk, which was then purged with argon and charged with anhydrous DCM (2 mL). This colourless solution was then transferred by syringe to the solution of $Cu(OAc)_2$. The pale blue colour of the reaction mixture gradually began to turn intense blue. The reaction was stirred for 10 minutes. The remaining inorganic insolubles were then removed by cannula filtration to give a blue/green solution. A large excess of anhydrous Et_2O (15 mL) was added to the DCM solution, which was stirred for 10 minutes then allowed to settle. The supernatant was decanted and the remaining blue solid, **29** (64 mg, 72%) was dried under vacuum.

Nominal ESI-MS (*m/z* -ESI): Found: 279 (M^+. $C_{10}H_{22}O_2N_3Cu$ predicted mass: 2779)

Crystals of **29** suitable for X-ray diffraction were obtained by recrystallisation of **28** from DCM/Et_2O.

3.5.5 Synthesis of $[Cu^{II}(2)(OTf)_2]$ (30)

Anhydrous $Cu(OTf)_2$ (78.2 mg, 0.22 mmol) was dissolved in a schlenk charged with anhydrous DCM (2 mL). Triamine **2** (34.0 mg, 0.22 mmol) was added to a separate schlenk, which was then purged with argon and charged with anhydrous DCM (2 mL). This colourless solution was then transferred by syringe to the solution of $Cu(OTf)_2$. The green/blue colour of the reaction mixture gradually began to turn intense blue. The reaction was stirred for 10 minutes. The remaining inorganic insolubles were then removed by cannula filtration to give a blue solution. A large excess of anhydrous Et_2O (15 mL) was added to the DCM solution, which was stirred for 10 minutes then allowed to settle. The supernatant was decanted and the remaining blue solid, **30** (41 mg, 63%) was dried under vacuum.

Crystals of **30** suitable for X-ray diffraction were obtained by recrystallisation of from $MeCN/Et_2O$.

3.5.6 Synthesis of $[Zn^{II}(2)Cl_2]$ (31)

Anhydrous $ZnCl_2$ (47.7 mg, 0.35 mmol) was suspended in a schlenk charged with anhydrous THF (2 mL). Triamine **2** (55.0 mg, 0.35 mmol) was added to a separate schlenk, which was then purged with argon and charged with anhydrous THF (2 mL). This colourless solution was then transferred by syringe to the suspension of $ZnCl_2$. The reaction was stirred for 10 minutes. The remaining inorganic insolubles were then removed by cannula filtration to give a pale yellow solution. A large excess of anhydrous Et_2O (15 mL) was added to the THF solution, which was stirred for 10 minutes then allowed to settle. The supernatant was decanted and the remaining white solid (87 mg, 85%) dried under vacuum.

^{1}H NMR (600 MHz, CD_3CN) δ = 0.69 (s, 3H), 1.70-1.80 (m, 1H), 2.07-2.14 (m, 4H), 2.75-2.85 (m, 4H), 2.98 (s, 2H), 3.14-3.26 (m, 4H), 3.34 (s, 2H), 3.70 (s, 2H).

^{13}C NMR (101 MHz, CD_3CN) δ = 23.9, 24.7, 34.5, 49.6, 54.7, 57.5.

ν_{max} /cm^{-1}: 3252, 2931, 2873, 2250, 2162, 2049, 1980, 1591, 1459, 1413, 1376, 1348, 1292, 1244, 1220, 1104, 1080, 1045, 1023, 972, 950, 856, 775, 632, 613, 577, 559

Nominal ESI-MS (*m/z* -ESI): Found: 256 (M^+. $C_8H_{19}N_3ZnCl$ predicted mass: 256).

3.5.7 Synthesis of [Cu^{I}(4)](OTf) (32)

In a glove box, **4** (0.079 g, 0.15 mmol) and [$Cu^{I}(MeCN)_4$](OTf) (0.063 g, 0.17 mmol) were stirred in anhydrous MeCN (5 mL) for 10 minutes. The reaction mixture was then concentrated under vacuum. Anhydrous MeCN (1 mL) was added followed by anhydrous Et_2O (20 mL) giving an off-white precipitate. The precipitate was collected by vacuum filtration and washed with anhydrous Et_2O (2 5 mL) to give [(**4**)Cu^{I}](OTf) (0.045 g, 49%) as pale yellow solid.

Nominal ESI-MS (*m/z* -ESI): Found: 619 (M+ + K. $C_{36}H_{43}N_3Cu^{0}K$ predicted mass: 619.2390).

Air sensitive compound, no melting point determined.

3.5.8 Synthesis of $[Cu^{I}(4)](PF_6)$ (33)

In a glove box, **4** (0.050 g, 0.09 mmol) and $[CuI(MeCN)_4](PF_6)$ (0.040 g, 0.1 mmol) were stirred in anhydrous DCM (2 mL) for 10 minutes. Anhydrous Et_2O (15 mL) was added resulting in the formation of a pale yellow precipitate. The supernatant was decanted and the precipitate dissolved in the minimum amount of DCM. The resulting solution was layered with anhydrous Et_2O and the product recrystallised to give **33** as pale yellow needles (0.048 g, 65%).

^{1}H NMR (400 MHz, $CDCl_3$) δ = 0.17 (s, 3H), 1.841.98 (m, 2H), 2.042.11 (m, 4H), 2.33 (d, J = 14.5 Hz, 2H), 2.42 (s, 3H), 2.552.63 (m, 2H), 3.19 (d, J = 12.3 Hz, 2H), 3.43 (s, 4H), 3.503.63 (m, 2H), 3.96 (d, J = 12.3 Hz, 2H).

^{13}C NMR (151 MHz, CDCl3) δ = 2.9, 23.8, 24.4, 30.9, 38.4, 59.2, 59.4, 61.7, 62.2, 67.1, 127.5, 128.4, 128.6, 129.3, 130.9, 131.6, 134.8, 139.3.

3.5.9 Crystallographic Information

The X-ray intensity data were measured at the temperatures given in Table 3.5 using an Oxford Cryosystems low temperature device using a MiTeGen micromount. See Table 3.5 for collection parameters and exposure time. Bruker APEX software was used to correct for Lorentz and polarization effects. Data were corrected for absorption effects using the Multi-Scan method (SADABS). The structures were solved and refined using the Bruker SHELXTL Software Package

Table 3.5: Crystal data and refinement parameters for **24**/**25**, **27**, **29** and **33**

.

	24/**25**	**27**	**29**	**33**
Empirical formula	$C_{32}H_{76}Cl_8Fe_4N_{12}$	$C_{40}H_{92}N_{12}Ni_4O_{12}$	$C_{17}H_{38}Cl_2CuN_6$	$C_{38}H_{46}CuF_6N_4P$
Formula weight	1136.04	1168.09	460.97	767.30
Temperature / K	100.01	100.0	100.04	100(2)
Crystal system	Monoclinic	Tetragonal	Monoclinic	Monoclinic
Space group	$P2_1/c$	$I4_1/a$	C_2/c	$P2_1/c$
Unit cell dimensions	a = 12.9224(3) Å	a = 23.0815(13) Å	a = 25.3015(16) Å	a = 13.9502(5) Å
	b = 15.6759(4) Å	b = 23.0815(13) Å	b = 12.2091(7) Å	b = 16.7687(6) Å
	c = 12.3817(3) Å	c = 10.6098(7) Å	c = 15.6702(9) Å	c = 15.9798(6) Å
	α= 90°	α= 90°	α= 90°	α= 90°
	β=106.9870(11)°	β= 90°	β= 96.086(4)°	β= 105.4835(12)°
	γ= 90°	γ= 90°	γ= 90°	γ= 90°
Volume / Å^3	2398.74(10)	5652.4(7)	4813.4(5)	3602.4(2)
Z	2	4	8	4
Density (calculated) / Mg m^{-3}	1.573	1.373	1.272	1.415
Crystal Size / mm^3	0.26 x 0.14 x 0.12	0.13 x 0.07 x 0.06	0.16 x 0.08 x 0.05	0.500 x 0.130 x 0.050
Reflections collected	57613	36451	31524	64377
Independent reflections	9686 [$R_{(int)}$ = 0.0505]	2923 [$R_{(int)}$ = 0.2210]	4858 [$R_{(int)}$ = 0.1516]	10124 [$R_{(int)}$ = 0.0551]
Final R indices [I>2σ(I)]	R_1 = 0.0310 wR_2 = 0.0577	R_1 = 0.0627 wR_2 = 0.1283	R_1 = 0.0616 wR_2 = 0.1299	R_1 = 0.0392 wR_2 = 0.0825
R indices (all data)	R_1 = 0.0525 wR_2 = 0.0653	R_1 = 0.1115 wR_2 = 0.1421	R_1 = 0.1204 wR_2 = 0.1515	R_1 = 0.0708 wR_2 = 0.0943

Chapter 4

Synthesis and Characterisation of a Tricyclic, Tripodal, Triamine Ligand

4.1 Introduction

In Chapter 3, we explored the coordination chemistry of the two mesocyclic ligands (**2** and **4**) synthesised in Chapter 2. We showed that **2** readily reacted with metals such as iron, nickel and zinc to form the corresponding metal complexes. However, the steric bulk around the metal binding pocket in these systems was insufficient to prevent the formation of multinuclear complexes. In order to combat this, we synthesised, **4**, the benzylated analogue of **2**. By installing the bulky benzyl groups, we had hoped to increase the steric protection around the mental binding pocket such that the formation of multinuclear complexes was unfavourable. However, analysis of the crystal structure of the corresponding Cu^{I} complex showed that **4** preferentially bound in a bidentate manner, *via* the 1,5-diazacyclooctane (DACO) nitrogen atoms, with the third *exo*-cyclic arm remaining unbound. This resulted in the trigonal planar complex **33**. We reason that this occured as a result of the size of the benzyl groups *i.e.* they are too bulky to accommodate all four around one metal centre.

As outlined in Chapter 1, polyazamacrocycles have been utilised to great effect in stabilising transition metal-oxo species.[80] The most notable of these is the four-coordinate tetraazamacrocycle, 1,4,8,11-tetramethyl-1,4,8,11-tetraazacyclotetradecane (TMC), which has been used in stabilising a variety of transition metal oxygen adducts; such as Fe^{IV}−oxo, Ni^{II}−superoxo, Ni^{III}−peroxo and Co^{III}−peroxo complexes.[180–184] Several three-coordinate analogues have also been reported in the literature and extensively studied. The most common of these is the triazamacrocycle, 1,4,7-triazacyclononane (TACN). While TACN has been shown to form 1:1 ligand to metal complexes, the ring size of TACN (9 atoms) is sufficiently small that it binds in a facially capping manner.[152] This is in stark contrast to TMC which binds meridionally, with the metal atom almost in the same plane as the nitrogen atoms.[80] A direct consequence of this is that TACN complexes form dinuclear complexes after reaction with O_2, regardless of the size of the *N*-alkly groups. For example, the Scarborough group have developed *N-tertbutyl* substituted TACN which was found to form a dicopper(II)

peroxo species after reaction with O_2.[151,154]

Closely related to TACN, but not as commonly encountered is 1,5,9-triazacyclododecane (TACDD).[152] Also a triazamacrocycle, TACDD contains a twelve membered ring, as opposed to the nine membered ring in TACN. This increase in ring size results in the metal sitting closer to the plane of nitrogen atoms and consequently, the metal is more sterically shielded by the ligand periphery. This is exemplified by the formation of a *pseudo*-tetrahedral Zn^{II} complex and even a trigonal planar Cu^{I} complex, which have both been crystalographically characterised.[152,155] However, Tolman and co-workers have shown that the trigonal planar coordination of the Cu centre nullifies its reactivity towards O_2.[152]

Inspired by these reports, we envisioned the synthesis of the macrocyclic **5**, in which the cyclic and acyclic nitrogen atoms in **2** would be linked with two propane bridges. We believed that incorporating these additional two propane linkers into **2** offered several benefits over **2** and **4**. These benefits could all be described under the broad heading of the macrocyclic effect. Firstly, we reasoned that the installation of two additional propane linkers between the mesocyclic and *exo*-cyclic nitrogen atoms would fix in place the *exo*-cyclic arm of **2**, ensuring its association with the metal centre. Secondly, we believed that the expected trigonal pyramidal geometry of each of the nitrogen atoms would ensure that the lone pairs on each of the three nitrogen atoms are all directed towards the centre of the macrocycle, resulting in the ligand binding in a tridentate fashion. Thirdly, we postulated that the inclusion of the neopentyl backbone (Figure 4.1 blue) to the TACDD macrocyclic framework (Figure 4.1 red) would increase the overall rigidity of the molecule. We believed that this would encourage the binding

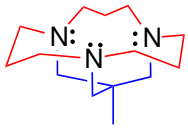

5

Figure 4.1: Chemdraw representation of the target ligand 11-methyl-1,5,9-triazatricyclo[7.3.3.$1^{5,11}$] hexadecane (**5**). The neopentyl skeleton is blue while the TACDD skeleton is shown in red.

of metals by **5**. The reason for this is that **5** contains a high degree of structural pre-organisation. Consequently, the loss of entropy to the ligand upon binding of a metal would be negligible thus increasing the thermodynamic driving force of the reaction compared to **2** or **4**. In addition, we believed that the use of the neopentyl skeleton in alkylating TACDD would ensure that the alkyl groups are all on the same face of the macrocycle, causing the propane bridges to be pushed in the same direction, out of the plane of the nitrogens; affording more steric protection to the metal binding pocket. A similar effect has been described by Que and co-workers for TMC.[74] Finally, the use of propane linkers would maximise the formation of thermodynamically favourable, six-membered rings. A total of six six-membered rings would be formed on the binding of a metal by **5**, which we reasoned would make **5** an excellent chelating ligand. We believed that the additional structural features incorporated into **5**, compared to **2** or **4**, would help to aleviate the problems which we encountered in Chapter 3.

In this chapter, we describe the synthesis of **5** from the mesocycle, **22**. We also explore the acid base chemistry of **5** and demonstrate its exceptionally basic nature. Furthermore, we also explore the coordination chemistry of **5** and present evidence for the formation of its lithium and copper complexes.

4.2 Synthesis and Characterisation of 35

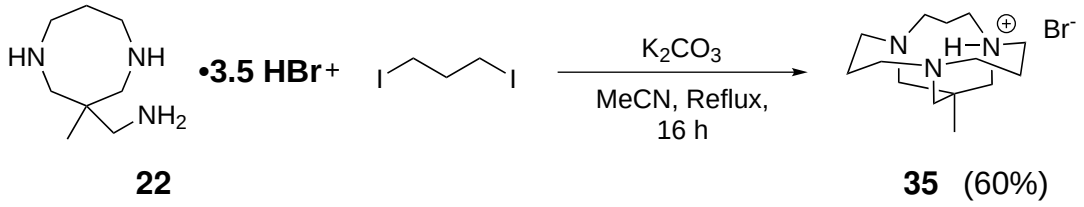

22 **35** (60%)

Scheme 4.1: Synthesis of **35** *via N*-alkylation of **22** with 1,3-diiodopropane.

We identified **22** as the most suitable candidate for the synthesis of **5**. The reasons for this were two-fold. The first is that there is a significant amount of structural pre-organisation in **22**, owing to the presence of the DACO ring. We reasoned that this would strongly promote the formation of **5**. Secondly, **22** is poorly soluble in acetonitrile, we reasoned that this could be utilised as an effective dilution. This was important as it meant we would not have to work under the high dilution conditions which are regularly encountered in the synthesis of macrocycles.[219] **22** was reacted with 1,3-diiodopropane in the presence of K_2CO_3 in acetonitrile (MeCN) (Scheme 4.1). Analysis of the crude reaction product by electrospray ionisation mass spectrometry (ESI-MS) gave a peak at *m/z* = 238.2292 for $C_{14}H_{27}N_3 + H^+$ (expected *m/z* = 238.2283), indicating that intramolecular *N*-alkylation had occured, confirming the formation of the desired ligand skeleton in **5**.

Analysis of the ^{1}H nuclear magnetic resonance (NMR) spectrum of the crude sample showed a quintet at 2.27 ppm and a triplet at 3.28 ppm. This indicated the presence of unreacted 1,3-diiodopropane. This was removed by slow precipitation of a dichloromethane (DCM) solution of **35** with pentane. The ^{1}H NMR spectrum of the pure product has been assigned in conjunction with the corresponding heteronuclear single quantum coherence (HSQC) spectra (Figure 4.2, Figure 4.3). Importantly, this confirmed that the multiplets at 1.77-1.84 ppm and 2.11-2.24 ppm as well as those at 2.65-2.74 ppm and 3.53-3.66 ppm were infact pairs of diastereotopic signals, as these protons belonged to the same carbon atom. Installation of the additional two propane bridges, as expected, significantly reduced the conformational flexibility of **35** when compared

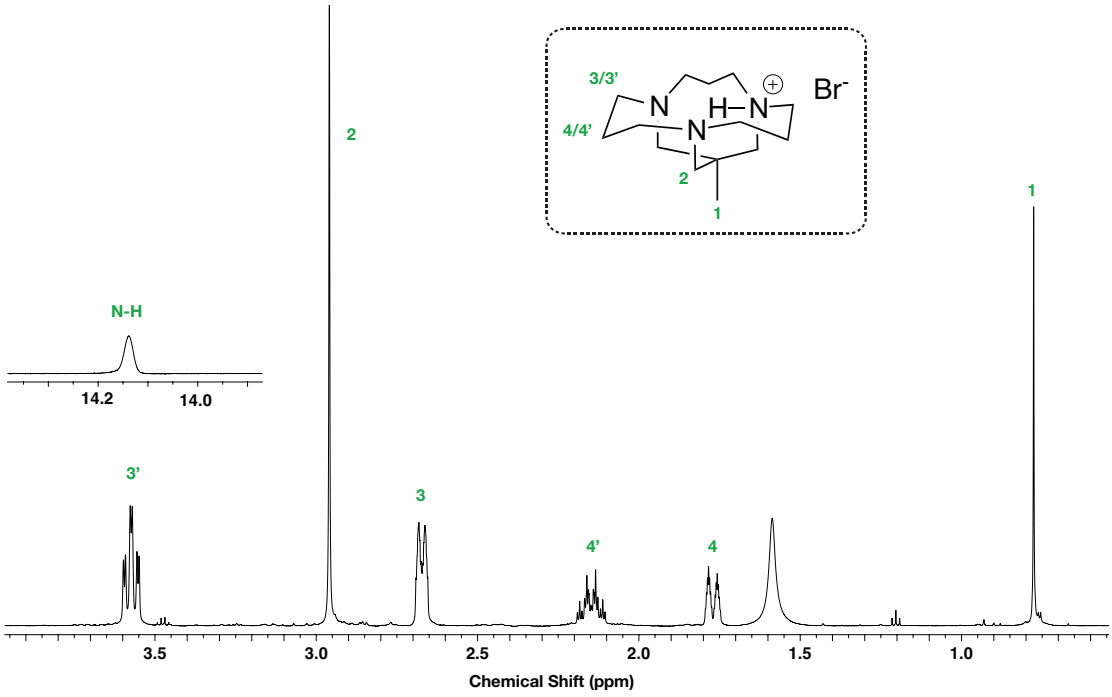

Figure 4.2: ^{1}H NMR Spectrum of **35**. ($CDCl_3$, 600 MHz) Signal assignments are shown in the inset. Diastereotopic protons have been arbitrarily labelled.

to **22** or **4**. This was borne out in the ^{1}H NMR spectrum (Figure 4.2), which showed two discrete multiplets for each pair of diastereotopic protons 3/3′ and 4/4′, similar to the spectra observed for [**4**·H](PF_6) and the Zn^{II} and Cu^{I} complexes discussed in Chapter 3. The appearance of these signals is discussed in more detail below. Interestingly, we observed a resonance at 14.14 ppm, integrating to one proton, which we tentatively assigned as an N-H based on the proposed structure of **5**. The relatively simple nature of the spectrum in Figure 4.2 suggests that **35** is highly symmetrical and that the proton is either shared equally between the three nitrogen atoms or, alternatively, shuttling between the three equivalent nitrogen atoms on the NMR time scale. ^{1}H-^{15}N correlation spectroscopy (COSY) experiments failed to confirm this signal as an N-H as no cross-peaks were observed. However, a D_2O shake experiment, in which a drop of D_2O was added to a sample of **35** in $CDCl_3$ proved highly informative.The signal at 14.14 ppm was found to slowly decrease in intensity until it was no longer observable after a period of twelve days. This indicated that this signal arose from an exchangeable proton which,

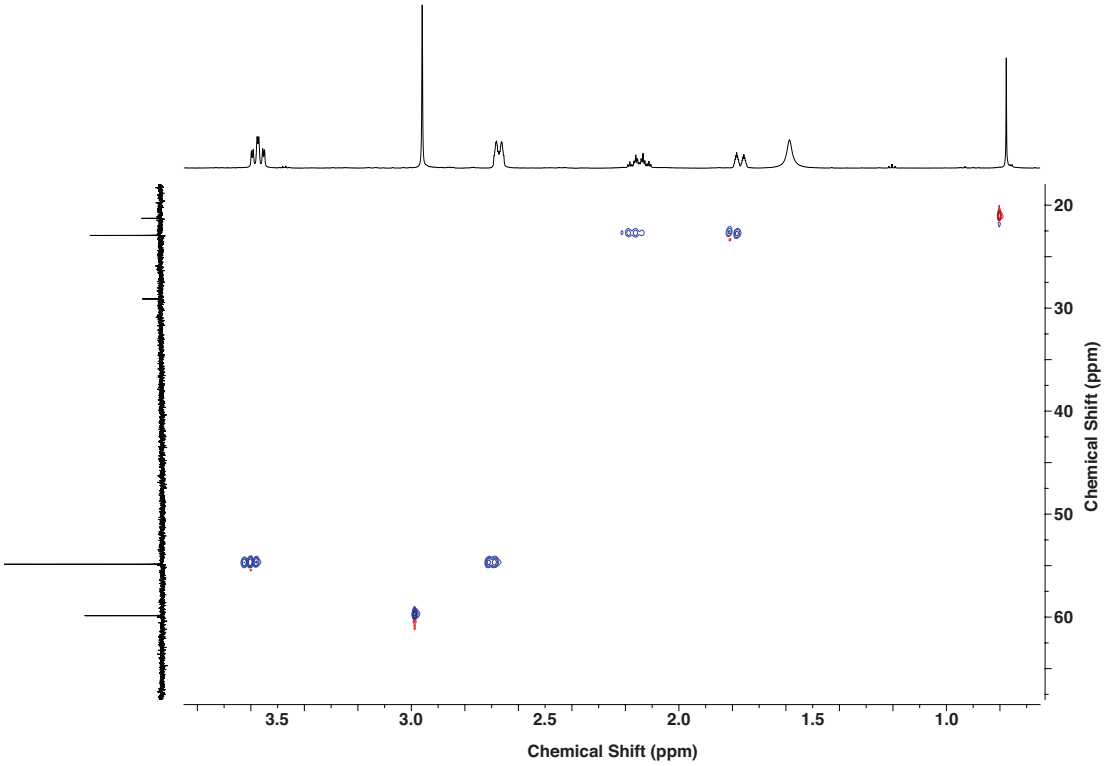

Figure 4.3: HSQC NMR Spectrum of **35**. ($CDCl_3$, 600 / 151 MHz) This spectrum confirms the proton assignments given in Figure 4.2 and also illustrates the presence of diastereotopic signals.

given the proposed structure of **35** was most likely an N-H. The long timescale of this reaction is discussed in more detail below.

Single crystals of **35** were grown from the slow diffusion of diethyl ether into an ethanolic solution of **35**. **35** was found to crystallise in the $P2_1/n$ space group. The asymmetric unit was found to contain two independent ion pairs, each consisting of a $C_{14}H_{28}N_3^+$ cation and a bromide anion (Figure 4.4. Selected bond lengths are shown in Table 4.1, crystal data and refinement parameters are given in Table 4.2). N-H atoms were located and refined with restraints (*vide infra*). In the solid state, the three DACO rings present in **35** are all in the boat-chair conformation, with an average C-N-C fold angle of 113.79°. This was similar to the fold angle observed in [**4**·2H]($(OTf)_2$). We believe that this conformation is favoured as intramolecular interactions are minimised. This idea can be extended to the solution state and used to rationalise the different splitting patterns observed in the signals for the 3/3′ and 4/4′ diastereotopic pairs of

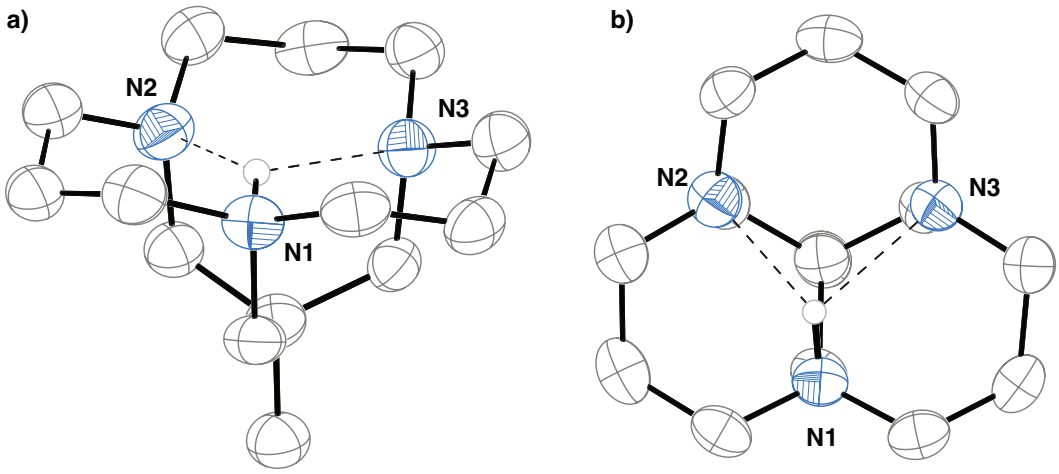

Figure 4.4: Thermal ellipsoid plot of **35**. a) Representative example of one of the fragments from the asymmetric unit. b) Top view of the binding pocket of **35** illustrating the association of the proton with N1 and the highly symmetric nature of the binding pocket. Thermal ellipsoids are shown at the 50% probability level. Anions have been omitted for clarity. Only N-H atoms are shown for clarity.

protons in the ^{1}H NMRspectrum (Figure 4.2).

Figure 4.5a shows a Newman projection of one of the propylene linkers in **35**, generated from the crystal structure obtained for **35**. The dihedral angles are shown in red. Based on the Karplus equation, we can expect that the coupling constant between vicinal protons increases to its maximum as the dihedral angle between these protons tends towards 180°.[220] It is clear from Figure 4.5 that in the boat-chair conformation observed in **35**, the dihedral angle is maximised for $H_{3'}$ and $H_{4'}$ (175°) but not for H_3 and H_4 (∼60°). Consequently, the larger coupling constant between $H_{3'}$ and $H_{4'}$ gives rise to the well-defined multiplets in Figure 4.2 at ∼2.15 and 3.55 ppm. Furthermore, this implies that **35** has a preferred conformation even in solution, as should the propylene linkers be free to move between the two possible conformers *i.e.* the boat-boat conformation (Figure 4.5b), one would expect this coupling phenomenon to average out and give rise to identical signals for both of the protons in each of diastereotopic pairs. Importantly, this suggests that the structure of **35** is highly conformationally rigid, which should make complex formation more entropically favourable. The average N-N distance in **35** is 2.71 Å, which is comparable with that observed in protonated TACN (2.76 Å).[221] No equivalent data is available for protonated TACDD. This data implies that we have

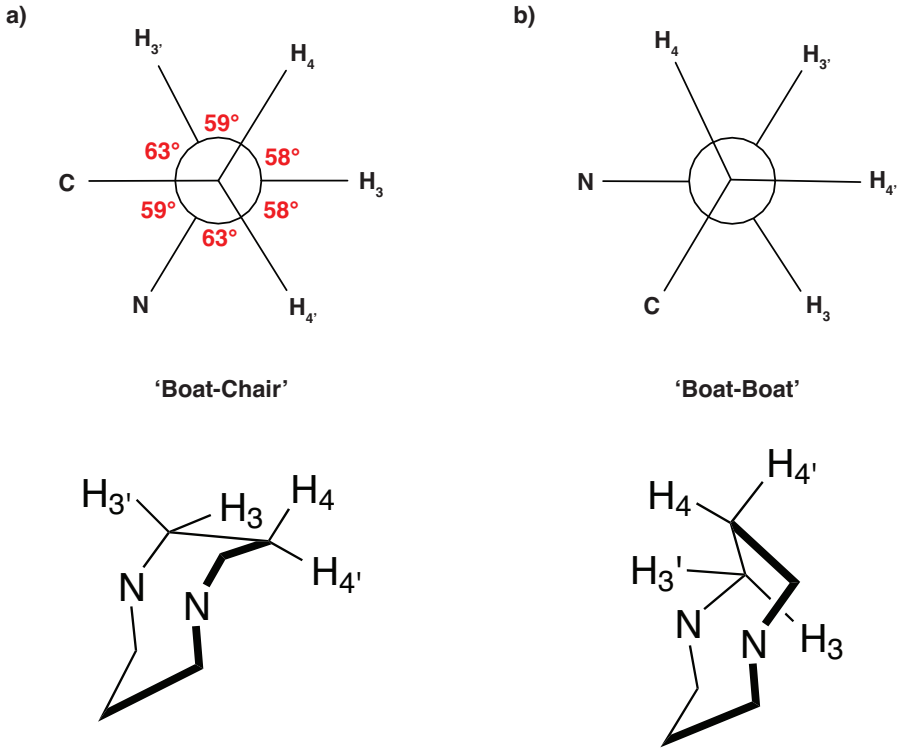

Figure 4.5: a) A Newman projection and corresponding chemdraw of the boat-chair conformer of the DACO ring found in **35**, generated from the X-ray crystal structure shown in Figure 4.4. This illustrates the large dihedral angle between vicinal protons $H_{3'}$ and $H_{4'}$; b) A hypothetical Newman projection and corresponding chemdraw of the alternate, boat-boat conformation of the DACO ring in **35**. This illustrates the anticipated large dihedral angle between vicinal protons H_3 and H_4 in this conformation.

been successful in narrowing the binding pocket of the TACDD fragment of **35**, so as to encourage the formation of *pseudo*-tetrahedral complexes.

4.3 Acid-base Behaviour of 35

Obtaining the crystal structure of **35** confirmed that, curiously, we had isolated our reaction product as the HBr salt. Importantly, this corroborated our assignment of the signal at 14.14 ppm in the ^{1}H NMR spectrum Figure 4.2 as resulting from an N-H. This was in contrast to the synthesis of **4**, in which the freebase was isolated directly from the reaction mixture. This suggested that the p*K*a of **35** is unusually high for a tertiary amine (p*K*a Et_3NH^+ = 10.75 in H_2O), as it was not deprotonated by the carbonate base during the reaction. Furthermore, work-up of the reaction of **22** with 1,3-diiodopropane (Scheme 4.1) under anhydrous conditions confirmed that the proton was not provided by adventitious water. We believe that this high basicity was the reason that the reaction shown in Scheme 4.1 proceeded so cleanly. The formation of an ammonium ion in the final step of the reaction, as opposed to the tertiary amine, prevented quaternisation of the amines in **35**, and thus the reaction proceeded without any side products. Similar phenomena have been observed in the synthesis of cage adamanzanes, which have also been found to be highly basic.[222] Interestingly, adamanzanes have also been shown to have similarly downfield ammonium N-H signals as well as an extremely low rate of H/D exchange in D_2O shake experiments; this has been attributed to encapsulation of the proton by the cage like structure.[223]

We believe that the high basicity of **35** can be ascribed to a proton sponge type effect. The same logic has been applied to account for the high basicity of triazamacrocycles such as TACDD, and related systems described by Bell and co-workers.[219]

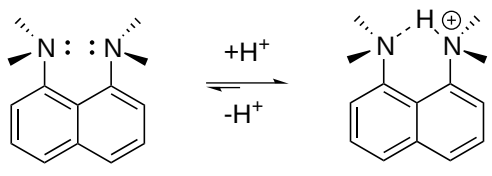

'Proton Sponge'

Figure 4.6: The proton sponge (1,8-Bis(dimethylamino)naphthalene) has p*K*a of 12.1 in H_2O. The unusually high p*K*a is a result of strain relief and the formation of intramolecular hydrogen bonds upon protonation.[224]

The archetypal proton sponge (Figure 4.6) has a p*K*a of 12.1 in H_2O.[224] This class of compounds characteristically have a high basicity.[225] This is a consequence of protonation modulating the interaction between the two nitrogen lone pairs. Furthermore, due to the close proximity of a hydrogen bond acceptor, *i.e.* the second nitrogen, a strong hydrogen bond is formed between the N-H and adjacent nitrogen, essentially chelating the proton.[225] Both of these factors contribute to a significant stabilisation of the conjugate acid and render the protonation reaction highly exothermic. Therefore, this class of compounds have a high p*K*a.[225] Furthermore, the protons in these molecules typically exhibit low kinetic basicity. That is, they show slow kinetics in H/D exchange reactions.[225] The practical consequence of the observed high thermodynamic and low kinetic basicity of these compounds is that while they are readily protonated, the proton can be difficult to remove. However, in instances where the proton can be replaced by a metal, the resulting complexes have been shown to demonstrate exceptionally high kinetic stability.[226]

Analysis of **35** by X-ray crystallography showed that two discrete fragments were found in the asymmetric unit of **35**. While these fragments are not equivalent by symmetry, it is apparent from Table 4.1 that both fragment 1 and fragment 2 show similar structural parameters. N-H Hydrogen atoms were located and refined with restraints, the details of which are given in the experimental section. In contrast to the ^{1}H NMR data shown in Figure 4.2 discussed above, the N-H proton was found to be strongly associated with N1. This was also supported by the longer mean N1-C distance (Table 4.1) compared to the mean N2/N3-C distances, which suggested that N1 was protonated while N2

Table 4.1: Selected bond lengths and interatomic distances for **35**.

Selected Distances /Å	Fragment 1	Fragment 2
N1-N2	2.67	2.67
N1-N3	2.69	2.67
N2-N3	2.78	2.81
Mean N-N Distance	2.71	2.72
Mean N1-C Distance	1.51	1.50
Mean N2-C Distance	1.47	1.47
Mean N3-C Distance	1.48	1.47

and N3 were not. Similar results have been observed by Springborg in the study of adamanzanes, where the ^{1}H NMR spectra suggested that the proton was shuttling between the nitrogen atoms on the NMR timescale while in the solid state the proton was located on one nitrogen atom in particular.[223] Furthermore, the -NH$\cdots$N distances in **35** were found to be relatively short ($\sim$ 2.01 Å) and, importantly, significantly less than the sum of the Van der Waals radii of nitrogen and hydrogen (2.75 Å). This is suggestive of a hydrogen bonding interaction between the N-H and the remaining two nitrogen atoms.[227] This is a direct result of the structural rigidity of **35**. Chelation of a proton in this manner significantly reduces the interaction of the nitrogen lone pairs in **35**. In the solid state, the trigonal pyramidal geometry of the nitrogen atoms in **35** implies that the lone pairs are directed towards the centre of the cavity, inducing a significant amount of strain in the structure. As ^{1}H NMR spectrum suggests that the conformation of the ring is fixed, this cannot be alleviated by the inversion of one or more of the nitrogens. Therefore the binding and retention of a proton in the centre of the macrocycle is highly thermodynamically favourable as it reduces this interaction. Consideration of these structural factors above, which suggest that protonation of **5** leads to a relief of strain caused by the interaction of the nitrogen lone pairs as well hydrogen bonding interactions between the N-H and adjacent nitrogen atoms add weight to the idea that **35** is superbasic. With this in mind, we next sought to remove the proton and isolate the freebase, in order to synthesise metal complexes of **35**.

It has been reported that the formation of an intramolecular hydrogen bond can increase the p*K*a of a molecule by 2-4 p*K*a units while the reduction of lone pair repulsion can increase the p*K*a by up to 6 p*K*a units.[225] With this in mind and considering the literature reported value of the p*K*a of TACDD (12-13),[219] we reasoned that the most convenient base for the deprotonation of **35** would be hydroxide. To this end, we replicated the procedure we had previously used in generating the freebase **2** from **22**. **35** was dissolved in the minimum amount of H_2O and potassium hydroxide (10 eq) was added (Scheme 4.2). This mixture was then added to a solution of toluene and the mixture refluxed in a Dean-Stark apparatus until all of the water had been removed. Curiously, analysis of the post reaction mixture indicated that none of the

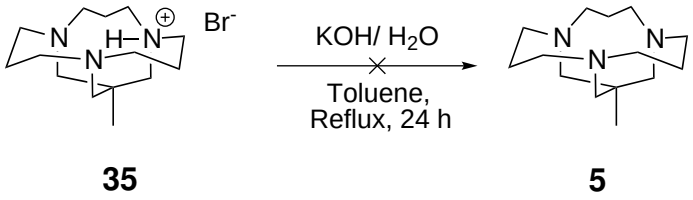

35 **5**

Scheme 4.2: Failed attempt at the deprotonation of **35** using KOH. This led us to conclude that the p*K*a of **35** > 15.7 in H_2O.

freebase, **5**, had been formed. This suggested that hydroxide was not a strong enough base to deprotonate **35** and by extension implied that the p*K*a of **5** was greater than 15.7 in H_2O.

Consequently, we turned our attention to stronger bases however, our efforts in this area were significantly hampered by the poor solubility of **35**. After work-up of the reaction (Scheme 4.1), **35** was only soluble in halogenated solvents, *N*,*N*-dimethylformamide (DMF) and water. **35** was reacted with KO^{t}Bu in DCM, (Scheme 4.3). Gratifyingly, a pale yellow solution of **35** in DCM turned instantly colourless on addition of one equivalent of KO^{t}Bu. This colour change was accompanied by the formation of a white precipitate. The precipitate was removed by cannula filtration and the remaining solvent removed *in vacuuo*. ^{1}H NMR analysis of this crude reaction product showed the presence of HO^{t}Bu. This was readily removed through repeated azeotropic distillation with anhydrous hexane. Crucially, the ^{1}H NMR spectrum (Figure 4.7b) showed no peak for the N-H proton at 14.14 ppm (Figure 4.7, inset) and the remaining resonances resulting from the cyclic protons were shifted slightly (*cf.* Figure 4.7a). The splitting pattern of the freebase signals remained the same as that observed for the HBr salt, **35** (Figure 4.7a). This suggested that protonation had little effect on the conformation of **5** further supporting the idea that the macrocycle is

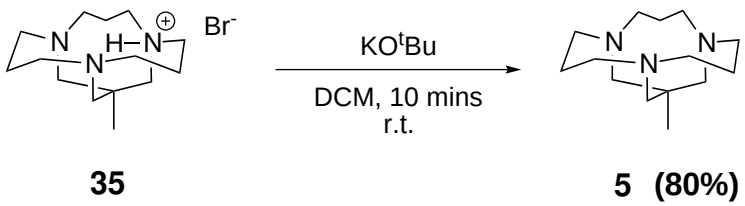

35 **5 (80%)**

Scheme 4.3: The successful deprotonation of **35** in DCM with KO^{t}Bu to give the corresponding freebase **5**.

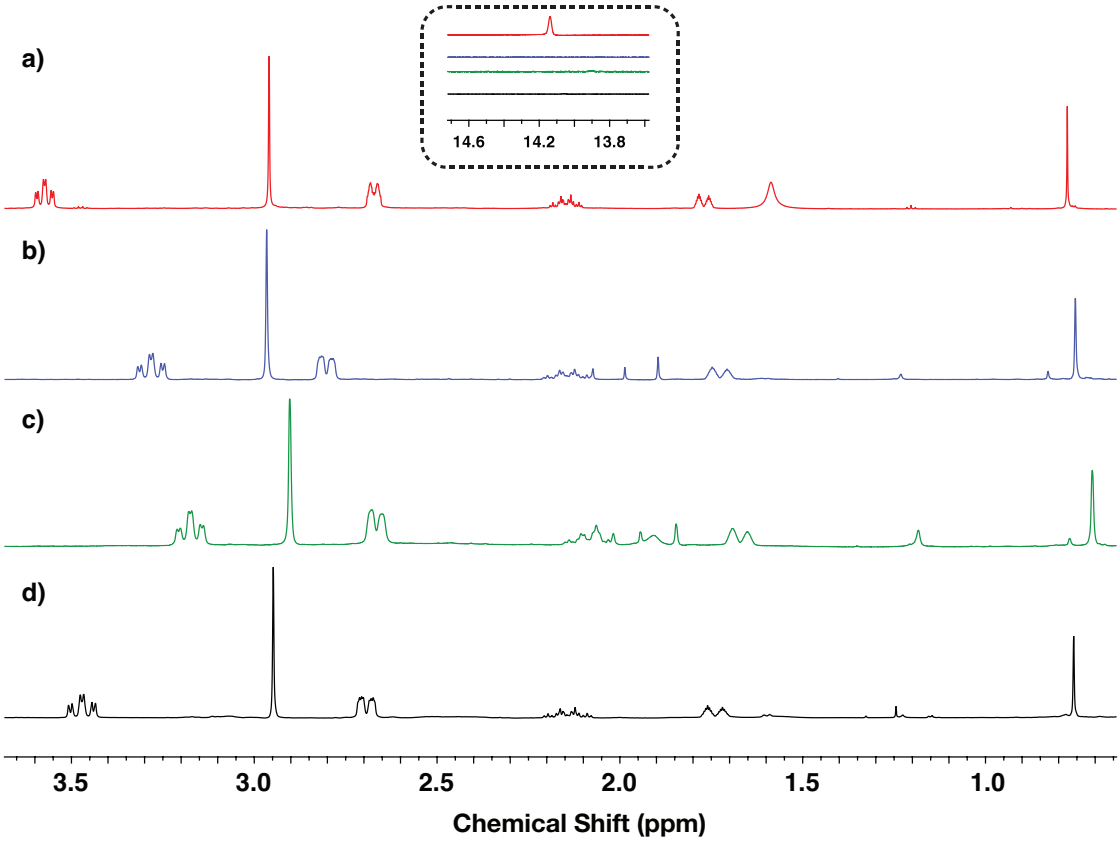

Figure 4.7: ^{1}H NMR spectrum of **5** and related complexes. a)^{1}H NMR spectrum of **35** (600 MHz $CDCl_3$); b) ^{1}H NMR spectrum of **5**; c) ^{1}H NMR spectrum of the reaction of **5** with $LiClO_4$; d) ^{1}H NMR spectrum of the reaction of **5** with $[Cu^{I}(NCCH_3)_4](PF_6)$; inset shows the region of the characteristic N-H peak of the protonated **35**. Spectra **b-d** were collected at 400 MHz in $CDCl_3$.

conformationally rigid. This is in contrast to **4**, in which a reduction in conformational flexibility was observed upon protonation (*vide supra*). The similarity in chemical shift between the aliphatic signals in **35** and **5** likely results from the fact that the proton is only loosely associated with each of the three nitrogens in solution *i.e.* shuttling between them on the NMR time scale, as opposed to being strongly associated with one nitrogen as observed in the solid state (Figure 4.4). We postulate that as there is a negligible change to the local magnetic environment on removal of the proton that the chemical shifts remain relatively similar in **35** and **5**.

4.4 Synthesis of metal complexes 5

With the freebase **5** in hand, we next sought to introduce a metal into the now vacant macrocyclic cavity. To this end we conducted several preliminary NMR tube experiments (Figure 4.7). In the first of these experiments, Figure 4.7c, we added a small amount of $LiClO_4$ to the NMR sample of **5** (Figure 4.7b). We chose to use lithium perchlorate for several reasons. Firstly, it is readily soluble in organic solvents. Secondly, any resulting lithium complex would be stable to oxidation and diamagnetic (*i.e.* NMR active). Finally, similar macrocycles to **5** have been predicted in the literature to be excellent ionophores for lithium.[219] It is clear from the spectrum in Figure 4.7c that addition of lithium to the cavity had a small but noticeable effect on the ^1H chemical shifts, with all of the signals being shifted slightly upfield when compared to Figure 4.7b. As observed in the deprotonation, the relative ordering of the signals was not altered and the splitting patterns remained unchanged. This is once again most likely a result of the conformational rigidity of **5** in solution. We tentatively ascribe this shift to the formation of the lithium complex **36**. However, analysis of the NMR solution by direct injection ESI-MS only displayed a peak corresponding to the mass of the free ligand, and no lithium complex was observed, failing to confirm the identity of the species shown in Figure 4.2c. Encouraged by the notable change in the ^1H NMR signals on addition of lithium, we then attempted to utilise other ^1H NMR compatible metals.

In a similar experiment to that described above, we added a small amount of $[Cu^I(NCCH_3)_4](PF_6)$ to a sample of **5** in $CDCl_3$ (Figure 4.7d). Once again a change in the ^1H NMR spectrum was evident. However, unlike the spectrum aquired after the addition of $LiClO_4$ (Figure 4.7c), there was a marked movement in the multiplet at 3.41-3.53, corresponding to $H_{3'}$. In fact, the spectrum obtained for Cu^I was almost identical to that of the protonated species **35** (Figure 4.7a). Crucially however, no signal was observed at ~14 ppm, corresponding to a N-H proton (Figure 4.7, inset). This confirmed that the reaction had not simply re-protonated the starting material, **5**. Furthermore,

analysis of the reaction mixture by direct injection ESI-MS showed a peak at *m/z* = 318 with an isotopic pattern corresponding to the copper complex, **37**, plus one water molecule (expected *m/z* = 318). Owing to the experimental set up, these values are only accurate to nominal mass and therefore provide strong support for the identity of the complex in the NMR spectrum. The data provided from the NMR tube experiments described above clearly indicate that once **35** has been deprotonated, the three nitrogen atoms are free to bind metal ions. This is clearly demonstrated by the formation of **37**, a low coordinate, late transition metal complex.

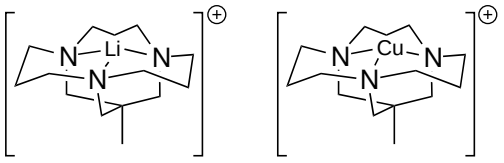

36 **37**

Scheme 4.4: Complexes of **5**. Resulting from NMR tube scale reactions with $LiClO_4$ and $[Cu^{I}(NCCH_3)_4](PF_6)$ in CD_3CN.

4.5 Conclusions and Future Work

In summary, we have shown that reaction of **22** with 1,3-diiodopropane leads to the clean formation of the tricyclicmacrocycle, **35**, which was characterised extensively using NMR spectroscopy and X-ray diffraction. **35** combines both the neopentyl and TACDD structural motifs, which contribute to **35** possessing a high degree of structural rigidity. This manifests in **5** displaying an unusually high p*K*a and suggests that the corresponding freebase, **5**, can be expected to be an excellent σ-donor and therefore, adept at stabilising the high oxidation states expected of late transition metal-oxos.

The rigidity of **5** was also found to impart a significant degree of structural pre-organisation with regards to the formation of *pseudo*-tetrahedral metal complexes of **5**. The lone pairs of each of the nitrogen atoms were found to be directed towards the centre of the TACDD ring in **35** which we believe will strongly promote the binding of **5** in a tridentate mode. Importantly, we have been successful in alkylating the triamine, **22** to give a more sterically protected metal binding pocket. In our opinion, this will prevent the formation of multinuclear complexes. We have also been able to prepare complexes **36** and **37** demonstrating the ability of **5** to form metal complexes.

Future work on this exciting project will be focused on scaling up the synthesis of the copper complex reported above. By doing this, we hope to be able to thoroughly structurally characterise the resulting complex and also begin to investigate the properties which the highly unusual ligand, **5**, imparts to the metal centre. Furthermore, we wish to explore the reactivity of **5** with other first row transition metals such as Fe^{II}, Ni^{II} and Zn^{II} in order to better understand the coordination behaviour of **5**. Ultimately, the goal of this project is to develop our understanding of the Cu^{I} complex to the point where we can begin to examine its reactivity in oxidation reactions. In particular, we would like to investigate the reactivity of the complex towards O_2 as well as oxygen atom transfer (OAT) reagents, such as iodosyl benzene, at low temperatures. By doing this, we hope to be able to identify reactive intermediates such as the corresponding Cu^{II}–$O_2^{\bullet-}$ and Cu^{III}=O complexes. Identifying these species will allow us to begin to

probe the reactivity of late transition metal-oxo species.

4.6 Experimental Section

4.6.1 Materials and Methods

All reagents and solvents were purchased from commercial sources and used as received, unless otherwise stated. $[Cu(MeCN)_4](PF_6)$ were prepared using previously reported procedures.[217] tetrahydrofuran (THF) and diethyl ether (Et_2O) were distilled from sodium and benzophenone and stored under argon. MeCN and DCM were distilled from CaH_2 prior to use. $CDCl_3$ was dried and de-acidified by stirring and subsequently storing over 4 Å molecular sieves and basic alumina. ^1H and ^{13}C NMR were recorded on either an Agilent 400-MR Long Hold Mag. Res. Spectrometer 2 or a Bruker Avance II 600 MHz spectrometer. ESI mass spectra were acquired by direct injection to a Micromass time of flight spectrometer (ToF).

4.6.2 Synthesis of 11-methyl-1,5,9-triazatricyclo[7.3.3.1^{5,11}] hexadecane hydrobromide (35)

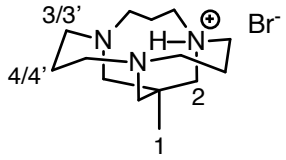

22 (1.57 g, 3.93 mmol), 1,3-diiodopropane (2.32 g, 7.85 mmol) and K_2CO_3 (5.42 g, 39.25 mmol) were added to a round bottomed flask containing acetonitrile (400 mL) and heated at reflux for 16 hours. The reaction mixture was then cooled to room temperature and the remaining K_2CO_3 removed by filtration. The remaining solvent was removed *in vacuuo*. The resulting white residue was dissolved in DCM (2 mL) and filtered to remove any insoluble material. The DCM solution was then added dropwise to a vigorously stirred solution of pentane resulting in the formation of a white precipitate. The precipitate was collected by filtration and washed with pentane (2 x 10 mL) followed by Et_2O (2 x 10 mL) then dried under vacuum to give **35** (0.72 g, 60%). Single crystals suitable for X-ray diffraction were grown by diffusing Et_2O into a concentrated ethanolic solution of **35**.

^{1}H NMR (600 MHz, $CDCl_3$) δ = 0.80 (s, 3H, H_1), 1.77-1.84 (m, 3H, H_4), 2.11-2.24 (m, 3H, $H_{4'}$), 2.65-2.74 (m, 6H, H_3), 2.99 (s, 6H, H_2), 3.53-3.66 (m, 6H$H_{3'}$), 14.17 (s, 1H, N-H).

^{13}C NMR (151 MHz, $CDCl_3$) δ = 22.1, 22.8, 29.0, 54.7, 59.7

HRMS (*m/z* -ESI): Found: 238.2292 (M^+ + H. $C_{14}H_{27}N_3$ predicted mass: 238.2283).

4.6.3 Synthesis of 11-methyl-1,5,9-triazatricyclo[7.3.3.1^{5,11}] hexadecane (5)

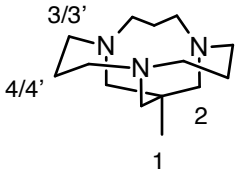

35 (0.2 g, 0.63 mmol) was added to a Schlenk charged with anhydrous DCM (10 mL). KO^{t}Bu (0.071 g, 0.63 mmol) was added and the reaction mixture stirred for 10 minutes. An immediate bleaching of the yellow solution was accompanied by the formation of a white precipitate. The supernatant was transferred by cannula filtration to a second Schlenk and the solvent removed under vacuum to give a colourless oil, **5** (0.127 g, 85%).

^{1}H NMR (600 MHz, $CDCl_3$) δ = 0.77 (s, 3H, H_1), 1.69-1.79 (m, 3H, H_4), 2.10-2.24 (m, 3H, $H_{4'}$), 2.78-2.86 (m, 6H, H_3), 2.98 (s, 6H, H_2), 3.24-3.35 (m, 6H, $H_{3'}$).

4.6.4 Crystallographic Information

The X-ray intensity data were measured at the temperatures given in Table 4.2 using an Oxford Cryosystems low temperature device using a MiTeGen micromount. See Table 4.2 for collection parameters and exposure time. Bruker APEX software was used to correct for Lorentz and polarization effects. Data were corrected for absorption effects using the Multi-Scan method (SADABS). The structures were solved and refined using the Bruker SHELXTL Software Package,

For **35** (both fragments), the location of the ammonium hydrogen was determined from the highest residual on the difference map located in the correct position. There was only one residual in the centre of each macrocycle that fitted this description. The N-H distance was restrained to 0.9 Åand the thermal parameter of the hydrogen was allowed to ride on the parent nitrogen with $U_{(iso)}(H) = 1.2U_{(eq)}(N)$.

Table 4.2: Crystal data and refinement parameters for **35**

	35
Empirical formula	$C_{14}H_{28}BrN_3$
Formula weight	318.30
Temperature / K	100.01
Crystal system	Monoclinic
Space group	$P2_1/n$
Unit cell dimensions	a = 15.2560(6) Å b = 14.9837(6) Å c = 15.4356(6) Å α= 90° β=114.3503(12)° γ= 90°
Volume / Å^3	3214.6(2)
Z	8
Density (calculated) / Mg m^{-3}	1.315
Crystal Size / mm^3	0.420 x 0.190 x 0.030
Reflections collected	40235
Independent reflections	6567 [$R_{(int)}$ = 0.0605]
Final R indices [I>2σ(I)]	R_1 = 0.0557 wR_2 = 0.1669
R indices (all data)	R_1 = 0.0741 wR_2 = 0.1856

Chapter 5

Conclusion and Future Work

5.1 Conclusion

The objective of this thesis was to design and synthesise a ligand which possessed the requisite properties to stabilise late transition metal-oxo species, which we believe will be potent oxidants. We have outlined several criteria that such a ligand must meet. It must enforce a *pseudo*-tetrahedral coordination geometry at the metal centre, it must contain strong σ-donor atoms and it must be sterically bulky. Based on the work presented in this thesis, we are able to draw several interesting conclusions.

5.1.1 Mesocyclic Ligand Synthesis

We reported several synthetic routes towards the synthesis of a mesocyclic tripodal, triamine ligand **22**, which met all of the above criteria. The mesocyclic DACO ring in **2** was readily synthesised *via* a Richman-Aitkins cyclisation of two of the arms of our tripodal starting material **18**. This left the third remaining arm free for further functionalisation. By adopting a modular approach to this synthesis, we have synthesised a library of synthons which may be further derivitised to modulate the steric and electronic properties of the ligand (*vide infra*). **22** was extensively characterised and its structural properties thoroughly investigated. X-ray crystallography revealed that **22** adopted an unusual conformation in the solid state which would disfavour the binding of metals in a tridentate manner. However, upon deprotonation of **22** to give the corresponding freebase **2**, NMR studies revealed that this species retained a high degree of flexibility in solution thus, would be capable of binding metals in the intended manner. We also demonstrated that **22** readily reacted with benzyl bromide to give **4**. This resulted in a more sterically bulky analogue of **2**. NMR studies suggested that **4** retained a high degree of flexibility in solution although this was reduced after monoprotonation of the DACO ring in **4**. These results indicated that we had been successful in isolating two ligands, which would be capable of stabilising late transition metal-oxos.

5.1.2 Coordination Chemistry of Mesocyclic Ligands 2 and 4

Having isolated both **2** and **4** we then explored their reactivity with first row transition metals. We have shown that in the absence of bridging ligands, **2** tends to form square pyramidal complexes. In the case of the reaction of **2** with [$FeCl_2$], [$Cu(OAc)_2$] and [$Cu(OTf)_2$] X-ray crystallography indicated the formation of the square pyramidal complexes **24**, **29** and **30**. Similarly, ^{1}H NMR and ESI-MS were suggestive of the formation of a square pyramidal complex, **31**, after the reaction of **2** with [$ZnCl_2$]. However, we also obtained crystal structures of polymetalic six coordinate complexes, **25** and **27**, when bridging ligands were present in the reaction mixture. Importantly, we did not observed any evidence for the formation of complexes with the general formula $[M^n(\mathbf{2})_2]^{n+}$. This suggested that our ligand modifications had been successful in overcoming the drawbacks associated with tripodal ligands such as 1,1,1-tris(aminomethyl)ethane (TAME). These results also indicated that under the reaction conditions employed, the steric bulk associated with **2** was insufficient to promote the formation of *pseudo*-tetrahedral metal complexes. Therefore, we also investigate the reactivity of **4**. We have shown that a trigonal planar Cu^I complex, $[Cu^I(\mathbf{4})(MeCN)](PF_6)$, results from the reaction of **4** with $[Cu^I(MeCN)_4](PF_6)$. This suggested that the bulk of the benzyl groups prevented their accommodation around the same metal centre.

5.1.3 Macroocyclic Ligand Synthesis

We envisioned further modifying **2** to give the tricyclic macrocycle **5**; which was readily synthesised through reaction of **22** with 1,3-diiodopropane and isolated as the corresponding HBr salt, **35**. ^{1}H NMR studies suggested that **35** was highly conformationally rigid and that this rigidity was maintained even after deprotonation. The inherent rigidity of **5** was used to rationalise the exceptionally high pka of **35**. This data suggested that **5** would bind metals in a facially capping manner and be an excellent σ-donor. Finally, we provided tentative evidence that suggested **5** formed metal complexes upon reaction with lithium or copper.

5.2 Future Work

The future work which should be carried out on this project focuses on two avenues. The first of these avenues is the continued exploration of the coordination chemistry of the three ligands synthesised in this thesis (**2**, **4** and **5**). The second avenue involves making further modifications to the ligand framework in order to modify the structural and electronic properties of the resulting complexes.

5.2.1 Coordination Chemistry

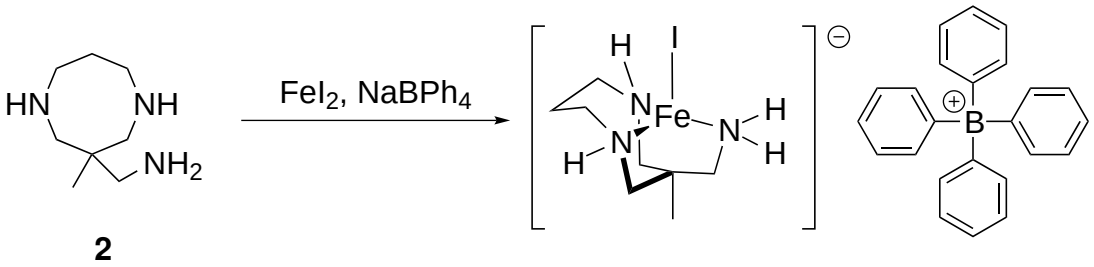

2

Scheme 5.1: Proposed synthetic route to *pseudo*-tetrahedral complexes of **2** utilising bulky anions.

In the case of **2** these studies should be directed towards understanding the factors which affect the coordination geometry of the resulting metal complexes. In particular, one question which needs to be addressed is whether **2** can form *pseudo*-tetrahedral complexes. This should be probed through reactions with metal salts containing bulkier anions (Scheme 5.1. This strategy has been successfully employed by the Chang and Scarborough groups in isolating tetrahedral complexes.[151,175] Furthermore, the factors that affect the formation of multinuclear species should be further investigated.

The key question which remains to be answered with regards to **4** is whether this ligand is capable of binding a metal centre in a tridentate fashion. In order to evaluate this, **4** should be reacted with metals other than Cu^{I} which have a *d*-electron count other than 10. This should make the formation of trigonal planar complexes, like that observed in the reaction with $[CuI(MeCN)_4](PF_6)$ (**33**), unfavourable. For example, it would be

interesting to investigate the reaction of **4** with $[M^{II}(OTf)_2]$ (M = Mn, Fe) as these metals have a stronger preference for forming higher coordinate complexes.

Finally, preliminary results obtained suggested that **5** was capable of forming metal complexs with Li and Cu. These findings must be explored much more thoroughly and every attempt should be made to obtain crystal structures of these complexes. We are incredibly encouraged by these preliminary results with regards to **5** and our confident that these studies will lead to the isolation of a *pseudo*-tetrahedral late transition metal complex. We then hope to be able to explore the reactivity of this species towards OAT reagents at low temperatures and subsequently probe their reactivity in C-H activation reactions.

5.2.2 Synthetic Chemistry

A significant part of this thesis involved the synthesis of the triamine **22**. In adopting a modular approach to the synthesis of this compound, we have developed a library of synthons containing the DACO framework, which could be reacted to further derivitise the ligand architecture.

In order to selectively address the *exo*-cyclic amine arm, **21** could either be alkylated using an alkyl halide or *via* a reductive amination reaction (Scheme 5.2). The resulting product could then be deprotected to yield a ligand in which the *exo*-cyclic arm consists of a tertiary amine while the DACO nitrogen atoms remain as secondary amines. This synthetic methodology may be adopted to benzylate the *exo*-cyclic amine only to give

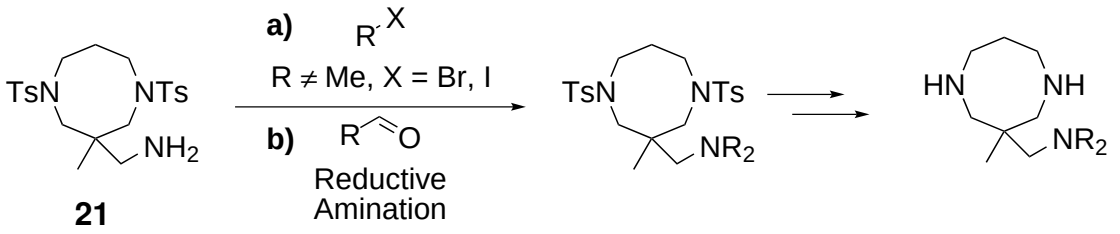

Scheme 5.2: Proposed synthetic route to the selective functionalisation of the *exo*-cyclic amine in **21**. This could be achieved through either alkylation with an alkyl halide or through reductive amination using an aldehyde and appropriate reductant.

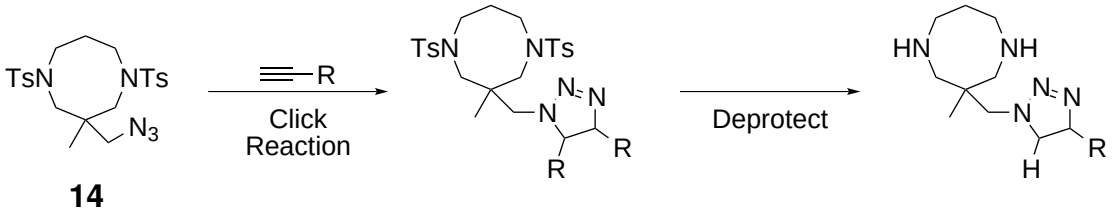

14

Scheme 5.3: Proposed synthetic route to the introduction of an *exo*-cyclic 1,2,3-triazole moiety into the general ligand architecture *via* a click reaction utilising **14**

a less bulky analogue of **4** which may bind metals in a tripodal manner, rather than the bidentate fashion observed for **33**.

The introduction of a 1,2,3-triazole moiety into the ligand architecture may also be an interesting pathway which warrants investigation. This could be achieved through a click reaction between **14** and an alkyne followed by deprotection of the *N*-tosyl groups (Scheme 5.3). The advantages of this are twofold. Firstly, a variety of alkynes could be employed which would allow for facile tuning of the steric and electronic properties associated with the triazole moiety. Secondly, introduction of the triazole moiety would lead to an increase in the size of the binding pocket of the ligand. This would allow the metal to sit closer to the plane of the nitrogen atoms and consequently increase the steric shielding of the metal centre by the ligand framework. A similar result could be achieved through the reaction of **20** with KCN to give the corresponding nitrile which could then be reduced to the primary amine (Scheme 5.4). This would extend the length of the *exo*-cyclic arm by one carbon atom and may also afford extra steric protection for the metal centre.

One of the most disappointing aspects of this work was our lack of success in isolating the tetra-methylated ligand, **3**, which we had targeted from the

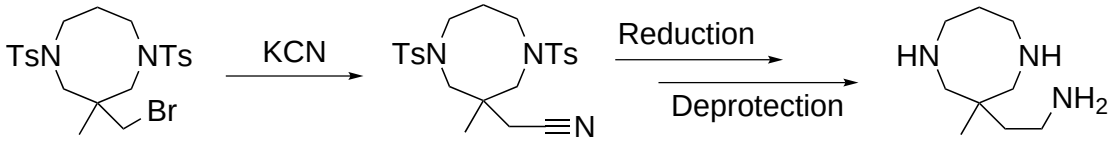

20

Scheme 5.4: Proposed synthetic route to extension of the *exo*-cyclic arm *via* reaction with KCN followed by reduction then deprotection of the *N*-tosyl groups.

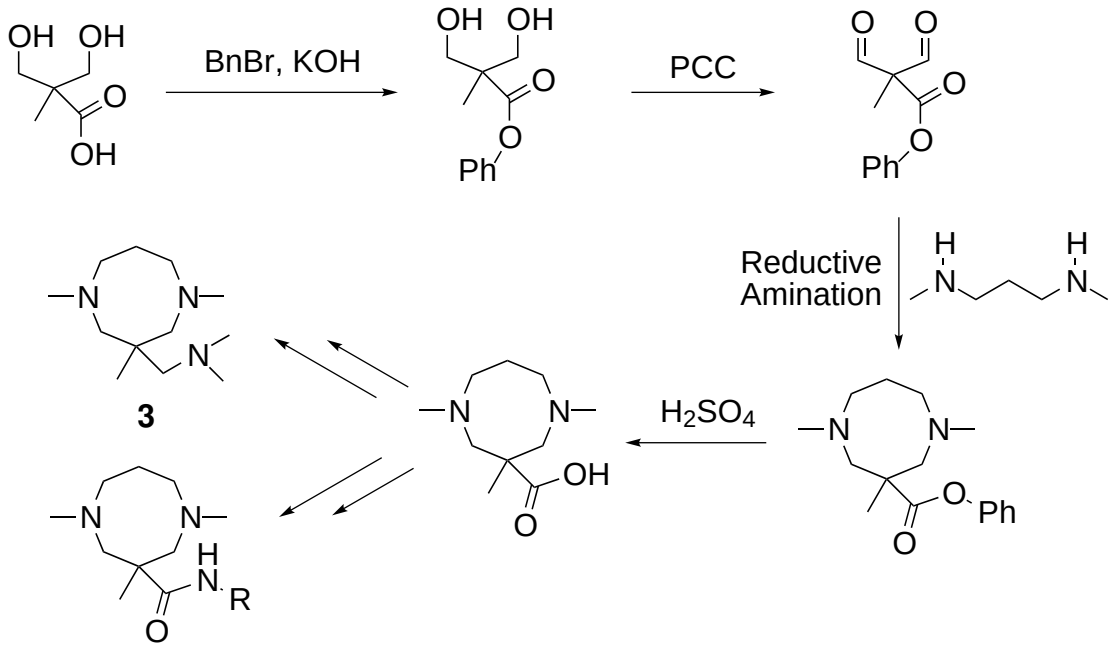

Scheme 5.5: Potential synthetic route to **3** *via* reductive amination using *N,N'*-dimethylethylenediamine.

outset. The results discussed above suggest that a change in synthetic approach is necessary in order to isolate this species. We propose that by changing the starting material to the commercially available 3-hydroxy-2-(hydroxymethyl)-2-methyl propanoic acid (Scheme 5.5) that **3** may be accessible 3-hydroxy-2-(hydroxymethyl)-2-methyl propanoic acid is readily converted to the corresponding benzyl ester.[228] The remaining hydroxyl groups may then be oxidised to the corresponding aldehydes which could then undergo reductive amination with *N,N'*-dimethylethylenediamine to give the dimethylated DACO ring. Cleavage of the benzyl ester protecting group would give the carboxylic acid which could then be converted to **3**. This route represents a significant synthetic undertaking therefore, was not attempted within this project. However, given the results discussed in Chapter 2, this represents the most simple route to **3**. Additionally, this synthesis would allow for the preparation of ligands with *exo*-cyclic amido donors, which have been shown to stabilise metals in high oxidation states owing to their basicity.

References

[1] Arakawa, H. *et al. Chem. Rev.* **2001**, *101*, 953–996.

[2] Caballero, A.; Perez, P. J. *Chem. Soc. Rev.* **2013**, *42*, 8809–8820.

[3] Schwarz, H. *Ang. Chem. Int. Ed.* **2011**, *50*, 10096–10115.

[4] Denisov, I. G.; Makris, T. M.; Sligar, S. G.; Schlichting, L. *Chem. Rev.* **2005**, *105*, 2253–2278.

[5] Rittle, J.; Green, M. T. *Science* **2010**, *330*, 933–937.

[6] Yosca, T. H.; Rittle, J.; Krest, C. M.; Onderko, E. L.; Silakov, A.; Calixto, J. C.; Behan, R. K.; Green, M. T. *Science* **2013**, *342*, 825–829.

[7] Bollinger, J. M.; Price, J. C.; Hoffart, L. M.; Barr, E. W.; Krebs, C. *Eur. J. Inorg. Chem* **2005**, *2005*, 4245–4254.

[8] Hoffart, L. M.; Barr, E. W.; Guyer, R. B.; Bollinger, J. M.; Krebs, C. *Proc. Natl. Acad. Sci. U.S.A.* **2006**, *103*, 14738–14743.

[9] Galonic, D. P.; Barr, E. W.; Walsh, C. T.; Bollinger, J. M.; Krebs, C. *Nat. Chem. Biol* **2007**, *3*, 113–116.

[10] Fujimori, D. G.; Barr, E. W.; Matthews, M. L.; Koch, G. M.; Yonce, J. R.; Walsh, C. T.; J. Martin Bollinger, J.; Krebs, C.; Riggs-Gelasco, P. J. *J. Am. Chem. Soc.* **2007**, *129*, 13408–13409.

[11] Sirajuddin, S.; Rosenzweig, A. C. *Biochemistry* **2015**, *54*, 2283–2294.

[12] Tinberg, C. E.; Lippard, S. J. *Acc. Chem. Res.* **2011**, *44*, 280–288.

[13] Banerjee, R.; Proshlyakov, Y.; Lipscomb, J. D.; Proshlyakov, D. A. *Nature* **2015**, *518*, 431–434.

[14] Solomon, E. I.; Heppner, D. E.; Johnston, E. M.; Ginsbach, J. W.; Cirera, J.; Qayyum, M.; Kieber-Emmons, M. T.; Kjaergaard, C. H.; Hadt, R. G.; Tian, L. *Chem. Rev.* **2014**, *114*, 3659–3853.

[15] Lieberman, R. L.; Rosenzweig, A. C. *Nature* **2005**, *434*, 177–182.

[16] Que, L.; Tolman, W. B. *Nature* **2008**, *455*, 333–340.

[17] Oloo, W. N.; Que Jr, L. *Acc. Chem. Res.* **2015**, *48*, 2612–2621.

[18] Cox, N.; Pantazis, D. A.; Neese, F.; Lubitz, W. *Acc. Chem. Res.* **2013**, *46*, 1588–1596.

[19] Singh, A.; Spiccia, L. *Coord. Chem. Rev.* **2013**, *257*, 2607–2622.

[20] Kim, C.; Chen, K.; Kim, J.; Que Jr, L. *J. Am. Chem. Soc.* **1997**, *119*, 5964–5965.

[21] Chen, K.; Que Jr, L. *J. Am. Chem. Soc.* **2001**, *123*, 6327–6337.

[22] Company, A.; Gómez, L.; Güell, M.; Ribas, X.; Luis, J. M.; Que Jr, L.; Costas, M. *J. Am. Chem. Soc.* **2007**, *129*, 15766–15767.

[23] Company, A.; Gómez, L.; Fontrodona, X.; Ribas, X.; Costas, M. *Chem. Eur. J.* **2008**, *14*, 5727–5731.

[24] Chen, M. S.; White, M. C. *Science* **2007**, *318*, 783–787.

[25] Wang, Y.; Janardanan, D.; Usharani, D.; Han, K.; Que Jr, L.; Shaik, S. *ACS Catal.* **2013**, *3*, 1334–1341.

[26] White, M. C.; Doyle, A. G.; ; Jacobsen, E. N. *J. Am. Chem. Soc.* **2001**, *123*, 7194–7195.

[27] Gormisky, P. E.; White, M. C. *J. Am. Chem. Soc.* **2013**, *135*, 14052–14055.

[28] Bigi, M. A.; Reed, S. A.; White, M. C. *J. Am. Chem. Soc.* **2012**, *134*, 9721–9726.

[29] Chen, M. S.; White, M. C. *Science* **2010**, *327*, 566–571.

[30] Bigi, M. A.; Reed, S. A.; White, M. C. *Nat. Chem.* **2011**, *3*, 216–222.

[31] Howell, J. M.; Feng, K.; Clark, J. R.; Trzepkowski, L. J.; White, M. C. *J. Am. Chem. Soc.* **2015**, *137*, 14590–14593.

[32] Irie, R.; Noda, K.; Ito, Y.; Matsumoto, N.; Katsuki, T. *Tet. Lett.* **1990**, *31*, 7345–7348.

[33] Zhang, W.; Loebach, J. L.; Wilson, S. R.; Jacobsen, E. N. *J. Am. Chem. Soc.* **1990**, *112*, 2801–2803.

[34] Bryliakov, K. P.; Babushkin, D. E.; Talsi, E. P. *J. Mol. Catal. A: Chem.* **2000**, *158*, 19–35.

[35] Feichtinger, D.; Plattner, D. A. *Ang. Chem. Int. Ed.* **1997**, *36*, 1718–1719.

[36] Katsuki, T. *Coord. Chem. Rev.* **1995**, *140*, 189–214.

[37] Caron, S.; Dugger, R. W.; Ruggeri, S. G.; Ragan, J. A.; Ripin, D. H. B. *Chem. Rev.* **2006**, *106*, 2943–2989.

[38] Lyakin, O. Y.; Ottenbacher, R. V.; Bryliakov, K. P.; Talsi, E. P. *ACS Catal.* **2012**, *2*, 1196–1202.

[39] Ottenbacher, R. V.; Samsonenko, D. G.; Talsi, E. P.; Bryliakov, K. P. *ACS Catal.* **2014**, *4*, 1599–1606.

[40] Ottenbacher, R. V.; Bryliakov, K. P.; Talsi, E. P. *Adv. Synth. Cat.* **2011**, *353*, 885–889.

[41] Maity, N. C.; Kumar Bera, P.; Ghosh, D.; Abdi, S. H. R.; Kureshy, R. I.; Khan, N.-u. H.; Bajaj, H. C.; Suresh, E. *Catal. Sci. Tech.* **2014**, *4*, 208–217.

[42] Wang, X.; Miao, C.; Wang, S.; Xia, C.; Sun, W. *ChemCatChem* **2013**, *5*, 2489–2494.

[43] Guillemot, G.; Neuburger, M.; Pfaltz, A. *Chem. Eur. J.* **2007**, *13*, 8960–8970.

[44] Wang, B.; Miao, C.; Wang, S.; Xia, C.; Sun, W. *Chem. Eur. J.* **2012**, *18*, 6750–6753.

[45] Gomez, L.; Garcia-Bosch, I.; Company, A.; Sala, X.; Fontrodona, X.; Ribas, X.; Costas, M. *Dalton Trans.* **2007**, 5539–5545.

[46] Wang, B.; Miao, C.-X.; Wang, S.-F.; Kühn, F. E.; Xia, C.-G.; Sun, W. *J. Organomet. Chem.* **2012**, *715*, 9–12.

[47] Murphy, A.; Dubois, G.; Stack, T. D. P. *J. Am. Chem. Soc.* **2003**, *125*, 5250–5251.

[48] Ilyashenko, G.; De Faveri, G.; Follier, T.; Al-Safadi, R.; Motevalli, M.; Watkinson, M. *Org. Biomol. Chem.* **2014**, *12*, 1124–1134.

[49] Dai, W.; Li, J.; Li, G.; Yang, H.; Wang, L.; Gao, S. *Org. Lett.* **2013**, *15*, 4138–4141.

[50] Cussó, O.; Garcia-Bosch, I.; Font, D.; Ribas, X.; Lloret-Fillol, J.; Costas, M. *Org. Lett.* **2013**, *15*, 6158–6161.

[51] Murphy, A.; Pace, A.; Stack, T. D. P. *Org. Lett.* **2004**, *6*, 3119–3122.

[52] Wu, M.; Wang, B.; Wang, S.; Xia, C.; Sun, W. *Org. Lett.* **2009**, *11*, 3622–3625.

[53] Ottenbacher, R. V.; Talsi, E. P.; Bryliakov, K. P. *Catal. Today* **2016**, In Press.

[54] Miao, C.; Wang, B.; Wang, Y.; Xia, C.; Lee, Y.-M.; Nam, W.; Sun, W. *J. Am. Chem. Soc.* **2016**, *138*, 936–943.

[55] Shen, D.; Qiu, B.; Xu, D.; Miao, C.; Xia, C.; Sun, W. *Org. Lett.* **2016**, *18*, 372–375.

[56] Fernández, I.; Pedro, J.; Roselló, A. L.; Ruiz, R.; Castro, I.; Ottenwaelder, X.; Journaux, Y. *Eur. J. Org. Chem* **2001**, *2001*, 1235–1247.

[57] Song, Y. J.; Hyun, M. Y.; Lee, J. H.; Lee, H. G.; Kim, J. H.; Jang, S. P.; Noh, J. Y.; Kim, Y.; Kim, S.-J.; Lee, S. J.; Kim, C. *Chem. Eur. J.* **2012**, *18*, 6094–6101.

[58] Yoon, H.; Wagler, T. R.; O'Connor, K. J.; Burrows, C. J. *J. Am. Chem. Soc.* **1990**, *112*, 4568–4570.

[59] Fernández, I.; Pedro, J.; Rosello, A. L.; Ruiz, R.; Ottenwaelder, X.; Journaux, Y. *Tet. Lett.* **1998**, *39*, 2869–2872.

[60] Kureshy, R. I.; Khan, N. H.; Abdi, S. H. R.; Iyer, P.; Bhatt, A. K. *J. Mol. Catal. A: Chem.* **1998**, *130*, 41–50.

[61] Nagataki, T.; Ishii, K.; Tachi, Y.; Itoh, S. *Dalton Trans.* **2007**, 1120–1128.

[62] Nagataki, T.; Tachi, Y.; Itoh, S. *Chem. Commun.* **2006**, 4016–4018.

[63] Nagataki, T.; Itoh, S. *Chem. Lett.* **2007**, *36*, 748–749.

[64] Balamurugan, M.; Mayilmurugan, R.; Suresh, E.; Palaniandavar, M. *Dalton Trans.* **2011**, *40*, 9413–9424.

[65] Sankaralingam, M.; Vadivelu, P.; Suresh, E.; Palaniandavar, M. *Inorg. Chim. Acta.* **2013**, *407*, 98–107.

[66] Punniyamurthy, T.; Rout, L. *Coord. Chem. Rev.* **2008**, *252*, 134–154.

[67] Gamez, P.; Aubel, P. G.; Driessen, W. L.; Reedijk, J. *Chem. Soc. Rev.* **2001**, *30*, 376–385.

[68] Markó, I. E.; Giles, P. R.; Tsukazaki, M.; Chellé-Regnaut, I.; Gautier, A.; Brown, S. M.; Urch, C. J. *J. Org. Chem.* **1999**, *64*, 2433–2439.

[69] Fujii, H. *Coord. Chem. Rev.* **2002**, *226*, 51 – 60.

[70] Bois, J. D.; Mizoguchi, T. J.; Lippard, S. J. *Coord. Chem. Rev.* **2000**, *200–202*, 443 – 485.

[71] Bryant, J. R.; Matsuo, T.; Mayer, J. M. *Inorg. Chem.* **2004**, *43*, 1587–1592.

[72] Wright, J. S.; Johnson, E. R.; DiLabio, G. A. *J. Am. Chem. Soc.* **2001**, *123*, 1173–1183.

[73] Blanksby, S. J.; Ellison, G. B. *Acc. Chem. Res.* **2003**, *36*, 255–263.

[74] Rohde, J.-U.; In, J.-H.; Lim, M. H.; Brennessel, W. W.; Bukowski, M. R.; Stubna, A.; Münck, E.; Nam, W.; Que Jr, L. *Science* **2003**, *299*, 1037–1039.

[75] Klinker, E. J.; Kaizer, J.; Brennessel, W. W.; Woodrum, N. L.; Cramer, C. J.; Que Jr, L. *Ang. Chem. Int. Ed.* **2005**, *44*, 3690–3694.

[76] England, J.; Bigelow, J. O.; Van Heuvelen, K. M.; Farquhar, E. R.; Martinho, M.; Meier, K. K.; Frisch, J. R.; Munck, E.; Que Jr, L. *Chem. Sci.* **2014**, *5*, 1204–1215.

[77] Prakash, J.; Rohde, G. T.; Meier, K. K.; Münck, E.; Que Jr, L. *Inorg. Chem.* **2015**, *54*, 11055–11057.

[78] Sastri, C. V.; Lee, J.; Oh, K.; Lee, Y. J.; Lee, J.; Jackson, T. A.; Ray, K.; Hirao, H.; Shin, W.; Halfen, J. A.; Kim, J.; Que Jr, L.; Shaik, S.; Nam, W. *Proc. Natl. Acad. Sci. U.S.A.* **2007**, *104*, 19181–19186.

[79] Decker, A.; Rohde, J.-U.; Klinker, E. J.; Shaun D. Wong, Q.; Que Jr, L.; Solomon, E. I. *J. Am. Chem. Soc.* **2007**, *129*, 15983–15996.

[80] McDonald, A. R.; Que Jr, L. *Coord. Chem. Rev.* **2013**, *257*, 414 – 428.

[81] Kaizer, J.; Klinker, E. J.; Oh, N. Y.; Rohde, J.-U.; Song, W. J.; Stubna, A.; Kim, J.; Münck, E.; Nam, W.; Que Jr, L. *J. Am. Chem. Soc.* **2004**, *126*, 472–473.

[82] Seo, M. S.; Kim, N. H.; Cho, K.-B.; So, J. E.; Park, S. K.; Clemancey, M.; Garcia-Serres, R.; Latour, J.-M.; Shaik, S.; Nam, W. *Chem. Sci.* **2011**, *2*, 1039–1045.

[83] England, J.; Martinho, M.; Farquhar, E.; Frisch, J.; Bominaar, E.; Münck, E.; Que Jr, L. *Ang. Chem. Int. Ed.* **2009**, *48*, 3622–3626.

[84] England, J.; Guo, Y.; Heuvelen, K. M. V.; Cranswick, M. A.; Rohde, G. T.; Bominaar, E. L.; Münck, E.; Que Jr, L. *J. Am. Chem. Soc.* **2011**, *133*, 11880–11883.

[85] Bigi, J. P.; Harman, W. H.; Lassalle-Kaiser, B.; Robles, D. M.; Stich, T. A.; Yano, J.; Britt, R. D.; Chang, C. J. *J. Am. Chem. Soc.* **2012**, *134*, 1536–1542.

[86] MacBeth, C. E.; Golombek, A. P.; Young, V. G.; Yang, C.; Kuczera, K.; Hendrich, M. P.; Borovik, A. S. *Science* **2000**, *289*, 938–941.

[87] Biswas, A. N.; Puri, M.; Meier, K. K.; Oloo, W. N.; Rohde, G. T.; Bominaar, E. L.; Münck, E.; Que Jr, L. *J. Am. Chem. Soc.* **2015**, *137*, 2428–2431.

[88] de Oliveira, F. T.; Chanda, A.; Banerjee, D.; Shan, X.; Mondal, S.; Que Jr, L.; Bominaar, E. L.; Münck, E.; Collins, T. J. *Science* **2007**, *315*, 835–838.

[89] Kundu, S.; Thompson, J. V. K.; Shen, L. Q.; Mills, M. R.; Bominaar, E. L.; Ryabov, A. D.; Collins, T. J. *Chem. Eur. J.* **2015**, *21*, 1803–1810.

[90] Ghosh, M.; Singh, K. K.; Panda, C.; Weitz, A.; Hendrich, M. P.; Collins, T. J.; Dhar, B. B.; Gupta, S. S. *J. Am. Chem. Soc.* **2014**, *136*, 9524–9527.

[91] Prat, I.; Mathieson, J. S.; Güell, M.; Ribas, X.; Luis, J. M.; Cronin, L.; Costas, M. *Nat. Chem.* **2011**, *3*, 788–793.

[92] Collins, T. J.; Powell, R. D.; Slebodnick, C.; Uffelman, E. S. *J. Am. Chem. Soc.* **1990**, *112*, 899–901.

[93] Collins, T. J.; Gordon-Wylie, S. W. *J. Am. Chem. Soc.* **1989**, *111*, 4511–4513.

[94] Miller, C. G.; Gordon-Wylie, S. W.; Horwitz, C. P.; Strazisar, S. A.; Peraino, D. K.; Clark, G. R.; Weintraub, S. T.; Collins, T. J. *J. Am. Chem. Soc.* **1998**, *120*, 11540–11541.

[95] MacDonnell, F. M.; Fackler, N. L. P.; Stern, C.; O'Halloran, T. V. *J. Am. Chem. Soc.* **1994**, *116*, 7431–7432.

[96] Hong, S.; Lee, Y.-M.; Sankaralingam, M.; Vardhaman, A. K.; Park, Y. J.; Cho, K.-B.; Ogura, T.; Sarangi, R.; Fukuzumi, S.; Nam, W. *J. Am. Chem. Soc.* **2016**, *138*, 8523–8532.

[97] Borovik, A. S. *Acc. Chem. Res.* **2005**, *38*, 54–61.

[98] Parsell, T. H.; Behan, R. K.; Green, M. T.; Hendrich, M. P.; Borovik, A. S. *J. Am. Chem. Soc.* **2006**, *128*, 8728–8729.

[99] Taguchi, T.; Gupta, R.; Lassalle-Kaiser, B.; Boyce, D. W.; Yachandra, V. K.; Tolman, W. B.; Yano, J.; Hendrich, M. P.; Borovik, A. S. *J. Am. Chem. Soc.* **2012**, *134*, 1996–1999.

[100] Leto, D. F.; Ingram, R.; Day, V. W.; Jackson, T. A. *Chem. Commun.* **2013**, *49*, 5378–5380.

[101] Wu, X.; Seo, M. S.; Davis, K. M.; Lee, Y.-M.; Chen, J.; Cho, K.-B.; Pushkar, Y. N.; Nam, W. *J. Am. Chem. Soc.* **2011**, *133*, 20088–20091.

[102] Chen, J.; Yoon, H.; Lee, Y.-M.; Seo, M. S.; Sarangi, R.; Fukuzumi, S.; Nam, W. *Chem. Sci.* **2015**, *6*, 3624–3632.

[103] Chen, J.; Lee, Y.-M.; Davis, K. M.; Wu, X.; Seo, M. S.; Cho, K.-B.; Yoon, H.; Park, Y. J.; Fukuzumi, S.; Pushkar, Y. N.; Nam, W. *J. Am. Chem. Soc.* **2013**, *135*, 6388–6391.

[104] Yoon, H.; Lee, Y.-M.; Wu, X.; Cho, K.-B.; Sarangi, R.; Nam, W.; Fukuzumi, S. *J. Am. Chem. Soc.* **2013**, *135*, 9186–9194.

[105] Bryliakov, K. P.; Talsi, E. P. *Coord. Chem. Rev.* **2014**, *276*, 73 – 96.

[106] Winkler, J. R.; Gray, H. B. In *Molecular Electronic Structures of Transition Metal Complexes I*; Mingos, P. D. M., Day, P., Dahl, P. J., Eds.; Springer Berlin Heidelberg: Berlin, Heidelberg, 2012; pp 17–28.

[107] Betley, T. A.; Wu, Q.; Voorhis, T. V.; Nocera, D. G. *Inorg. Chem.* **2008**, *47*, 1849–1861.

[108] Betley, T. A.; Surendranath, Y.; Childress, M. V.; Alliger, G. E.; Fu, R.; Cummins, C. C.; Nocera, D. G. *Phil. Trans. R. Soc. B* **2008**, *363*, 1293–1303.

[109] Ray, K.; Heims, F.; Pfaff, F. F. *Eur. J. Inorg. Chem* **2013**, *2013*, 3784–3807.

[110] Hohenberger, J.; Ray, K.; Meyer, K. *Nat. Commun.* **2012**, *3*, 720.

[111] Scepaniak, J. J.; Fulton, M. D.; Bontchev, R. P.; Duesler, E. N.; Kirk, M. L.; Smith, J. M. *J. Am. Chem. Soc.* **2008**, *130*, 10515–10517.

[112] Mayer, J. M. *Annu. Rev. Phys. Chem.* **2004**, *55*, 363–390.

[113] Warren, J. J.; Tronic, T. A.; Mayer, J. M. *Chem. Rev.* **2010**, *110*, 6961–7001.

[114] Borovik, A. S. *Chem. Soc. Rev.* **2011**, *40*, 1870–1874.

[115] Gunay, A.; Theopold, K. H. *Chem. Rev.* **2010**, *110*, 1060–1081.

[116] Lai, W.; Li, C.; Chen, H.; Shaik, S. *Ang. Chem. Int. Ed.* **2012**, *51*, 5556–5578.

[117] Shaik, S.; Hirao, H.; Kumar, D. *Acc. Chem. Res.* **2007**, *40*, 532–542.

[118] Srnec, M.; Wong, S. D.; England, J.; Que Jr, L.; Solomon, E. I. *Proc. Natl. Acad. Sci. U.S.A.* **2012**, *109*, 14326–14331.

[119] Spaltenstein, E.; Conry, R. R.; Critchlow, S. C.; Mayer, J. M. *J. Am. Chem. Soc.* **1989**, *111*, 8741–8742.

[120] Mayer, J. M.; Thorn, D. L.; Tulip, T. H. *J. Am. Chem. Soc.* **1985**, *107*, 7454–7462.

[121] Hay-Motherwell, R. S.; Wilkinson, G.; Hussain-Bates, B.; Hursthouse, M. B. *Polyhedron* **1993**, *12*, 2009 – 2012.

[122] Schröder, D.; Holthausen, M. C.; Schwarz, H. *J. Phys. Chem. B* **2004**, *108*, 14407–14416.

[123] Poverenov, E.; Efremenko, I.; Frenkel, A. I.; Ben-David, Y.; Shimon, L. J. W.; Leitus, G.; Konstantinovski, L.; Martin, J. M. L.; Milstein, D. *Nature* **2008**, *455*, 1093–1096.

[124] Pfaff, F. F.; Kundu, S.; Risch, M.; Pandian, S.; Heims, F.; Pryjomska-Ray, I.; Haack, P.; Metzinger, R.; Bill, E.; Dau, H.; Comba, P.; Ray, K. *Ang. Chem. Int. Ed.* **2011**, *50*, 1711–1715.

[125] Lacy, D. C.; Park, Y. J.; Ziller, J. W.; Yano, J.; Borovik, A. S. *J. Am. Chem. Soc.* **2012**, *134*, 17526–17535.

[126] Hong, S.; Pfaff, F. F.; Kwon, E.; Wang, Y.; Seo, M.-S.; Bill, E.; Ray, K.; Nam, W. *Ang. Chem. Int. Ed.* **2014**, *53*, 10403–10407.

[127] Donoghue, P. J.; Tehranchi, J.; Cramer, C. J.; Sarangi, R.; Solomon, E. I.; Tolman, W. B. *J. Am. Chem. Soc.* **2011**, *133*, 17602–17605.

[128] Dhar, D.; Tolman, W. B. *J. Am. Chem. Soc.* **2015**, *137*, 1322–1329.

[129] Dhar, D.; Yee, G. M.; Spaeth, A. D.; Boyce, D. W.; Zhang, H.; Dereli, B.; Cramer, C. J.; Tolman, W. B. *J. Am. Chem. Soc.* **2016**, *138*, 356–368.

[130] Tehranchi, J.; Donoghue, P. J.; Cramer, C. J.; Tolman, W. B. *Eur. J. Inorg. Chem* **2013**, *2013*, 4077–4084.

[131] Pirovano, P.; Farquhar, E. R.; Swart, M.; Fitzpatrick, A. J.; Morgan, G. G.; McDonald, A. R. *Chem. Eur. J.* **2015**, *21*, 3785–3790.

[132] Corona, T.; Pfaff, F. F.; Acuña-Parés, F.; Draksharapu, A.; Whiteoak, C. J.; Martin-Diaconescu, V.; Lloret-Fillol, J.; Browne, W. R.; Ray, K.; Company, A. *Chem. Eur. J.* **2015**, *21*, 15029–15038.

[133] Pfaff, F. F.; Heims, F.; Kundu, S.; Mebs, S.; Ray, K. *Chem. Commun.* **2012**, *48*, 3730–3732.

[134] Groothaert, M. H.; Smeets, P. J.; Sels, B. F.; Jacobs, P. A.; Schoonheydt, R. A. *J. Am. Chem. Soc.* **2005**, *127*, 1394–1395.

[135] Smeets, P. J.; Hadt, R. G.; Woertink, J. S.; Vanelderen, P.; Schoonheydt, R. A.; Sels, B. F.; Solomon, E. I. *J. Am. Chem. Soc.* **2010**, *132*, 14736–14738.

[136] Woertink, J. S.; Smeets, P. J.; Groothaert, M. H.; Vance, M. A.; Sels, B. F.; Schoonheydt, R. A.; Solomon, E. I. *Proc. Natl. Acad. Sci. U.S.A.* **2009**, *106*, 18908–18913.

[137] Hu, X.; Meyer, K. *J. Am. Chem. Soc.* **2004**, *126*, 16322–16323.

[138] Jenkins, D. M.; Betley, T. A.; ; Peters, J. C. *J. Am. Chem. Soc.* **2002**, *124*, 11238–11239.

[139] Hu, X.; Meyer, K. *J. Am. Chem. Soc.* **2004**, *126*, 16322–16323.

[140] Dai, X.; Kapoor, P.; Warren, T. H. *J. Am. Chem. Soc.* **2004**, *126*, 4798–4799.

[141] Cowley, R. E.; Bontchev, R. P.; Sorrell, J.; Sarracino, O.; Feng, Y.; Wang, H.; Smith, J. M. *J. Am. Chem. Soc.* **2007**, *129*, 2424–2425.

[142] Shay, D. T.; Yap, G. P. A.; Zakharov, L. N.; Rheingold, A. L.; Theopold, K. H. *Ang. Chem. Int. Ed.* **2005**, *44*, 1508–1510.

[143] Shay, D. T.; Yap, G. P. A.; Zakharov, L. N.; Rheingold, A. L.; Theopold, K. H. *Ang. Chem. Int. Ed.* **2006**, *45*, 7870–7870.

[144] Jones, C.; Schulten, C.; Rose, R. P.; Stasch, A.; Aldridge, S.; Woodul, W. D.; Murray, K. S.; Moubaraki, B.; Brynda, M.; La Macchia, G.; Gagliardi, L. *Ang. Chem. Int. Ed.* **2009**, *48*, 7406–7410.

[145] Zhang, L.; Liu, Y.; Deng, L. *J. Am. Chem. Soc.* **2014**, *136*, 15525–15528.

[146] Zolnhofer, E. M.; Käß, M.; Khusniyarov, M. M.; Heinemann, F. W.; Maron, L.; van Gastel, M.; Bill, E.; Meyer, K. *J. Am. Chem. Soc.* **2014**, *136*, 15072–15078.

[147] Kogut, E.; Wiencko, H. L.; Zhang, L.; Cordeau, D. E.; Warren, T. H. *J. Am. Chem. Soc.* **2005**, *127*, 11248–11249.

[148] Waterman, R.; Hillhouse, G. L. *J. Am. Chem. Soc.* **2008**, *130*, 12628–12629.

[149] Mindiola, D. J.; Hillhouse, G. L. *J. Am. Chem. Soc.* **2001**, *123*, 4623–4624.

[150] Laskowski, C. A.; Miller, A. J. M.; Hillhouse, G. L.; Cundari, T. R. *J. Am. Chem. Soc.* **2011**, *133*, 771–773.

[151] Thangavel, A.; Wieliczko, M.; Bacsa, J.; Scarborough, C. C. *Inorg. Chem.* **2013**, *52*, 13282–13287.

[152] Lam, B. M. T.; Halfen, J. A.; Young Jr, V. G.; Hagadorn, J. R.; Holland, P. L.; Lledós, A.; Cucurull-Sánchez, L.; Novoa, J. J.; Alvarez, S.; Tolman, W. B. *Inorg. Chem.* **2000**, *39*, 4059–4072.

[153] Halfen, J. A.; Mahapatra, S.; Wilkinson, E. C.; Kaderli, S.; Young, V. G.; Que Jr, L.; Zuberbühler, A. D.; Tolman, W. B. *Science* **1996**, *271*, 1397–1400.

[154] Karahalis, G. J.; Thangavel, A.; Chica, B.; Bacsa, J.; Dyer, R. B.; Scarborough, C. C. *Inorg. Chem.* **2016**, *55*, 1102–1107.

[155] Kimura, E.; Shiota, T.; Koike, T.; Shiro, M.; Kodama, M. *J. Am. Chem. Soc.* **1990**, *112*, 5805–5811.

[156] Boeyens, J. C. A.; Fox, C. C.; Hancock, R. D. *Inorg. Chim. Acta.* **1984**, *87*, 1–4.

[157] Kunishita, A.; Ertem, M. Z.; Okubo, Y.; Tano, T.; Sugimoto, H.; Ohkubo, K.; Fujieda, N.; Fukuzumi, S.; Cramer, C. J.; Itoh, S. *Inorg. Chem.* **2012**, *51*, 9465–9480.

[158] Abe, T.; Morimoto, Y.; Tano, T.; Mieda, K.; Sugimoto, H.; Fujieda, N.; Ogura, T.; Itoh, S. *Inorg. Chem.* **2014**, *53*, 8786–8794.

[159] Kunishita, A.; Kubo, M.; Sugimoto, H.; Ogura, T.; Sato, K.; Takui, T.; Itoh, S. *J. Am. Chem. Soc.* **2009**, *131*, 2788–2789.

[160] Tano, T.; Okubo, Y.; Kunishita, A.; Kubo, M.; Sugimoto, H.; Fujieda, N.; Ogura, T.; Itoh, S. *Inorg. Chem.* **2013**, *52*, 10431–10437.

[161] Musker, W. K. *Coord. Chem. Rev.* **1992**, *117*, 133–157.

[162] Musker, W. K.; Hussain, H. S. *Inorg. Chem.* **1966**, *5*, 1416–1419.

[163] Musker, W. K.; Steffen, E. D. *Inorg. Chem.* **1974**, *13*, 1951–1955.

[164] Nielson, D. O.; Larsen, M. L.; Willett, R. D.; Legg, J. I. *J. Am. Chem. Soc.* **1971**, *93*, 5079–5082.

[165] Averill, D. F.; Legg, J. I.; Smith, D. L. *Inorg. Chem.* **1972**, *11*, 2344–2349.

[166] Legg, J. I.; Nielson, D. O.; Smith, D. L.; Larson, M. L. *J. Am. Chem. Soc.* **1968**, *90*, 5030–5031.

[167] Farmer, P. J.; Solouki, T.; Mills, D. K.; Soma, T.; Russell, D. H.; Reibenspies, J. H.; Darensbourg, M. Y. *J. Am. Chem. Soc.* **1992**, *114*, 4601–4605.

[168] Mills, D. K.; Reibenspies, J. H.; Darensbourg, M. Y. *Inorg. Chem.* **1990**, *29*, 4364–4366.

[169] Buonomo, R. M.; Font, I.; Maguire, M. J.; Reibenspies, J. H.; Tuntulani, T.; Darensbourg, M. Y. *J. Am. Chem. Soc.* **1995**, *117*, 963–973.

[170] Halfen, J. A.; Uhan, J. M.; Fox, D. C.; Mehn, M. P.; Que Jr, L. *Inorg. Chem.* **2000**, *39*, 4913–4920.

[171] Geiger, R. A.; Chattopadhyay, S.; Day, V. W.; Jackson, T. A. *Dalton Trans.* **2011**, *40*, 1707–1715.

[172] Halfen, J. A.; Moore, H. L.; Fox, D. C. *Inorg. Chem.* **2002**, *41*, 3935–3943.

[173] Halfen, J. A.; Fox, D. C.; Mehn, M. P.; Que Jr, L. *Inorg. Chem.* **2001**, *40*, 5060–5061.

[174] Kasowski, W. J.; Jr., J. C. B. *J. Am. Chem. Soc.* **1969**, *91*, 3212–3218.

[175] Zadrozny, J. M.; Liu, J.; Piro, N. A.; Chang, C. J.; Hill, S.; Long, J. R. *Chem. Commun.* **2012**, *48*, 3927–3929.

[176] Wittmann, H.; Schorm, A.; Sundermeyer, J. *Z. Anorg. Allg. Chem.* **2000**, *626*, 1583–1590.

[177] Nam, W. *Acc. Chem. Res.* **2007**, *40*, 522–531.

[178] Ray, K.; Pfaff, F. F.; Wang, B.; Nam, W. *J. Am. Chem. Soc.* **2014**, *136*, 13942–13958.

[179] Que, L. *Acc. Chem. Res.* **2007**, *40*, 493–500.

[180] Suh, Y.; Seo, M. S.; Kim, K. M.; Kim, Y. S.; Jang, H. G.; Tosha, T.; Kitagawa, T.; Kim, J.; Nam, W. *J. Inorg. Biochem.* **2006**, *100*, 627–633.

[181] de Visser, S. P.; Rohde, J.-U.; Lee, Y.-M.; Cho, J.; Nam, W. *Coord. Chem. Rev.* **2013**, *257*, 381–393.

[182] Cho, J.; Sarangi, R.; Annaraj, J.; Kim, S. Y.; Kubo, M.; Ogura, T.; Solomon, E. I.; Nam, W. *Nat. Chem.* **2009**, *1*, 568–572.

[183] Cho, J.; Sarangi, R.; Kang, H. Y.; Lee, J. Y.; Kubo, M.; Ogura, T.; Solomon, E. I.; Nam, W. *J. Am. Chem. Soc.* **2010**, *132*, 16977–16986.

[184] Cho, J.; Kang, H. Y.; Liu, L. V.; Sarangi, R.; Solomon, E. I.; Nam, W. *Chem. Sci.* **2013**, *4*, 1502–1508.

[185] Jo, Y.; Annaraj, J.; Seo, M. S.; Lee, Y.-M.; Kim, S. Y.; Cho, J.; Nam, W. *J. Inorg. Biochem.* **2008**, *102*, 2155–2159.

[186] Kieber-Emmons, M. T.; Annaraj, J.; Seo, M. S.; Van Heuvelen, K. M.; Tosha, T.; Kitagawa, T.; Brunold, T. C.; Nam, W.; Riordan, C. G. *J. Am. Chem. Soc.* **2006**, *128*, 14230–14231.

[187] Barefield, E. K.; Wagner, F. *Inorg. Chem.* **1973**, *12*, 2435–2439.

[188] Hossain, M. D.; Jia, Z.; Monteiro, M. J. *Macromolecules* **2014**, *47*, 4955–4970.

[189] Gash, V. W. *J. Org. Chem.* **1972**, *37*, 2197–2201.

[190] Kanoh, S.; Nishimura, T.; Tsuchida, T.; Senda, H.; Motoi, M.; Takani, M.; Matsuura, N. *Macromol. Chem. Phys.* **2001**, *202*, 2489–2503.

[191] Liu, S. T.; Liu, C. Y. *J. Org. Chem.* **1992**, *57*, 6079–6080.

[192] Richman, J. E.; Atkins, T. J. *J. Am. Chem. Soc.* **1974**, *96*, 2268–2270.

[193] Chandrasekaran, V.; Lindhorst, T. K. *Chem. Commun.* **2012**, *48*, 7519–7521.

[194] Petrovski, Ž.; Romão, C. C.; Afonso, C. A. M. *Synth Commun.* **2008**, *38*, 2761–2767.

[195] von E. Doering, W.; Levy, L. K. *J. Am. Chem. Soc.* **1955**, *77*, 509–513.

[196] Dostrovsky, I.; Hughes, E. D. *J. Chem. Soc. (Res.)* **1946**, 157–161.

[197] Du, M.; Bu, X.-H.; Wang, G.-C.; Guo, Y.-M.; Zhang, R.-H. *Inorg. Chim. Acta.* **2001**, *320*, 190–197.

[198] Kroll, N.; Theilacker, K.; Schoknecht, M.; Baabe, D.; Wiedemann, D.; Kaupp, M.; Grohmann, A.; Horner, G. *Dalton Trans.* **2015**, *44*, 19232–19247.

[199] Bencini, A.; Bianchi, A.; Garcia-España, E.; Micheloni, M.; Ramirez, J. A. *Coord. Chem. Rev.* **1999**, *188*, 97–156.

[200] Du, M.; Bu, X.-H.; Xu, Q.; Shang, Z.-L.; Zhang, R.-H. *J. Chem. Crystallogr.* **2000**, *30*, 531–534.

[201] Ozeryanskii, V. A.; Pozharskii, A. F.; Antonov, A. S.; Filarowski, A. *Org. Biomol. Chem.* **2014**, *12*, 2360–2369.

[202] Dalrymple, S. A.; Shimizu, G. K. H. *J. Mol. Struct.* **2006**, *796*, 95–106.

[203] Belle, C.; Bougault, C.; Averbuch, M.-T.; Durif, A.; Pierre, J.-L.; Latour, J.-M.; Le Pape, L. *J. Am. Chem. Soc.* **2001**, *123*, 8053–8066.

[204] Addison, A. W.; Rao, T. N.; Reedijk, J.; van Rijn, J.; Verschoor, G. C. *J. Chem. Soc., Dalton Trans.* **1984**, 1349–1356.

[205] Kawamura, M.; Sunada, Y.; Kai, H.; Koike, N.; Hamada, A.; Hayakawa, H.; Jin, R.-H.; Nagashima, H. *Adv. Synth. Cat.* **2009**, *351*, 2086–2090.

[206] Pawlak, P. L.; Panda, M.; Loloee, R.; Kucera, B. E.; Costes, J.-P.; Tuchagues, J.-P.; Chavez, F. A. *Dalton Trans.* **2011**, *40*, 2926–2931.

[207] O'Reilly, R. K.; Gibson, V. C.; White, A. J. P.; Williams, D. J. *Polyhedron* **2004**, *23*, 2921–2928.

[208] Ballester, L.; Coronado, E.; Gutierrez, A.; Monge, A.; Perpinan, M. F.; Pinilla, E.; Rico, T. *Inorg. Chem.* **1992**, *31*, 2053–2056.

[209] Clemente-Juan, J. M.; Chansou, B.; Donnadieu, B.; Tuchagues, J.-P. *Inorg. Chem.* **2000**, *39*, 5515–5519.

[210] Wikstrom, J. P.; Nazarenko, A. Y.; Reiff, W. M.; Rybak-Akimova, E. V. *Inorg. Chim. Acta.* **2007**, *360*, 3733–3740.

[211] Aurivillius, B. *Acta Chem. Scand.* **1977**, *31*.

[212] Ford, P. C.; Cariati, E.; Bourassa, J. *Chem. Rev.* **1999**, *99*, 3625–3648.

[213] Spencer, D. J. E.; Reynolds, A. M.; Holland, P. L.; Jazdzewski, B. A.; Duboc-Toia, C.; Le Pape, L.; Yokota, S.; Tachi, Y.; Itoh, S.; Tolman, W. B. *Inorg. Chem.* **2002**, *41*, 6307–6321.

[214] Mills, J. E.; Maryanoff, C. A.; McComsey, D. F.; Stanzione, R. C.; Scott, L. *J. Org. Chem.* **1987**, *52*, 1857–1859.

[215] Lee, J.-J.; Stanger, K. J.; Noll, B. C.; Gonzalez, C.; Marquez, M.; Smith, B. D. *J. Am. Chem. Soc.* **2005**, *127*, 4184–4185.

[216] Batten, S. R.; Spiccia, L.; Templar, C. E. *Acta Crystallogr. Sect. E* **2001**, *57*, m265–m266.

[217] Riedel, P. J.; Arulsamy, N.; Mehn, M. P. *Inorg. Chem. Commun.* **2011**, *14*, 734–737.

[218] Serpell, C. J.; Chall, R.; Thompson, A. L.; Beer, P. D. *Dalton Trans.* **2011**, *40*, 12052–12055.

[219] Bell, T. W.; Choi, H.-J.; Harte, W.; Drew, M. G. B. *J. Am. Chem. Soc.* **2003**, *125*, 12196–12210.

[220] Karplus, M. *J. Am. Chem. Soc.* **1963**, *85*, 2870–2871.

[221] Everett, M.; Jolleys, A.; Levason, W.; Pugh, D.; Reid, G. *Chem. Commun.* **2014**, *50*, 5843–5846.

[222] Springborg, J.; Pretzmann, U.; Olsen, C. E. *Acta Chem. Scand.* **1996**, *50*, 294.

[223] Springborg, J. *Dalton Trans.* **2003**, 1653–1665.

[224] Alder, R. W.; Bowman, P. S.; Steele, W. R. S.; Winterman, D. R. *Chem. Commun.* **1968**, 723–724.

[225] Ishikawa, T. *Superbases for Organic Synthesis: Guanidines, Amidines, Phosphazenes and Related Organocatalysts*; Wiley, 2009.

[226] Broge, L.; Sotofte, I.; Jensen, K.; Jensen, N.; Pretzmann, U.; Springborg, J. *Dalton Trans.* **2007**, 3826–3839.

[227] Kanbara, T.; Suzuki, Y.; Yamamoto, T. *Eur. J. Org. Chem* **2006**, *2006*, 3314–3316.

[228] Appel, R.; Fuchs, J.; Tyrrell, S. M.; Korevaar, P. A.; Stuart, M. C. A.; Voets, I. K.; Schönhoff, M.; Besenius, P. *Chem. Eur. J.* **2015**, *21*, 19257–19264.